

ANALYSIS OF COMPRESSIVE ICE FAILURE DURING
ICE-STRUCTURE INTERACTION

THOMAS M. BROWNE



Analysis of Compressive Ice Failure during Ice-structure Interaction

by

© Thomas M. Browne, B.Eng.

A thesis submitted to the School of Graduate Studies
in partial fulfillment of the requirements for the degree of

Master of Engineering

Faculty of Engineering and Applied Science

Memorial University of Newfoundland

April 2012

St. John's

Newfoundland

Abstract

Forty-four small-scale ice indentation tests have been performed on confined polycrystalline ice specimens in order to aid in the understanding of the mechanics associated with ice failure processes related to high pressure zones formed during ice-structure interaction. A review of fundamental ice mechanics theory, execution of a laboratory-scale experimental program, and analysis of the collected data were completed.

Through analysis of the collected data, cyclic loading patterns, at frequencies as high as 250 Hz, have been linked to crushing and extrusion of ice associated with high pressure zone failures. Structural compliance was observed to aid in the development of cyclic loading patterns and the frequency has been determined to have a linear dependence on structural stiffness. A linear relationship was also observed between the indentation speed and the resulting cyclic loading frequency. A layer of damaged ice adjacent to the indenter was observed and composed of regions of both dense microfracture and recrystallized ice.

This study is part of a larger, three year research project on ice compressive failure mechanics that is jointly funded by Statoil and the Research and Development Corporation of Newfoundland and Labrador. Promising results from the work presented in this thesis will be used to guide the remainder of the research project.

Acknowledgements

I would first like to thank my supervisors, Dr. Ian Jordaan and Dr. Rocky Taylor, for their support and guidance throughout my graduate studies. Their expert advice in the areas of ice mechanics, experimentation, data analysis, and writing has been invaluable to me and I am truly grateful. I would also like to thank Dr. Charles Randell and C-CORE for providing me with both financial support and an excellent environment to pursue research. Mr. Andrew Macneill, of C-CORE, is due many thanks and praise for dedicating his time and skill to the design of the testing apparatus and the selection of instrumentation. Sincere gratitude is extended to Mr. Steve Keats and Mr. Austin Bugden of NRC-IOT for their assistance and guidance in the preparation and execution of the laboratory work throughout this program.

Many thanks are given to Statoil and the Research and Development Corporation of Newfoundland and Labrador for funding the research presented in this thesis. Financial support from the School of Graduate Studies at Memorial University, C-CORE, MITACS, the Research and Development Corporation of Newfoundland and Labrador, the W. Garfield Weston Foundation, and the Royal Bank of Canada is gratefully acknowledged. Much appreciation is also given to Dr. Brian Veitch, Dr. Leonard Lye, and Dr. Wei Qiu for providing their many letters of reference over the course of my program.

I would like to dedicate this work to my mother, Lena, and my father, Steve. My father passed away while I was completing my undergraduate studies at Memorial. The work ethic that you instilled in me from an early age is the underlying factor in all that I accomplish.

Finally, a special thank you to Ms. Emilie Martin for her support and encouragement in all that I do.

Table of Contents

Chapter 1: Introduction	1
1.1 Overview	1
1.2 Objectives	2
1.3 Scope of Research.....	3
1.4 Outline of Thesis.....	3
Chapter 2: Literature Review	5
2.1 Overview	5
2.2 The Mechanical Behaviour of Ice.....	5
2.2.1 Ice as a Viscoelastic Material	5
2.2.2 Fracture, Damage, and High Pressure Zones.....	13
2.3 Ice-structure Interaction.....	30
2.4 Previous Indentation Test Programs	35
Chapter 3: Experimental Methodology	43
3.1 Overview	43
3.1.1 Physical Problem	43
3.1.2 Rationale for Small-scale Laboratory Testing	47
3.2 Experimental Design.....	52
3.2.1 Overview of Test Set-up	53

3.2.2	Test Structure for Phase 1A	56
3.2.3	Test Structure for Phase 1B	66
3.3	Ice Specimen Preparation	70
3.4	Testing Procedure	72
3.5	Thin-sectioning Procedure	74
3.6	Summary	77
Chapter 4: Experimental Results		79
4.1	Overview	79
4.2	Results from Phase 1A	80
4.2.1	Test Matrix – Phase 1A	81
4.2.2	Slow Speed Test (4 mm/s)	83
4.2.3	Medium Speed Test (7 mm/s)	86
4.2.4	Fast Speed Test (10 mm/s)	88
4.2.5	Warm Ice Results (-5°C)	91
4.3	Results from Phase 1B	95
4.3.1	Test Matrix – Phase 1B	96
4.3.2	Slow Speed Test (2 mm/s)	97
4.3.3	Medium Speed Test (4 mm/s)	100
4.3.4	Fast Speed Test (6 mm/s)	103
4.3.5	Results for Increased Indenter Size	106
4.4	Summary	109
Chapter 5: Analysis		110
5.1	Overview	110
5.2	Observations of Ice Failure Process	111
5.2.1	Crushing	111
5.2.2	Spalling	114
5.3	Effect of Temperature	116
5.4	Effect of Structural Compliance	118

5.4.1	Relative Indentation Rate.....	119
5.4.2	Amplitude and Frequency of Cyclic Loading.....	121
5.5	Link between Speed and Frequency	123
5.6	Preliminary Spectral Analysis.....	125
5.7	Summary	127
Chapter 6: Discussions and Conclusions		129
6.1	Main Conclusions	129
6.1.1	Crushing and Cyclic Loading	129
6.1.2	Effect of Temperature	130
6.1.3	Effect of Structural Compliance	131
6.1.4	Linear Relationship between Speed and Frequency	131
6.2	Recommendations for Future Work.....	132
Bibliography		134
APPENDIX A – Test Results: Total Load, Structural Deflection, and Thin-section Photographs		140
	Phase 1A	141
	Phase 1B	170
APPENDIX B – System Characterization Test Results.....		184
APPENDIX C – Calibrations		190
	Tekscan I-Scan Pressure Sensors.....	191
	Miniature Load Cell.....	193
	LVDTs	194

List of Figures

Figure 2.1: Typical creep curve for ice under constant stress.....	6
Figure 2.2: Burgers body - idealized viscoelastic model for ice.....	7
Figure 2.3: Wing crack formation at two grain boundaries in ice under compression (modified from Taylor, 2010).....	17
Figure 2.4: Schematic of ice failure for slow loading rate during medium-scale field tests (Jordaan and Xiao, 1992).	18
Figure 2.5: Photograph of ductile failure resulting from a 0.3 mm/s loading rate during medium-scale field tests (photo courtesy of Dan Masterson).	19
Figure 2.6: Ice failure mode for fast loading rate during medium-scale field tests (modified from Jordaan and Xiao, 1992).....	20
Figure 2.7: Photograph of damage resulting from a 10 mm/s loading rate during medium-scale field tests (photo courtesy of Dan Masterson).....	20
Figure 2.8: Schematic identifying the presence of high pressure zones at an ice-structure interface (Jordaan, 2001).	21
Figure 2.9: Typical spalling event for an ice sheet (modified from Sanderson, 1988).	22
Figure 2.10: Idealization of high pressure zone distribution for common contact geometries (Jordaan, 2001).	22
Figure 2.11: Comparison between von Mises and confining pressure in the layer at peak load for: (a) an element at the edge, (b) an element at the middle of the edge and center, and (c) an element at the center.	23

Figure 2.12: Relationship between relative creep compliance of ice and confining pressure (modified from Jordaan et al., 2005).	25
Figure 2.13: Damaged layer at (Left) medium scale and (Right) small scale.	26
Figure 2.14: Damage rate versus hydrostatic pressure (Jordaan et al., 1994).	29
Figure 2.15: Typical structural responses, in the form of displacement, during interaction with drifting ice floes at various speeds (Kärnä, 1994).	31
Figure 2.16: Instrumented loading zones (Top) and acceleration record (Bottom) showing transition from a non-simultaneous to quasi-static loading pattern recorded during a May 12, 1986 loading event on the Molikpaq (modified from Jefferies et al., 2008).	34
Figure 2.17: Steady-state structural response of a channel marker in the Baltic Sea (Kärnä, 1994).	35
Figure 2.18: Three frequency domains observed during indentation of a confined ice specimen (courtesy of Paul Barrette).	37
Figure 2.19: Load record identifying five different failure modes associated with compressive ice failure (Wells et al., 2010).	41
Figure 3.1: Schematic of pressure distribution before ($t = t_0$) and after ($t = t_1$) localized failure for (a) crushing, and (b) spalling. (Taylor et al., 2008).	45
Figure 3.2: Cyclic processes in the vicinity of a single high pressure zone during crushing failure of ice (Jordaan et al., 2008).	47
Figure 3.3: Pressure distribution of a simulated high pressure zone produced with a 20-mm diameter steel indenter (Wells et al., 2010).	48
Figure 3.4: A photograph of the indentation system and an ice specimen used by Paul Barrette at Memorial University.	50
Figure 3.5: Changes in pressure distribution in a high pressure zone are linked to cyclic loading during a small-scale indentation test (Wells et al., 2010).	51
Figure 3.6: Steel confining rings, 150 mm (Left) and 300 mm (Right) in diameter, used to suppress splitting of ice specimens.	55
Figure 3.7: Photograph of indentation system and confined specimen mounted to the MTS.	56
Figure 3.8: General arrangement of the testing system used in Phase 1A.	57

Figure 3.9: Photographs of the pinned end connections. The rotating end connection is shown on the right.	58
Figure 3.10: Compliant beam combinations used for Phase 1A.....	59
Figure 3.11: Photograph of Compliant System 4 identifying position of aluminum blocks. Two blocks are located in the front and two in the back.....	60
Figure 3.12: Photograph showing the location of the LVDT array.	63
Figure 3.13: Photographs of location of miniature and MTS load cells.....	64
Figure 3.14: Photograph showing the positioning of a Tekscan tactile pressure sensor.	65
Figure 3.15: Photograph of 20 mm rigid indentation system.	67
Figure 3.16: 40 mm indenter design drawing (Left); Photograph of 40 mm rigid indentation system (Right).....	67
Figure 3.17: Photographs of Small Cold Room equipment: (a) bubble-free sculptor's ice, (b) bandsaw, (c) industrial ice crusher, and (d) sieve.....	71
Figure 3.18: Photograph of an indented area being extracted using the milling machine in the Large Cold Room.	75
Figure 3.19: Photograph of the microtome located in the Small Cold Room.....	76
Figure 4.1: Test naming convention example.....	80
Figure 4.2: Miniature load cell and LVDT data for test T16_1A_04_15_C3 showing total force on the indenter (Top) and structural deflection (Bottom).	84
Figure 4.3: Pressure distribution images corresponding to the load drops identified in force-time trace in Figure 4.2.	84
Figure 4.4: Thin-section of damaged zone from test T16_1A_04_15_C3 photographed with side lighting (Top) and through cross-polarized light (Bottom).	85
Figure 4.5: Miniature load cell and LVDT data for test T17_1A_07_15_C3 showing total force on the indenter (Top) and structural deflection (Bottom).	87
Figure 4.6: Pressure distribution images corresponding to the load drops identified in the force-time trace in Figure 4.5.....	87

Figure 4.7: Thin-section of damaged zone from test T17_1A_07_15_C3 photographed with side lighting (Top) and through cross-polarized light (Bottom).	88
Figure 4.8: Miniature load cell and LVDT data for test T18_1A_10_15_C3 showing total force on the indenter (Top) and structural deflection (Bottom).	90
Figure 4.9: Pressure distribution images corresponding to the load drops identified in the force-time trace in Figure 4.8.....	90
Figure 4.10: Thin-section of damaged zone from test T18_1A_10_15_C3 photographed with side lighting (Top) and through cross-polarized light (Bottom).	91
Figure 4.11: Miniature load cell and LVDT data for test T04_1A_04_05_C3 showing total force on the indenter (Top) and structural deflection (Bottom).	92
Figure 4.12: Miniature load cell and LVDT data for test T05_1A_07_05_C3 showing total force on the indenter (Top) and structural deflection (Bottom).	93
Figure 4.13: Miniature load cell and LVDT data for test T06_1A_10_05_C3 showing total force on the indenter (Top) and structural deflection (Bottom).	93
Figure 4.14: Thin-section of damaged zone from test T04_1A_04_05_C3 photographed with side lighting (Top) and through cross-polarized light (Bottom).	94
Figure 4.15: Thin-section of damaged zone from test T05_1A_07_05_C3 photographed with side lighting (Top) and through cross-polarized light (Bottom).	95
Figure 4.16: MTS load cell data for test T48_1B_02_10_R20 showing total force on the indenter.....	98
Figure 4.17: Enlarged view of the region boxed in red in Figure 4.16.....	98
Figure 4.18: Pressure distribution images corresponding to the load drop identified in the force-time trace in Figure 4.17.	99
Figure 4.19: Thin-section of damaged zone from test T48_1B_02_10_R20 photographed with side lighting (Top) and through cross-polarized light (Bottom).	99
Figure 4.20: MTS load cell data for test T51_1B_04_10_R20 showing total force on the indenter.....	101

Figure 4.21: Enlarged view of the region boxed in red in Figure 4.20.....	101
Figure 4.22: Pressure distribution images corresponding to the load drop identified in the force-time trace in Figure 4.21.	102
Figure 4.23: Thin-section of damaged zone from test T51_1B_04_10_R20 photographed with side lighting (Top) and through cross-polarized light (Bottom).	102
Figure 4.24: MTS load cell data for test T52_1B_06_10_R20 showing total force on the indenter.....	104
Figure 4.25: Enlarged view of the region boxed in red in Figure 4.20.....	105
Figure 4.26: Pressure distribution images corresponding to the load drop identified in the force-time trace in Figure 4.21.	105
Figure 4.27: Thin-section of damaged zone from test T52_1B_06_10_R20 photographed with side lighting (Top) and through cross-polarized light (Bottom).	105
Figure 4.28: MTS load cell data for test T54_1B_02_10_R40 showing total force on the indenter.....	107
Figure 4.29: Enlarged view of the region boxed in red in Figure 4.28.....	107
Figure 4.30: Pressure distribution images corresponding to the load drop identified in the force-time trace in Figure 4.29.	108
Figure 4.31: Thin-section of damaged zone from test T54_1B_04_10_R40 photographed with side lighting (Top) and through cross-polarized light (Bottom).	108
Figure 5.1: Miniature load cell data identifying cyclic crushing failure.....	113
Figure 5.2: Pressure distribution images before and after crushing events.	113
Figure 5.3: Miniature load cell data identifying a spalling event.	115
Figure 5.4: Pressure distribution before (a) and after (b) a spalling event, and a still taken from the high-speed video recording of the event.....	115
Figure 5.5: Miniature load cell data for two identical tests at different temperatures.	116

Figure 5.6: Thin-section photographs highlighting the effect of temperature on microstructural modification in the damaged layer.	118
Figure 5.7: Plot of the relative indentation rate for test T23_1A_07_15_C1.	120
Figure 5.8: Relative indentation rates versus nominal indentation rates for Phase 1A indentation systems.	121
Figure 5.9: Plot of frequency versus stiffness for Phase 1A data.	123
Figure 5.10: Plot of frequency versus indentation rate for Phase 1A data.	124
Figure 5.11: Plot of frequency versus indentation rate for Phase 1B data.	125
Figure 5.12: FFT spectral plot for test T14_1A_07_15_C3.	126

List of Tables

Table 3.1: Theoretical properties for Phase 1A indentation systems.....	59
Table 3.2: Measured properties for Phase 1A indentation systems.....	61
Table 4.1: Test Matrix for Phase 1A.....	82
Table 4.2: Test matrix for Phase 1B.....	96
Table 5.1: Relative indentation rates due to structural compliance.....	121
Table 5.2: Average amplitude for periods of cyclic loading for five different indentation systems.....	122

List of Abbreviations and Symbols

ϵ^e	elastic strain
ϵ^d	delayed-elastic creep strain
ϵ^c	viscous creep strain
ϵ	total strain
σ	axial stress
E_m	Young's modulus of ice (or of the Maxwell unit in Burgers body)
μ_k	viscosity coefficient for a Kelvin unit
μ_m	viscosity coefficient for a Maxwell unit
$\dot{\epsilon}_o^d$	creep reference rate
σ_o	constant unit stress (1 MPa)
σ^d	stress in a Kelvin unit dashpot
$\dot{\epsilon}_o^c$	creep parameter
E_k	Young's modulus of a Kelvin unit

$\psi(t)$	reduced time
a_d	function of stress in the case of delayed-elastic strain
K	viscosity parameter
$\mu_{t=0}$	viscosity at time $t = 0$
\mathcal{E}_{ij}	total strain tensor
\mathcal{E}_{ij}^e	elastic strain tensor
\mathcal{E}_{ij}^d	delayed-elastic strain tensor
\mathcal{E}_{ij}^c	viscous creep strain tensor
e_{ij}	deviatoric component of strain tensor
\mathcal{E}_v	volumetric component of strain tensor
e_{ij}^d	delayed-elastic deviatoric strain tensor
\mathcal{E}_v^d	delayed-elastic volumetric strain tensor
e_{ij}^c	viscous creep deviatoric strain tensor
\mathcal{E}_v^c	viscous creep volumetric strain tensor
δ_{ij}^S	Kronecker delta function
ν	Poisson ratio for ice
s	von Mises stress tensor
s^d	effective stress in the Kelvin unit dashpot
f_3	constant in the equation for volumetric strain rate of ice
p	hydrostatic pressure

e	effective total strain under multi-axial load conditions
e^e	effective elastic strain
A_o	cross-sectional area of undamaged ice specimen
P	uniaxial load
A	cross-sectional area of damaged ice specimen
σ_{eff}	effective stress
D	damage variable
S	damage state variable
f_1	function of stress reflecting material properties
$f_1(p)$	low hydrostatic confining pressure dependent variable
$f_2(p)$	high hydrostatic confining pressure dependent variable
β	creep enhancement factor constant
hpz	high pressure zone
NRC-IOT	National Research Council – Institute for Ocean Technology
JOIA	Japan Ocean Industries Association
MTS	Material Testing System
LVDT	Linear Variable Differential Transformer
LCR	Large Cold Room
SCR	Small Cold Room
C.S.	Compliant System
FFT	Fast Fourier Transform

Chapter 1: Introduction

1.1 Overview

Sea ice and icebergs present significant engineering challenges to the development of oil fields off Canada's East Coast, as well as in other ice-prone regions around the world. In areas where ice is much more prevalent, such as the Arctic, marine structures must be designed to withstand regular interactions with ice features. Effective design for ice is critical in ensuring the safety of structures in these maritime regions. It is the design of these offshore structures for petroleum exploration and production that has driven much of the ice mechanics research over the last three decades.

Structures in ice-environments such as those found in the Beaufort Sea, the Baltic Sea, Chukchi Sea, and the Bohai Sea, can include drilling and production platforms, lighthouses, route markers, and ice-breaking ships. These structures experience regular interactions with ice features such as first-year and multi-year sea ice floes, ice ridges, and icebergs. During ice-structure interaction sea ice may

fail in a number of ways including compressive ice failure, flexural failure, shearing failure, buckling, rafting or ridging, or any combination of these.

Compressive ice failure is very important for vertical walled structures interacting with drifting ice floes and the loads associated with crushing failure are a dominant consideration in design. During compressive ice failure, and crushing in particular, structural systems can experience significant vibrations. Three primary modes of vibration associated with full-scale crushing have been observed in the field and are related to the rate of advance of the ice floe: quasi-static loading, steady-state vibration, and nonsimultaneous crushing. The consequences of such dynamic loading are possible structural vibration, resonance, load amplification, and serviceability aspects such as human comfort and use of computers.

1.2 Objectives

The objective of this research program is to improve our understanding of compressive ice failure mechanics during ice-structure interaction and the associated structural feedback. It is specifically aimed at investigating:

- The processes responsible for high pressure zone formation and evolution.
- The processes that serve to limit ice pressures during compressive ice failure.
- The role of structural feedback in ice crushing failure.
- The influence of temperature on load-limiting ice failure mechanisms.
- The effect of indentation rate on the ice-structure interaction process.

The results from this program will build on more than twenty-five years of ice mechanics research carried out by Dr. Ian Jordaan.

1.3 Scope of Research

The research presented in this work involves the investigation of compressive ice failure during interaction with compliant structures through small-scale laboratory testing. The experimental program consisted of two separate test series, referred to as Phase 1A and Phase 1B, both of which were carried out in the cold room facilities at the National Research Council – Institute for Ocean Technology (NRC-IOT). Tests involved the indentation of confined specimens of freshwater polycrystalline ice using spherical steel indenters in order to study the effects of structural compliance, indentation rate, and temperature on the compressive failure of ice. In Phase 1A, the influence of structural feedback on the compressive ice failure process for a single high pressure zone was studied, while in Phase 1B compressive ice failure for a single high pressure zone in the absence of structural feedback was studied.

1.4 Outline of Thesis

This thesis is organized into six chapters. In Chapter 1, an introduction to the research program is provided. Chapter 2 presents a review of literature covering the mechanical behaviour of ice, ice-induced vibration of structures observed in the field, and previous small-scale ice indentation experiments. In Chapter 3 a

detailed description of the experimental program is provided including the rationale for small-scale experimentation, the design of the indentation equipment, and the procedures for ice production, testing, and thin-sectioning. A sample of the experimental results is provided in Chapter 4, with an exhaustive collection of results included in the appendices. In Chapter 5, an analysis of the results is presented, including observations of the ice failure process and the associated effects of temperature, structural compliance, and indentation rate. The final chapter, Chapter 6, discusses the main findings and conclusions and states recommendations for future work.

Chapter 2: Literature Review

2.1 Overview

In order to investigate ice-induced vibrations at the laboratory scale, it is necessary to have a sound understanding of full-scale ice-structure interaction, ice compressive failure mechanics, and the physical processes involved. In this chapter the interaction of ice with structures, the mechanical behaviour of ice, and the results of previous small-scale ice indentation tests will be reviewed.

2.2 The Mechanical Behaviour of Ice

2.2.1 Ice as a Viscoelastic Material

Ice behaves as a brittle, non-linear, viscoelastic solid. When ice is loaded the relationship between stress and strain has a time dependent nature. Ice will experience stress relaxation when held under constant strain, and time-dependent strain when held under constant stress.

Uniaxial Loading

When ice is loaded uniaxially, its deformation can be broken down into three components of strain: elastic, delayed-elastic creep, and non-linear viscous creep. First it experiences instantaneous elastic strain (ϵ^e), followed by delayed-elastic creep strain (ϵ^d), and non-linear viscous creep strain (ϵ^c). The delayed-elastic creep strain is referred to as primary creep and is almost fully recoverable, while the viscous creep strain, often referred to as secondary creep, is non-recoverable. Following secondary creep is a more complex deformation stage referred to as tertiary creep. Tertiary creep is often associated with microcracks forming and joining at grain boundaries leading to accelerated strain rates and, ultimately, complete failure (Duval et al., 1983). Figure 2.1 presents a typical creep curve for ice.

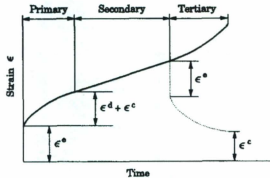


Figure 2.1: Typical creep curve for ice under constant stress.

A spring-and-dashpot model known as Burgers body is commonly used as an idealized viscoelastic model for ice. Burgers body consists of a Maxwell unit (a

spring and dashpot in series) in series with a Kelvin unit (a spring and dashpot in parallel). For the viscoelastic modeling of ice the dashpots of both units are non-linear with stress. Figure 2.2 presents a schematic of the Burgers body.

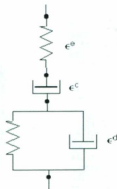


Figure 2.2: Burgers body - idealized viscoelastic model for ice.

The spring in the Maxwell unit represents the instantaneous elastic strain in ice under load. The dashpot in the Maxwell unit represents the viscous, or secondary, creep strain. The Kelvin unit represents delayed-elastic, or primary creep, strain. For the condition of uniaxial stress, the total strain in ice is given by the summation of these three components:

$$\mathcal{E} = \mathcal{E}^e + \mathcal{E}^d + \mathcal{E}^c \quad (2.1)$$

The elastic strain is simply a function of the axial stress (σ) and the Young's modulus of the ice (E_m), which, in the case of the Burgers' body, is the spring constant in the Maxwell unit. The equation for elastic strain is given by:

$$\dot{\epsilon}^e = \frac{\sigma}{E_m} \quad (2.2)$$

The delayed-elastic and viscous creep strain rates are given by:

$$\dot{\epsilon}^d = \frac{\sigma}{\mu_k} \quad (2.3)$$

$$\dot{\epsilon}^c = \frac{\sigma}{\mu_m} \quad (2.4)$$

where μ_k is the viscosity coefficient of the Kelvin unit and μ_m is the viscosity coefficient of the Maxwell unit. The dashpots for both units may be treated as nonlinear with stress following a power-law stress-dependent relationship as shown below:

$$\mu_k = \left(\frac{\sigma}{\dot{\epsilon}_o^d} \right) \left(\frac{\sigma_o}{\sigma^d} \right)^n \quad (2.5)$$

$$\mu_m = \left(\frac{\sigma}{\dot{\epsilon}_o^c} \right) \left(\frac{\sigma_o}{\sigma} \right)^m \quad (2.6)$$

where $\dot{\epsilon}_o^d$ is a creep reference rate; σ_o is a constant unit stress (1 MPa); σ^d is the stress in the Kelvin unit dashpot; and $\dot{\epsilon}_o^c$ is a creep parameter (Xiao, 1997).

This Burgers model representation with nonlinear dashpots has been used to successfully model primary creep under rapid loading (Jordaan and McKenna, 1988), who also presented the following equation for delayed-elastic strain, which

assumes a nonlinear dashpot and a linear spring in the Kelvin unit and incorporates reduced time:

$$\varepsilon^d(t) = \frac{\sigma}{E_k} \left[1 - \exp \left(- \int_0^t \frac{E_k}{\mu_k(\sigma_d)} d\tau \right) \right] \quad (2.7)$$

with E_k being Young's modulus of the Kelvin unit and $\frac{1}{\mu_k(\sigma_d)}$ being reduced time.

Reduced time is a common method used in viscoelastic theory to take into account nonlinearities in time-dependent processes and modifying them in such a way that linear viscoelastic theory can be applied. This is useful as it allows for complex nonlinear viscoelastic materials to be analyzed with simpler linear theory. In general, the application of linear theory is possible by replacing the time, t , with a reduced time, $\psi(t)$, defined as:

$$\psi(t) = \int_0^t \frac{d\tau}{a_d} \quad (2.8)$$

where, in the case of delayed-elastic strain, a_d is a function of stress. In order to achieve a straight forward analytic solution for Eq. (2.7) the viscosity coefficient must follow the power-law relationship:

$$\mu_k(\sigma_d) = \frac{1}{K\sigma_d^{n-1}} \quad (2.9)$$

where K is a viscosity parameter.

Using the equation of equilibrium for a Kelvin unit Eq. (2.9) can be solved and substituted into Eq. (2.7) to give:

$$\varepsilon^d(t) = \frac{\sigma}{E_k} \left\{ 1 - [(n-1)\alpha t + 1]^{1/(1-n)} \right\} \quad (2.10)$$

where $\omega = \frac{E_k}{\mu_{k0}}$ and μ_{k0} is the viscosity at time $t = 0$.

Multi-axial Loading

In order to model realistically ice for engineering purposes it is essential to consider multi-axial loading. When sea ice in a floe comes into contact with a structure the presence of the surrounding ice floe creates a level of confinement and subjects the ice to multi-axial loads. Under multi-axial loading the deformation of ice can be represented with strain tensors as follows:

$$\varepsilon_{ij} = \varepsilon_{ij}^e + \varepsilon_{ij}^d + \varepsilon_{ij}^c \quad (2.11)$$

The delayed-elastic and viscous creep strain tensors can be broken down into deviatoric (e_{ij}) and volumetric, often referred to as hydrostatic, components (ε_v):

$$\varepsilon_{ij}^d = e_{ij}^d + \varepsilon_v^d \quad (2.12)$$

$$\varepsilon_{ij}^c = e_{ij}^c + \varepsilon_v^c \quad (2.13)$$

The volume change in ice under compression is quite small often making the volumetric components in Eq. (2.12) and (2.13) negligible and assumed to be zero. However, if not assumed negligible the volumetric components can be combined and summed with the elastic strain tensor, the deviatoric delayed-elastic strain and deviatoric viscous strain to give the total strain under multi-axial loading as:

$$\varepsilon_{ij} = \varepsilon_{ij}^e + e_{ij}^d + e_{ij}^c + \varepsilon_{ij}^v \delta_{ij} \quad (2.14)$$

where δ_{ij} is the Kronecker delta function (Li, 2002).

Assuming that the elastic properties of ice are isotropic the equation describing the elastic strain components is given by:

$$\varepsilon_{ij}^e = \frac{-\nu}{E} \sigma_{kk} \delta_{ij} + \frac{1+\nu}{E} \sigma_{ij} \quad (2.15)$$

and ν , being the Poisson ratio for ice, is approximately 0.3.

It must be noted that for multi-axial loading conditions it is necessary to model viscosity coefficients, and effective delayed-elastic and viscous creep deviators, with von Mises stresses as opposed to uniaxial stress.

$$\mu_k = \left(\frac{s}{\dot{\varepsilon}_o^d} \right) \left(\frac{\sigma_o}{s^d} \right)^n \quad (2.16)$$

$$\mu_m = \left(\frac{s}{\dot{\varepsilon}_o^c} \right) \left(\frac{\sigma_o}{s} \right)^m \quad (2.17)$$

$$\dot{\epsilon}_{ij}^d = \frac{3}{2} \dot{\epsilon}_o^d \left(\frac{s^d}{\sigma_0} \right)^n \frac{s_{ij}}{s} \quad (2.18)$$

$$\dot{\epsilon}_{ij}^c = \frac{3}{2} \dot{\epsilon}_o^c \left(\frac{s}{\sigma_0} \right)^n \frac{s_{ij}}{s} \quad (2.19)$$

where the von Mises stress is defined using the stress tensors as, $s = \left(\frac{3}{2} s_{ij} s_{ij} \right)^{1/2}$,

and s^d is the effective stress in the Kelvin unit dashpot and defined by,

$$s^d = s - E_k e^d \quad (\text{Xiao, 1997}).$$

Of particular interest in modeling ice for engineering purposes is the effect of multi-axial loading on strain rate. Ice that is put under very high multi-axial stress states, such as is present during ice-structure interaction, experiences very high strain rates. These strain rates can be as great as 10^7 times those observed in uniaxial loaded specimens at 1 MPa (Jordaan and Taylor, 2011). These increased strain rates mean that the strain accumulated in a solid over a year at low stress may occur in a matter of seconds at high stress. Despite this dramatic increase in strain rate viscoelastic theory still applies.

Dilatation

The equation for the total strain under multi-axial loading conditions was given by Eq. (2.14). The final component to be defined is the combined volumetric strain (ϵ_v) from the delayed elastic and viscous creep strains. In order to determine the volumetric strain it is necessary to study the dilatation of ice during loading and

consequent damage. It was observed during the Hobson's Choice Ice Island medium-scale field tests that the density near the edges of the crushed layer was less than that of the parent ice (Frederking et al., 1990) while the density near the center remained relatively constant. Since it is known that the volume change in ice under compression is quite small it is likely that the change in density near the edge is due to damage (microcracking) of the ice during indentation.

For triaxial load conditions Singh (1993) proposed the following equation for the volumetric strain rate of ice:

$$\dot{\epsilon}_v = \frac{-f_3}{p} (\dot{\epsilon} - \dot{\epsilon}^e) = \frac{-f_3}{p} (\dot{\epsilon}_y^d + \dot{\epsilon}_y^c) \quad (2.20)$$

where f_3 is a constant; p is the hydrostatic pressure; ϵ is the effective total strain under multi-axial load conditions; and ϵ^e is the effective elastic strain.

The final equation for the total strain tensor developed using viscoelastic theory is written as:

$$\dot{\epsilon}_{ij} = \dot{\epsilon}_{ij}^e + \dot{\epsilon}_{ij}^d + \dot{\epsilon}_{ij}^c + \epsilon_{ij}^v \delta_{ij} \quad (2.21)$$

2.2.2 Fracture, Damage, and High Pressure Zones

The result of fracture processes in ice under either tensile or compressive loading can lead to the catastrophic failure of the ice. Fracturing of ice is associated with the transition from elastic and pure continuum creep deformation, often referred to as ductile behaviour, to brittle behaviour. This transition of deformation

mechanisms occurs as a result of a complex interaction of applied strain rate, temperature, load level, and flaws in the ice (Sanderson, 1988).

In nature, ice is formed through geophysical processes and as a result has many internal flaws and irregularities. These inherent defects, or lack thereof, play a significant role in how fracture processes in ice and associated failure are initiated and controlled. Sanderson (1988) explains that a fracture process can be either propagation-controlled or nucleation-controlled.

When ice specimens are grown in the laboratory it is possible to produce them such that they have few or no internal defects or cracks. When this is the case and a load is applied to the ice it will deform causing dislocations to glide within grains and pile-up at grain boundaries resulting in local stress concentrations (Sanderson, 1988). In order to relieve these stress concentrations the grain boundaries will part creating microcracks in the ice and these cracks will be under shear stress. This is referred to as crack nucleation. True crack nucleation requires the increasing of local stress concentrations to levels matching the cohesive or theoretical cleavage strength of the material (Taylor, 2010).

If an applied load induces crack nucleation but the microcracks are too small to propagate then the load must be increased until they do. This is referred to by Sanderson (1988) as a 'propagation-controlled' fracture process. A fracture process is also propagation-controlled if an applied load causes pre-existing defects and cracks, as can be found in naturally formed ice, to propagate due to shear stress. In either instance the propagation of cracks will lead to failure of the

material. If the applied load is great enough to produce large microcracks it may be the case that the cracks will propagate the instant they form. This is referred to by Sanderson (1988) as a 'nucleation-controlled' fracture process.

For a polycrystalline ice specimen subjected to a uniform tensile load Sinha (1982) proposed that the nucleation of a crack is governed by the exceedence of a critical level of delayed-elastic strain, ϵ^d , which is discussed in Section 2.2.1.

Sinha was dealing with low stress levels and low strains, which are not normally the case for ice-structure interaction, and as a result the delayed-elastic strain will always take a finite time to develop suggesting that ice can carry an infinite stress prior to crack nucleation. Ting and Sunder (1985) proposed that crack nucleation is governed by the exceedence of the total tensile strain. Regardless of conditions necessary for crack nucleation during tensile loading, once nucleated a crack is unstable and a single crack will propagate to failure as predicted by linear elastic fracture mechanics criterion. The stress required to nucleate a crack is greater than that required to propagate a crack and therefore the stress required to fracture a specimen with no pre-existing cracks is equal to the required stress for crack nucleation. It should be noted that under slow loading ductile processes at the crack tips complicate matters and linear elastic fracture mechanics does not apply (Sanderson, 1988).

For a polycrystalline ice specimen loaded in compression the nucleation of cracks occurs for the same reasons discussed above for tensile loading. Main differences between the two types of loading are that cracks may nucleate across grains

(transgranular) during compressive loading, compressive loading leads to the formation of wing cracks, and crack propagation may be a stable process when in compression. Schulson (1999) states that the brittle failure of ice under compression is marked by sudden material collapse as a result of macroscopic shear faulting on planes inclined approximately 30 degrees to the direction of principal stress. It can be argued that this observation of shear faulting was a result of the ice specimen interacting with the end platens of the apparatus. In the presence of low confinement (≤ 25 MPa) the brittle compressive strength of ice is greatly increased by the suppression of internal cracks due to the additional confinement. At greater than 25 MPa confinement ice experiences pure creep and damage (Sanderson, 1988). Schulson (1999) describes the brittle compressive failure of ice as a multi-step process:

- 1) Nucleation of cracks at grain boundaries at applied stresses approximately one quarter to one third the failure stress.
- 2) Progressive and generally uniform increase in crack density as load rises.
- 3) Complete failure through sudden formation of one or more macroscopic shear faults.

Shear cracks nucleate due to grain boundary sliding followed by the formation of wing cracks as a result of frictional sliding of the shear cracks (Schulson, 1999). The frictional sliding produces zones of high tensile stress at the ends of the shear crack leading to the formation of wing cracks. The wing cracks will form perpendicular to the initial crack but as they grow they tend to align with the principal axis of compressive stress. Figure 2.3 is a schematic of a typical wing

crack identifying the region of high tensile stress. This alignment is a result of the second principal axis being the highest tension and perpendicular to the applied compressive stress. The final failure of the specimen occurs due to the linkage of a large number of cracks, as opposed to the catastrophic propagation of a single crack as is the case for tensile loading (Sanderson, 1988).

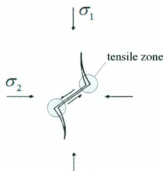


Figure 2.3: Wing crack formation at two grain boundaries in ice under compression (modified from Taylor, 2010).

During interaction with a structure the failure process of the ice has a strong dependence on loading rate. Jordaan and Xiao (1992) describe the relation of failure processes to loading rate using the results of medium-scale field indentation tests with a 1 m diameter spherical indenter. For very slow loading rates, below 0.3 mm/s, the ice near the indenter experienced creep and elastic deformation. This deformation is in the continuum mode and there is no formation of cracks or damage. The failure mode associated with low loading rates is often termed ductile, or secondary creep, failure and can be modeled with viscoelastic theory. When the loading rate was increased to 0.3 mm/s damage

became evident in the vicinity of the indenter and the indenter left a permanent depression in the ice. There was no ejection of material or localized spalling observed, however a large spall developed 20 m in horizontal length. Figure 2.4 is a schematic illustrating the features of the ice deformation at the 0.3 mm/s loading rate. Figure 2.5 is a photograph from the medium-scale field tests showing the permanent depression in the ice as a result of ductile failure.

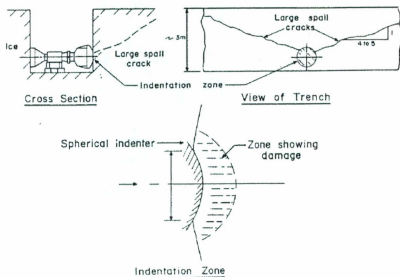


Figure 2.4: Schematic of ice failure for slow loading rate during medium-scale field tests (Jordaan and Xiao, 1992).

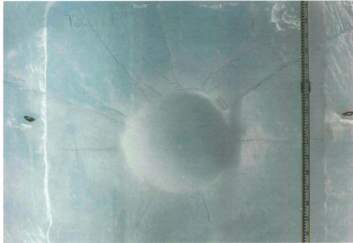


Figure 2.5: Photograph of ductile failure resulting from a 0.3 mm/s loading rate during medium-scale field tests (photo courtesy of Dan Masterson).

When the loading rate of the medium scale tests was increased to 20 mm/s the damage became predominantly isolated in a distinct layer adjacent to the indenter with extrusion and localized spalling observed. The ice in the layer was very fine-grained with microcracking near the edges of the contact zone and regions of highly recrystallized ice near the center (Jordaan and Xiao, 1992). Figure 2.6 illustrates the ice failure mode for high loading rates during the medium scale field tests. Figure 2.7 is a photograph taken during the program showing the damage from indentation at 10 mm/s.

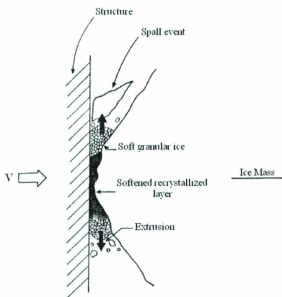


Figure 2.6: Ice failure mode for fast loading rate during medium-scale field tests (modified from Jordaan and Xiao, 1992).

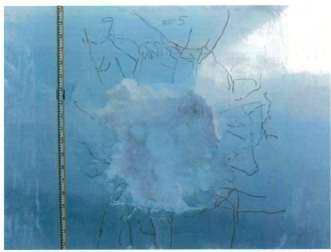


Figure 2.7: Photograph of damage resulting from a 10 mm/s loading rate during medium-scale field tests (photo courtesy of Dan Masterson).

It is at these faster rates, which are more representative of ice-structure interaction, that high pressure zones, or *hpzs*, form and create a narrow layer of microstructurally modified ice at the ice-structure interface. High pressure zones transmit most of the load to the structure and fluctuate in both space and time. Figure 2.8, a schematic of an ice floe interacting with a structure, identifies the presence of areas of high pressure.

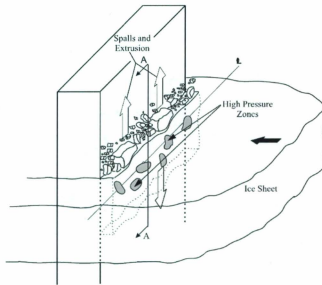


Figure 2.8: Schematic identifying the presence of high pressure zones at an ice-structure interface (Jordaan, 2001).

Local spalling during ice-structure interaction is characterized by the formation of relatively large fragments of ice which occur near high pressure zones and run to a free surface (Taylor, 2010). Figure 2.9 illustrates a typical spalling event for an ice sheet.



Figure 2.9: Typical spalling event for an ice sheet (modified from Sanderson, 1988).

The tendency for these fractures to run to free edges plays a key role in the formation and location of high pressure zones. For example, when an ice sheet interacts with a structure the high pressure zones concentrate away from the free edge and create a “line-load”, which was first discussed by Riska et al. (1990). Jordaan (2001) presented an idealization of high pressure zone distributions for a variety of contact geometries. These idealizations are presented in Figure 2.10.

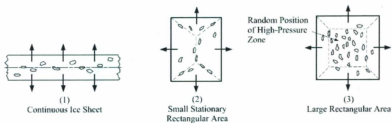


Figure 2.10: Idealization of high pressure zone distribution for common contact geometries (Jordaan, 2001).

These localized zones of high pressure experience triaxial confinement and shear stress leading to microstructural change, or damage, in the ice in the form of microfracture, recrystallization, and pressure melting (Jordaan, 2001). The degree of triaxial confinement in the zone of high pressure varies from low confinement near the edges to high confinement, with contact pressures often reported near

70 MPa, near the center. Li (2002) explained that the different mechanisms of damage in the layer are a result of the addition of the two stress components in the layer. Figure 2.11 can be used to explain how the reported contact pressure is a combination of von Mises stress and confining pressure (i.e. hydrostatic pressure). Near the edges of the layer the confining pressure (4 MPa) is negligible in comparison to the von Mises stress (21 MPa), while in the center of the layer the confining pressure (46 MPa) becomes the dominant of the two components, with von Mises stress at 37 MPa. Between the edge and the center of the layer the components are near equal (von Mises stress = 36 MPa; confining pressure = 31 MPa).

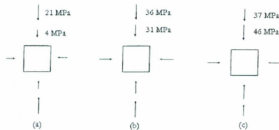


Figure 2.11: Comparison between von Mises and confining pressure in the layer at peak load for: (a) an element at the edge, (b) an element at the middle of the edge and center, and (c) an element at the center.

Jordaan (2001) explains that in the areas of low confinement the damage tends to be dominated by microfracture, while in the central high pressure areas microcracking is suppressed and the damage is dominated by recrystallization and local pressure melting. An alternative theory presented by Gagnon (1994) describes the contact area to have regions of low pressure consisting of crushed

ice and regions of relatively undamaged ice, transparent in appearance, and bearing approximately 88% of the load with pressures greater than 70 MPa. Through the process of thin-sectioning, as described by Sinha (1977), it is clearly shown in both laboratory and field tests that this transparent, high pressure central area, described by Gagnon (1994) to be undamaged, is in fact highly recrystallized; the reader is referred to Frederking et al. (1990), Sinha and Cai (1992), Jordaan and Singh (1994), and Barrette et al. (2002). In order to study high pressure zones it is necessary to have an understanding of damage mechanics. Damage mechanics refers to events leading to a softening of a material due to microstructural change in the material (Jordaan et al., 2005).

Damage results in a layer of considerably softer, or more compliant, ice compared to the parent undamaged ice and leads to increased strain rates during ice-structure interaction. The relative compliance of the ice as a function of confinement is represented in Figure 2.12. It has been theorized that failure of the *hpz* and the resulting extrusion occurs when the soft, low confined areas near the edge meet the soft, highly confined area near the center, and the pulverized ice particles near the edge flow according to Mohr-Coulomb criterion (Jordaan, 2001).

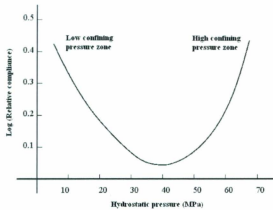


Figure 2.12: Relationship between relative creep compliance of ice and confining pressure (modified from Jordaan et al., 2005).

These damaged layers have been observed in both small scale laboratory tests and medium scale field tests. Figure 2.13 shows the significant similarity between damaged layers at different scales. Jordaan et al. (2012) describe that in modeling the development of the damaged layer the solution is identical at different scales as long as the indentation rate is scaled linearly according to scaling constant λ . The equation for scaling the indentation rate for a prototype (μ_p) from a model (μ_m) is given by:

$$\mu_p = \lambda \mu_m \quad (2.22)$$

Note that near the edges of the damaged layer the ice is opaque and white, a characteristic of areas of dense microfracturing. Near the center of the layer the ice remains translucent and was originally thought to be undamaged, but upon further examination was discovered to be highly recrystallized.

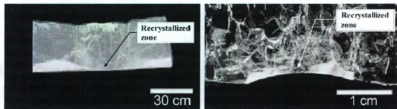


Figure 2.13: Damaged layer at (Left) medium scale and (Right) small scale.

Modeling Damage

A mechanical model to analyze the total strain in multi-axially loaded ice has been reviewed in Section 2.2.1. The next step is to consider the concept of damage and how it affects the constitutive properties of ice. Damage refers to microstructural change in the ice, which may include microcracking (nucleation and growth), dynamic recrystallization, and pressure melting.

One of the first models of damage was developed by Kachanov (1958). For an undamaged specimen with a cross-section, A_0 , in uniaxial loading, P , the stress is given by:

$$\sigma = \frac{P}{A_0} \quad (2.23)$$

In the presence of damage (cracks) an amount of the cross-sectional area becomes associated with cracks, A , and thus a smaller area, $A_0 - A$, carries the load and results in an effective stress, σ_{eff} :

$$\sigma_{eff} = \frac{P}{A_o - A} = \frac{P}{A_o(1-D)} \quad (2.24)$$

The parameter D is referred to as the damage variable and is defined as:

$$D = \frac{A}{A_o}; \quad 0 \leq D \leq 1 \quad (2.25)$$

This treats damage only as a function of crack density which will not hold true for all brittle materials under all loading conditions.

Schapery (1981) developed a damage state variable, S , and formulated a continuum damage theory similar to the J-integral. The J-integral developed by Rice (1968) used non-linear elasticity theory to approximate elastoplastic response to account for plasticity of the tip of a crack during fracture.

Schapery (1981) used correspondence principals to develop a fracture theory for non-linear viscoelastic materials based on modeling elastic theory and accounted for the effects of damage using the damage state variable presented below.

$$S = \int_0^t f_1 \left(\frac{\sigma}{\sigma_o} \right)^q d\tau \quad (2.26)$$

The constant, f_1 , is a function of stress and reflects the properties of the material.

Treating ice as a continuum and assigning a finite number of points in the continuum a state variable (S) allows for the constitutive properties of the model to vary in both space and time.

In order to account for the effect of confining pressure on damage, Singh (1993) modified Schapery's damage variable equation to include a hydrostatic confining pressure dependent variable $f_1(p)$. The revised equation is written as:

$$S = \int_0^t f_1(p) \left(\frac{\sigma}{\sigma_0} \right)^q d\tau \quad (2.27)$$

This method was compared against experimental results by Xiao and Jordaan (1996) and proved to have good agreement with theoretical results. Jordaan later introduced the use of two state variables in order to account for high loading stresses and confining pressures (Jordaan et al., 1997). Two functions of pressure are used in this equation, $f_1(p)$ for low pressures and $f_2(p)$ for higher pressures:

$$S = \int_0^t \left(f_1(p) \exp \left(\frac{\sigma}{\sigma_2} \right)^{q_1} + f_2(p) \exp \left(\frac{\sigma}{\sigma_2} \right)^{q_2} \right) d\tau \quad (2.28)$$

Figure 2.14 shows how the functions of pressure correspond to damage rate. Note the similarity between Figures 2.12 and 2.14. The relative compliance in Figure 2.12 is directly related to the rate of damage in Figure 2.14.

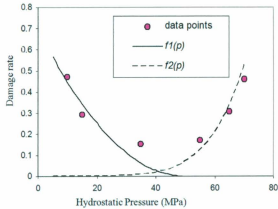


Figure 2.14: Damage rate versus hydrostatic pressure (Jordaan et al., 1994).

A factor to account for the creep enhancement of inelastic strain due to damage is introduced through the equations for delayed-elastic and viscous creep strain.

Xiao and Jordaan (1996) defined the enhancement as an exponential function of Schapery's damage state variable (S), and a creep enhancement factor constant (β) in combination with Glen's Law:

$$\dot{\epsilon} = c \left(\frac{\sigma}{\sigma_o} \right)^n \exp(\beta S) \quad (2.29)$$

The equations for the effective delayed-elastic and viscous elastic deviatoric strain rates are now re-written as:

$$\dot{\epsilon}_{ij}^{d,e} = \frac{3}{2} \dot{\epsilon}_o^d \left(\frac{s^d}{\sigma_o} \right)^n \frac{s_{ij}}{s} \exp(\beta_d S) \quad (2.30)$$

$$\dot{\epsilon}_{ij}^{v,e} = \frac{3}{2} \dot{\epsilon}_o^v \left(\frac{s}{\sigma_o} \right)^n \frac{s_{ij}}{s} \exp(\beta_v S) \quad (2.31)$$

The equation for the total strain tensor using viscoelastic theory given in Eq. (2.21) can be redefined incorporating the effect of damage on the constitutive properties of ice:

$$\dot{\epsilon}_{ij} = \dot{\epsilon}_{ij}^e + \dot{\epsilon}_{ij}^{d'} + \dot{\epsilon}_{ij}^{c'} + \dot{\epsilon}_{ij}^v \delta_{ij} \quad (2.32)$$

2.3 Ice-structure Interaction

Since the early 1960s much of the motivation and funding for research in the field of ice-structure interaction has been driven by the demand for exploration and development of offshore oil and gas fields in the Arctic. In the 1970s significant oil reserves were discovered in Prudhoe Bay, Alaska, and on the Canadian Beaufort Shelf. In the Canadian Beaufort drillships were able to operate during the summer season but for the most part these areas are ice covered for the majority of the year limiting the use of drillships. To cope with this limitation industry initially built artificial islands and utilized shore-based drilling equipment, making it possible to conduct exploratory drilling in the near-shore zone. Moving ice sheets would break up on the beaches and form grounded rubble piles (Jeffries et al., 2008). Over time, exploration moved further offshore into deeper waters making artificial islands impractical and leading to the development of caisson type structures. Caisson structures were often constructed with vertical, or near vertical, sides and when subjected to the action of drifting ice floes the ice would crush directly against the caisson walls.

When drifting ice floes crush against vertical sided offshore structures several different kinds of interactions may occur. Four distinctly different ice-structure interaction types have been observed at full-scale and also during medium- and small-scale indentation tests. Kärnä (1994) describes the structural response, in the form of displacement, to different interaction types and the associated ice conditions as follows (Figure 2.15):

- a) Response to ductile ice failure, at very low ice velocities.
- b) Quasi-static response followed by transient vibration, at low ice velocities
- c) Steady-state vibration in conditions where the ice fails by crushing, at medium ice velocities
- d) Random response due to nonsimultaneous ice crushing, at high ice velocities

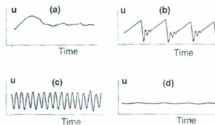


Figure 2.15: Typical structural responses, in the form of displacement, during interaction with drifting ice floes at various speeds (Kärnä, 1994).

Cyclic response during ice-structure interaction is a part of almost all ice loading events on vertical sided structures, even in uniform ice sheets (Blenkarn, 1970).

Regular cyclic loading of offshore structures may cause resonance and load amplification, vibrations of flare booms and other superstructure, and disturb working conditions onboard.

A characteristic of ice that plays a salient role in the different interaction types discussed above is the strong dependence of ice strength on strain rate, or loading rate of the ice. Ice loading data taken from the Molikpaq, a steel caisson structure deployed in the Canadian Beaufort Sea in the 1980s to drill exploratory wells, show that loads can increase when ice velocity drops below 0.1 m/s, and the interaction subsequently transitions from non-simultaneous crushing to phase-locked, or quasi-static, loading (Jefferies et al., 2008). The compliance of the structure, specifically deflection at the waterline, also plays an important role in the vibratory response during ice-structure interaction. The storage and dissipation of energy during deflection and spring back, respectively, of the structure introduces structural feedback and varies the relative loading rates experienced by the ice.

At low ice velocities a quasi-static loading pattern develops, as depicted in Figure 2.15 (b). The name refers to the fact that loads are not amplified by the dynamics of the structure. This pattern has also been referred to in literature as “saw-tooth loading”, “ratcheting”, “phase-locked crushing”, “intermittent crushing”, and “alternating ductile-brittle crushing”. During quasi-static response the ice interaction process is composed of load cycles incorporating both ductile and brittle ice behaviour. Blenkarn (1970) and Määttäinen (1977) share a similar explanation for this process. At full-scale and under slow loading rate, when an ice floe comes into first contact with an offshore structure the structure deflects under load decreasing the ice loading rate and subsequently increasing ice

strength. During this initial loading the ice exhibits ductile behaviour. As the floe advances the deflection of the structure as well as the ice load gradually increases, until the resistance of the deflected structure exceeds the maximum strength of the ice. At this point the ice fails and the structure springs back releasing its stored energy creating an increase in the relative loading rate and a decrease in ice strength. During this spring back stage the ice crushed and extruded. Following spring back the structure may experience transient oscillations near its natural frequency until the ice edge advances enough to begin another load up stage, and the cycle repeats.

One of the best examples of quasi-static interaction at full-scale is the Molikpaq loading event on May 12, 1986, when a 2 – 3 m thick first-year ice floe crushed past the caisson structure. Figure 2.16 shows a ten second window of the loading record on the Molikpaq. The interaction is initially non-simultaneous crushing but as the drifting ice floe slowed from near 0.09 m/s to 0.02 m/s a quasi-static interaction became well established (Jefferies et al., 2008). The load record was recorded using three instrumented loading zones and the acceleration record was recorded an accelerometer mounted near the top of a bulkhead.

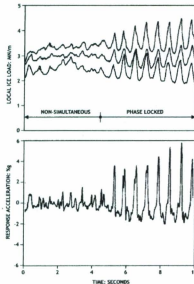


Figure 2.16: Instrumented loading zones (Top) and acceleration record (Bottom) showing transition from a non-simultaneous to quasi-static loading pattern recorded during a May 12, 1986 loading event on the Molikpaq (modified from Jefferies et al., 2008).

When offshore structures experience steady-state vibrations, as depicted in Figure 2.15 (c), the associated forces are often amplified by the dynamics of the structure and accelerations occur near constant amplitude (Kärnä, 1994). This phenomenon has been observed in full-scale structures in Cook Inlet, Alaska (Blenkarn, 1970) and in field measurement programs in the Baltic Sea (Määttänen, 1978). The Cook Inlet structures were instrumented test piles and the Baltic Sea structures were channels markers, both of which are slender narrow structures. Kärnä and Turunen (1990) propose that steady-state vibrations exist only when the ice velocity is between two transitional values. While in this steady-state range the structural response is amplified by the ice-structure interaction with a large

amount of data suggesting the structure oscillates at a frequency 5% to 15% lower than its natural frequency (Kärnä, 1994). Figure 2.17 presents the structural accelerations of a channel marker in the Baltic Sea during steady-state ice-structure interaction. Kärnä states that ice forces are magnified by the dynamics of the structure during steady-state vibration.

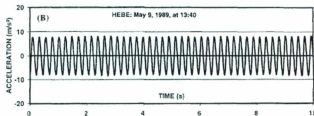


Figure 2.17: Steady-state structural response of a channel marker in the Baltic Sea (Kärnä, 1994).

At higher ice velocities nonsimultaneous ice failure may develop. The failure processes across the width of the ice-structure interface become random and cause decrease in the total load. Due to the random nature of nonsimultaneous failure a cyclic loading pattern does not develop.

2.4 Previous Indentation Test Programs

Small-scale laboratory testing is seen as a cost effective approach to analyzing ice failure mechanics and associated structural interaction. Observations seen at small-scale are then linked to full-scale observations and applied to the design of offshore structures for arctic and other ice prone regions. There exists a vast amount of literature and data on small-scale ice-structure interaction. A selection

of experimental approaches and results will be presented in this section, highlighting similarities and differences in observed ice-structure interaction.

Two different experimental programs have recently been conducted by Barrette et al. (2002) and Wells et al. (2010) investigating ice failure mechanics through indentation with a spherical indenter simulating a single, stationary high-pressure zone. Both sets of results show evidence of load cycling attributable to dynamic activity in the damage layer. A significant difference between the two programs is that Wells indented unconfined ice specimens in order to study the effects of fracture on high pressure zone behaviour.

Barrette et al. (2002) conducted ice indentation tests on freshwater, polycrystalline ice specimens with grain size between 3.35 to 4.75 mm. The specimens were confined in cylindrical steel molds (155 mm and 200 mm in diameter) and indented with a 20 mm diameter spherical steel indenter. This indenters used by both Barrette and Wells were modeled after the indenter used in the Hobsons' Choice Ice Island medium-scale tests (Frederking et al. 1990) and scaled down by a factor of 50. Tests were conducted to investigate the effects of temperature and loading rate on the load response of a single high-pressure zone and to analyze the physical characteristics of the damage layer produced in the ice adjacent to the indenter. Tests were conducted at -2°C , -10°C , and -20°C , with indentation rates ranging from 0.1 to 10 mm/s and with a penetration depth of 2.6 mm. Following indentation tests Barrette used the double-microtome technique

developed by Sinha (1977) to produce thin-sections of the indented area and assess the microstructural damage present in the ice.

Load cycling was observed in a number of tests and Barrette described these as consisting of three different frequency domains, as depicted in Figure 2.18.

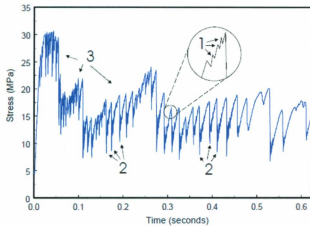


Figure 2.18: Three frequency domains observed during indentation of a confined ice specimen (courtesy of Paul Barrette).

The first (Frequency Domain 1) occurs near frequencies of 500 ± 100 Hz with maximum amplitudes corresponding to test at -20 °C. Frequencies in this domain peaked at 1000 Hz in tests conducted at -20 °C and 10 mm/s. Barrette believes this high frequency response is a result of microfracturing processes. However, frequencies above 500 Hz are unlikely to occur during ice-structure interaction and this frequency domain may be attributable to transient vibrations in the indentation system. When compared with other indentation tests, which used a compliant indentation system, (see for instance Gagnon, 1994) high frequency

domains were determined to be a result of resonant oscillations in the indentation system. The second frequency domain discussed (Frequency Domain 2) cycled at 150 to 200 Hz with amplitudes between 1 and 3 kN and seemed to occur most frequently at indentation rates of 4 mm/s, and occurred rarely at -2 °C. Barrette associated this load cycling pattern to dynamic activity in the layer adjacent to the indenter. A third frequency domain identified (Frequency Domain 3) appears as periodic drops disrupting the 150 to 200 Hz cycling pattern and is associated with spalling and radial cracking.

During load cycles in the 150 to 200 Hz domain fine-grained pulverized ice was ejected from the indentation area. Tests at the lowest indentation rate showed less extrusion but was dominated by microfracturing. This observation is consistent with other small-scale ice indentation tests which identified ductile behaviour at slow rates of indentation and a transition to brittle behaviour as rates increase; the reader is referred to Sodhi and Nakazawa (1990), Jordaan (2001), and Kärnä et al. (2008).

The indented surface of each test was characterized by a central dark zone with lighter areas on the perimeter. Thin-sections were taken for the majority of tests and showed the dark zone to be an area of recrystallized ice with the lighter regions being heavily microfractured, as described by Jordaan (2001). This damage layer was present in tests at all temperatures however those at -2 °C showed little evidence of microfracture, tests at -10 °C showed a central

recrystallized zone with microfracture near the edges, and tests at $-20\text{ }^{\circ}\text{C}$ were dominated by microfractures.

Indentation tests by Wells et al. (2010) were similar to those presented by Barrette et al. (2002). A similar indenter was used (a scaled down version of the Hobsons' Choice Ice Island medium scale indenter) to simulate a single, stationary high pressure zone, and tests were conducted on polycrystalline, freshwater ice specimens. Wells procedure differed from Barrette in that a vacuum mold was used to eliminate any bubbles in the ice, and the specimens were not confined. A key aspect of Wells' experiment was the use of a tactile pressure sensor to record pressure distribution at the ice-indenter interface. This provided valuable data used for classifying failure processes associated with load drops during a test, as well as dynamic activity of the high pressure zone. Tests were conducted at $-10\text{ }^{\circ}\text{C}$, with indentation rates ranging from 0.2 to 10 mm/s, and penetration depths ranging from 3 to 20 mm.

The failure behaviour of the ice was found to have a strong dependence on loading rate. Five different failure types were observed and classified and are identified in the load record presented in Figure 2.19. At slow speeds, 0.2 to 2 mm/s, failure was dominated by ductile behaviour with force and contact area rising steadily with time. Although ductile is the commonly used to describe this failure mode it is more akin to a damage enhanced creep response, as opposed plastic yielding which is classically associated with ductile failure. At speeds between 2 and 5 mm/s a mix of ductile behaviour and crushing failure was

observed. Crushing failure was classified as either isolated crushing events or repeated crushing events (also referred to as cyclic loading). Isolated crushing refers to a drop in load accompanied by a reduction of pressure in the central region of the high pressure zone and little to no change in the contact area. Immediately preceding the drop in load is an extrusion of crushed ice particles from the perimeter of the indentation zone. This is identical to the process of high pressure zone failure described by Taylor et al. (2008). Cyclic loading refers to regular dynamic activity with a visible increasing trend in the load trace and this pattern is not interrupted by other failure processes. At speeds between 8 and 10 mm/s brittle behaviour dominated and was characterized by localized spalling behaviour. The fifth failure type described by Wells was mixed-mode failure. This was characterized by a combination of crushing and localized spalling and was evident in all tests with rates above 2 mm/s.

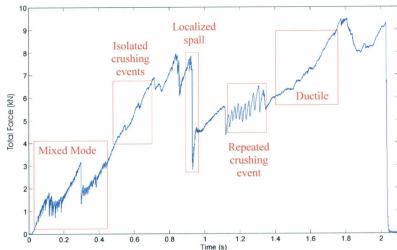


Figure 2.19: Load record identifying five different failure modes associated with compressive ice failure (wells et al., 2010).

Tests conducted by Wells et al. (2010) provide strong evidence of the dependence of ice failure modes on indentation rate as well as the fact that there exist two different processes of ice failure during interaction with a structure, fracture and damage.

Small-scale laboratory tests have also been conducted with compliant structures. These results provide valuable data for full-scale design as all real structures have some degree of compliance. Sodhi and Nakazawa (1990) indented freshwater, fine-grained, columnar ice sheets (15 – 57 mm thick) with a single-degree-of-freedom compliant system. The widths of the indenting portion of this structure ranged from 50 to 150 mm wide. Various indentation rates and structural stiffnesses were tested. Based on the results three basic modes of ice behaviour were described: creep deformation at low indentation rates, intermittent crushing at intermediate rates, and continuous crushing at high rates, as in Kärnä (1994) above.

The process of intermittent crushing described by the authors is identical to that described by Blenkarn (1970) and Määttänen (1977) for full-scale quasi-static interaction. The compliance of the structure allows for the transition of relative indentation rates leading to ductile ice behaviour during the loading phase (low relative velocity) followed by brittle ice behaviour during the spring back phase (increased relative velocity). Based on these small-scale tests with structural

compliance the frequency of intermittent crushing was found to increase with an increase in indentation rate and structural stiffness. This increase in frequency continues until it reaches a value equal to the natural frequency of the structure, at which point it locks into this frequency and is dominated by the resonant response of the structure.

Kärnä et al. (2008) indented columnar ice sheets, 73 to 98 mm thick, with a vertical, compliant indentation structure. The modes of ice failure produced were similar to those discussed by Sodhi and Nakazawa (1990). Kärnä et al. (2008) also noted that during intermittent crushing at low indentation speeds (below 100 mm/s) the total load on the structure can increase as much as two times the load experienced during continuous brittle crushing at higher speeds (above 100 mm/s). A similar result was found by Singh et al. (1990) through indentation of laboratory grown ice sheets with a flexible, vertical structure. Singh observed that maximum excitation forces decreased with an increase in the interaction rate. Speeds above 100 mm/s were required by Kärnä to achieve continuous brittle crushing because his indentation structure was very flexible. Offshore oil and gas structures are much stiffer and would not require such high speeds to experience continuous brittle crushing. Once in the range of continuous brittle crushing the ice load shows very little variation with increasing indentation rate.

Chapter 3: Experimental Methodology

3.1 Overview

3.1.1 Physical Problem

Sea ice and icebergs present significant engineering challenges for the exploration and development of hydrocarbon fields in ice-prone regions around the world.

Designing for ice is an important issue pertaining to the safety of these structures, and as such, it has driven much of the research in the field over the last 30+ years.

For more northerly regions, such as the Beaufort Sea, Barents Sea, Bohai Bay, and Cook Inlet, to name a few, ice is much more prevalent and the interaction of offshore structures with drifting ice floes is of particular concern in design.

During the interaction of a vertically sided structure with a drifting ice floe the structural system can experience significant vibrations associated with the compressive failure of ice, and crushing in particular. The consequences of such dynamic loading are: possible structural vibration, resonance, load amplification,

and serviceability aspects such as human comfort and use of computers. Two factors that have a definite effect on ice-induced vibration are structural compliance at the waterline and the loading rate of the ice. See Chapter 2, Figure 2.16 for an example of ice-induced vibrations at full-scale recorded during a 1986 loading event on the Molikpaq structure in the Canadian Beaufort.

When an ice feature interacts with a compliant structure there is an energy flux into and out of the structure. Energy is stored elastically in the structure as the ice advances and deflects the structure and as deflection increases so to does the load experienced at the ice-structure interface. Stored energy is dissipated through local ice failure processes, and also through elastic rebound of the structure at the moment the strength of the ice is exceeded by the increasing structural resistance. Due to the elastic deflection and rebound of the structure the relative loading rate on the ice varies between decreased rates during initial deflection and increased rates during rebound. These alternating loading rates may change the processes by which the ice fails and it is therefore essential that the nature of local ice failure processes be understood.

Failure processes in ice tend to limit load build-up within the ice and therefore limit the loads applied to the structure. During the interaction of ice with a vertically sided structure the loads are often limited by a combination of spalling fracture and crushing. Spalls typically result in an appreciable, asymmetric area loss and are primarily dependent on stress, geometry, and internal flaws. Crushing, which refers to the pulverization and extrusion of ice and is associated

with damage process within the high pressure zones, is typically observed as a sudden decrease in high-pressure zone intensity without an appreciable shift in position (Taylor et al., 2008). The schematic in Figure 3.1 shows the pressure distribution before and after a localized failure for (a) crushing, and (b) spalling.

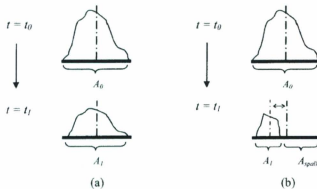


Figure 3.1: Schematic of pressure distribution before ($t = t_0$) and after ($t = t_1$) localized failure for (a) crushing, and (b) spalling. (Taylor et al., 2008)

During ice-structure interaction it is through these localized areas of high pressure that loads are primarily transmitted to the structure (Jordaan, 2001) and therefore it is essential that the nature of these high pressure zones be understood in order to determine design loads for structures. High pressure zones exhibit significant variation in both space and time and typically cover only a small portion of the nominal interaction area. For example the pressure distribution data from the Japan Ocean Industries Association (JOIA) medium-scale field indentation tests show that on average only 10% of the nominal contact area is actually loaded during crushing events (Taylor et al., 2008). It is also known that when ice sheets

interact with a structure high pressure zones tend to take on a 'line-like' distribution (Frederking, 2004).

Within these high pressure zones very high local contact pressure can occur. Taylor et al. (2008) gives a good summary of some of the high contact pressure values reported in the literature. Indentation tests on multi-year ice have produced recorded pressures as high as 80 MPa (Frederking et al., 1990) and 50 MPa (Masterson et al., 1993). Small-scale indentation tests on polycrystalline freshwater ice have produced pressures as high as 100 MPa (Mackey et al., 2007; Jordaan et al., 2008). Pressure values of 70 MPa have been reported during ship ram tests (Jordaan, 2001).

It has been hypothesized by Jordaan (2001) that load drops during periods of crushing are associated with the failure of high pressure zones and that cyclic loading is a result of the varying processes in the vicinity of high pressure zones. As the load carried by a high pressure zone increases the extent of damage also increases and the microstructurally modified layer becomes considerably softer than virgin, undamaged ice. Upon failure of the high pressure zone and subsequent release of pressure the layer hardens. This cycle of pressure softening and hardening of the layer results in a cyclic loading pattern. Figure 3.2 illustrates the cyclic response of a high pressure zone during crushing failure of ice as described by Jordaan (2001).

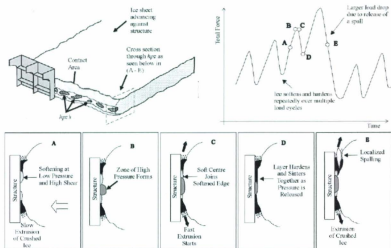


Figure 3.2: Cyclic processes in the vicinity of a single high pressure zone during crushing failure of ice (Jordaan et al., 2008).

Two salient aspects of ice-induced vibration on structures that need attention are the localized failure processes in the ice and the effect of structural feedback on these processes.

3.1.2 Rationale for Small-scale Laboratory Testing

When a drifting ice floe comes into contact and crushes against the vertical walls of an offshore structure the structure is subjected to multiple high pressure zones. The response of the structure upon failure of one high pressure zone may trigger the failure of adjacent high pressure zones. This makes the interactions between a structure and multiple high pressure zones very complex. It is therefore necessary to first understand the mechanical process of a single high pressure zone and then

apply this knowledge to the more complex scenario of multiple high pressure zones.

Recent small-scale laboratory tests, completed by Barrette et al. (2002) and Wells et al. (2010), have successfully modeled a single, stationary high pressure zone to study its effect on the failure pattern observed during compressive ice failure. The indenters used by both Barrette et al. (2002) and Wells et al. (2010) were spherical, steel indenters modeled after the indenters used in the Pond Inlet medium-scale field tests (Frederking et al., 1990) and scaled down by factors of 50 and 25. Wells et al. (2010) also incorporated tactile pressure sensors in her experiments to study the pressure distribution at the ice-indenter interface. A snapshot of the pressure distribution for a 20 mm diameter spherical indenter indenting polycrystalline ice is shown in Figure 3.3. It can be seen that the high pressure zone simulated at small-scale consists of a very high pressure central region with decreasing pressure with distance from the center. This matches the characteristics of a full-scale high pressure zone as describe by Jordaan (2001).

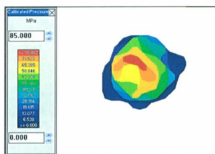


Figure 3.3: Pressure distribution of a simulated high pressure zone produced with a 20-mm diameter steel indenter (Wells et al., 2010).

High pressure zones are found over a wide range of scales and their physical characteristics remain remarkably similar. It is this similarity of the zones at different scales that makes small-scale experimentation a cost-effective approach for studying the processes responsible for the formation and evolution of high pressure zones at full-scale. The microstructural characteristics of the damaged layer can be observed by taking a thin-section through the damaged layer (see for example Barrette et al., 2002). Figure 2.13 in Chapter 2 shows two thin-sections through high pressure zones at different scales with remarkably similar microstructural characteristics. At both scales the central region appears translucent, but in fact it consists of a fine-grained, recrystallized microstructure, and the edges of the damaged layer appear white and are associated with regions of dense microfracture.

Barrette et al. (2002) and Wells et al. (2010) both indented polycrystalline, freshwater, ice specimens with identical spherical, steel indenters. The major difference between the two experiments was that Barrette housed ice specimens in steel, cylindrical confining rings. It was this confinement that allowed Barrette to consistently produce very regular cyclic loading, where as Wells achieved cyclic loading patterns on occasion but most often the lack of confinement caused the ice specimens to fracture prior to the development of cyclic loading patterns. From these two experiments it can be seen that cyclic loading during compressive ice failure must be studied through indentation of confined ice specimens. Figure 3.4 is a photograph of Barrette's indentation system, installed on the Materials

Testing System (MTS) at Memorial University with a 300 mm diameter confined ice specimen mounted on the MTS ram.

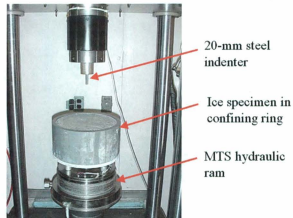


Figure 3.4: A photograph of the indentation system and an ice specimen used by Paul Barrette at Memorial University.

Tactile pressure sensors have proven to be an effective technology for observing the pressure variations and failure mechanisms within a high pressure zone during load cycling. Through the use of tactile pressure sensor data taken from the JOIA program (see for example Takeuchi et al., 1997; Sodhi et al., 1998; and Akagawa et al., 2000) Taylor et al. (2008) observed that high pressure zones formed during medium-scale indentation of an ice-sheet vary significantly in space and time, while maintaining a “line-like” distribution. Examination of pressure distributions at medium-scale (Taylor et al., 2008) and small-scale (Wells et al., 2010) in conjunction with their associated load traces have identified load limiting failure mechanisms, including spalling, pulverization, and extrusion, to be linked to load drops.

An example of how tactile pressure sensors can be used to link cyclic load drops to the failure of a high pressure zone during small-scale indentation testing is presented in Figure 3.5. Examining the load trace in Figure 3.5 (e) and the associated pressure distributions, Figure 3.5 (a, b, c, and d), it can be seen that each load drop is associated with a decrease in the intensity of the high pressure central region, and a loss of contact area around the periphery of the high pressure zone associated with extrusion of pulverized material. If, on the other hand, the load drops were related to spalling fractures, as opposed to high pressure zone failure, it would appear in the pressure distribution as a significant loss of contact area and a shift in the location of the region of high pressure.

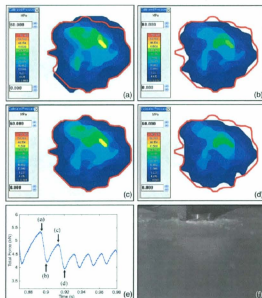


Figure 3.5: Changes in pressure distribution in a high pressure zone are linked to cyclic loading during a small-scale indentation test (Wells et al., 2010).

Another salient aspect of compressive ice failure during ice-structure interaction is the effect of structural feedback. Full-scale ice-structure interactions occur in the presence of structural feedback and it is therefore essential that structural feedback be a factor when studying compressive ice failure at small-scale. During an interaction energy is stored in the structure through elastic deflection and is dissipated through failure processes in the ice. Kärnä et al. (2008) describes the waterline displacement of an offshore structure as being the explanatory parameter in the magnification of ice loads during intermittent crushing events. Through the design of a compliant indentation system structural feedback can be introduced into the system and controlled at small-scale in order to study the effect of structural feedback, the different modes of ice-structure interaction, and theories such as of load magnification during cyclic loading.

3.2 Experimental Design

Through small-scale laboratory experiments the present research investigates the effects of loading rate, structural feedback, and temperature on the compressive failure of ice in the vicinity of a high pressure zone. Three central questions that guide this research are:

- 1) How does loading rate affect the frequency, amplitude, and duration of cyclic loading patterns produced during compressive ice failure at different temperatures?
- 2) How does structural feedback (the storage and dissipation of energy through structural deflection) affect the frequency, amplitude, and duration of cyclic loading patterns produced during compressive ice failure at different temperatures?

- 3) What influence does the formation, evolution, and failure of high pressure zones and the occurrence of spalls and fractures have on the observed cyclic loading patterns produced during compressive ice failure?

The research is divided into two separate phases. The first phase, Phase 1A, consists of the indentation of confined ice specimens in the presence of structural feedback. Similarly, the second phase, Phase 1B, includes indentation tests on confined ice specimens but in the absence of structural feedback.

To properly study the phenomenon of ice-induced vibration certain relevant information must be collected during each test. Measurements include the total force and pressure distribution at the ice-indenter interface, structural deflection, and the ambient testing temperature. Emphasis is also placed on the internal structure of the ice and analysis of the nature of the damaged layer at the laboratory scale. All testing, sample preparation, and post-test work was conducted in the cold room facilities at the National Research Council – Institute for Ocean Technology (NRC-IOT).

3.2.1 Overview of Test Set-up

In order to study the effect of structural feedback on the ice crushing process, tests were conducted using both compliant and rigid indentation systems. In Phase 1A structural feedback was analyzed by designing indentation systems that would deflect elastically under load. The indentation systems were designed as simply-supported beams with an attached indenter. Different levels of structural compliance and natural frequency were achieved by varying the lengths of the compliant beams. Phase 1B consisted of rigid indentation systems with two

different sized indenters, 20 mm and 40 mm in diameter, attached directly to the MTS load cell to eliminate compliance.

In general, when conducting laboratory experiments the essential aspects of the phenomenon being studied must be duplicated. In order to study compressive ice failure in the vicinity of a high pressure zone during ice-structure interaction at small-scale the following aspects were addressed:

- A single, stationary high pressure zone was simulated using a small-scale, steel, spherical indenter to indent the ice.
- A simple structural indentation system was designed to introduce compliance into the system.
- Ice was grown in the laboratory and confined to suppress splitting.

A single, stationary high pressure zone can be simulated in the laboratory through indentation with a small, spherical, steel indenter. This technique was successfully employed during recent small-scale studies of indentation failure (the reader is referred to Barrette et al. (2002) and Wells et al. (2010)). The indenters used in the present research are 20 and 40 mm in diameter with radii of curvature of 25.6 and 51.2 mm, respectively. These are scale models of the medium-scale indenters used during Pond Inlet field tests (Frederking et al., 1990). The 20 mm indenter is scaled by a factor of 50 and the 40 mm indenter is scaled by a factor of 25.

Polycrystalline, freshwater ice was chosen as the ice type for these experiments as it has a consistent, isotropic microstructure, similar to glacial ice. This makes it an ideal ice type for experimental testing because it can be consistently reproduced. Another benefit of polycrystalline, freshwater ice is that it is commonly used in

laboratory testing thus allowing for comparison with other experimental results. Phase 1A used crystals in the size range of 3.35 to 4.75 mm in diameter and Phase 1B used a size range of 2.00 to 3.35 mm. The ice produced for the present research was molded and confined in steel confining rings to suppress fracture and splitting of the ice sample during testing. Two different sized confining rings were used with diameters of 150 mm and 300 mm and are shown side-by-side in Figure 3.6.



Figure 3.6: Steel confining rings, 150 mm (Left) and 300 mm (Right) in diameter, used to suppress splitting of ice specimens.

Loads and loading rates are applied to the indenters and controlled using a Materials Testing System (MTS) located in the Large Cold Room at NRC-IOT. The confined ice specimens are mounted and secured to a stainless-steel platen attached to the hydraulic ram of the MTS. The hydraulic ram (rated for 250 kN) is instrumented with an internal linear variable differential transformer (LVDT) and controls the vertical displacement of the platen and attached specimen. The ram operates in a closed-loop system to maintain accurate displacement control. The

indentation system, whether compliant or rigid, is secured to the MTS crosshead (rated for 1 MN of force) and remains stationary throughout each test. Figure 3.7 is a photograph of a compliant indentation system and a confined ice specimen mounted to the MTS.

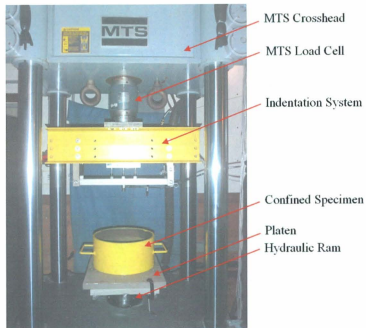


Figure 3.7: Photograph of indentation system and confined specimen mounted to the MTS.

3.2.2 Test Structure for Phase 1A

Indentation Systems

The first series of tests, Phase 1A, was aimed at identifying the conditions which trigger dynamic ice failure for a single high pressure zone during indentation of a

confined ice specimen in the presence of structural feedback. Structural feedback was introduced through simple structural indentation systems which transmitted loads to the indenter. The general arrangement of the testing system designed for Phase 1A is shown in Figure 3.8.

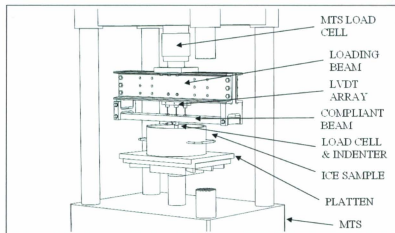


Figure 3.8: General arrangement of the testing system used in Phase 1A.

Polycrystalline freshwater ice specimens with randomly oriented crystals, 3.35 to 4.75 mm in diameter, were grown and confined in 300 mm diameter steel molds and secured to a stainless steel platen attached to the hydraulic ram of the MTS. Ice samples were clamped to the platen in three different locations to ensure the samples did not move during testing. The vertical displacement (indentation rate) of the specimen is controlled by regulating the rate of extension of the hydraulic ram.

To investigate the effects of structural feedback four structural indentation systems were constructed to introduce different levels of compliance. The indentation systems have been designed as compliant steel beams simply-supported by a loading beam. Three compliant beams were fabricated at different lengths to produce a range of compliances and natural frequencies. The loading beam consists of two back-to-back C7 x 9.8 steel channels. Both the compliant beams and loading beam channels were fabricated from 55W-grade steel. Attached to the underside of each compliant beam was a stainless steel indenter 20 mm in diameter with a radius of curvature of 25.6 mm. The compliant beams were attached to the loading beams by pinned end connections fitted with needle roller bearings to allow the ends to freely rotate with little frictional resistance. To prevent any axial tensile forces developing in the beam when it deflects under load one end connection was designed as a yoke mechanism allowing it to rotate in a plane parallel to the compliant beam. Figure 3.9 shows photographs of the two end connections.



Figure 3.9: Photographs of the pinned end connections. The rotating end connection is shown on the right.

Table 3.1 presents the dimensions, design stiffness values, and design natural frequencies associated with the three compliant beams. These design values were calculated using simply-supported beam equations. Figure 3.10 is a drawing of the indentation system showing the three different compliant beams used in Phase 1A.

Table 3.1: Theoretical properties for Phase 1A indentation systems.

	Compliant System 1	Compliant System 2	Compliant System 3
Length (m)	0.756	0.476	0.300
Width (m)	0.100	0.100	0.100
Height (m)	0.030	0.030	0.030
Stiffness (N/m)	5.00E+06	2.00E+07	8.00E+07
Natural Frequency (Hz)	120	303	763

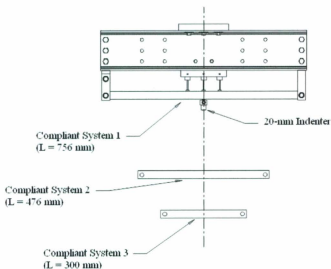


Figure 3.10: Compliant beam combinations used for Phase 1A.

The fourth indentation system designed for Phase 1A was aimed at being perfectly rigid, however it was determined through system characteristic tests that

it in fact had an amount of compliance and deflected under load. This configuration, referred to as Compliant System 4, consisted of Compliant System 1 (the longest compliant beam) fitted with 4 aluminum blocks positioned symmetrically between the compliant beam and the loading beam. The aluminum blocks were intended to eliminate any deflection that would occur in the compliant beam. A photograph of Compliant System 4 showing the positioning of the aluminum blocks is provided in Figure 3.11.

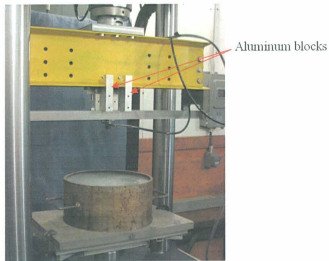


Figure 3.11: Photograph of Compliant System 4 identifying position of aluminum blocks. Two blocks are located in the front and two in the back.

All indentation systems are attached to the MTS by mounting the loading beam to the MTS load cell with a steel adapter plate. The load cell is in turn attached directly to the MTS crosshead.

Each of the four compliant indentation systems was subjected to two system characteristic tests to determine their actual stiffness values and natural frequencies. The first test, called a Stress-Strain test, loaded the indentation system between 0 and 10 kN at a constant loading rate for several cycles. The structural deflection recorded during this test was used to determine the actual value of structural stiffness. For the second test an impact load was applied to the underside of the compliant beam while the system was mounted to the MTS. The transient vibration of the system following the impact was recorded to determine the actual natural frequency values of the systems. Table 3.2 presents the measured stiffness values and measured natural frequencies for each indentation system in Phase 1A and the data plots for each set of system characterization tests are included in Appendix B.

Table 3.2: Measured properties for Phase 1A indentation systems.

	Compliant System 1	Compliant System 2	Compliant System 3	Compliant System 4
Length (m)	0.756	0.476	0.300	0.756*
Stiffness (N/m)	3.89E+06	9.61E+06	1.46E+07	1.50E+08
Natural Frequency (Hz)	100	140	250	210

* Compliant beam is fitted with aluminum blocks to increase stiffness

Instrumentation and Data Acquisition

A collection of instrumentation and recording devices were required for Phase 1A in order to analyze the structural response, pressures, loads, and ice failure mechanisms at play during each indentation test.

Structural response was measured using an array of linear variable differential transformers (LVDTs). The LVDTs measured deflection in the compliant beams at three different locations along their length. By knowing the deflection of the structure near the indenter it is possible to determine the relative indentation rate for any given time during a test. The relative indentation rate is of interest because it is known that ice strength has a strong dependence on loading rate.

The LVDTs used for Phase 1A were Series 230, Model 0235-0000, A.C. LVDTs with a working range of ± 6.35 mm, temperature stability to -55 °C, and are light weight making them ideal for the high structural accelerations expected during the indentation tests. The three LVDTs were positioned in a row along the length of the top side of the compliant beam, spaced 75 mm apart, with the middle LVDT located directly over the center of the indenter. They were mounted in an aluminum LVDT block secured between the channels of the loading beam. The LVDT core rods were threaded into small aluminum blocks that were secured to the top of the compliant beams with an epoxy adhesive. The photograph in Figure 3.12 shows the location and installation of the LVDT array.

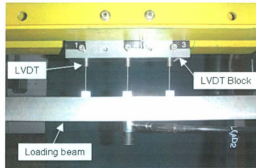


Figure 3.12: Photograph showing the location of the LVDT array.

Loads were measured at two different locations: at the ice-indenter interface, and at the point where the indentation system attaches to the MTS. To measure loads at the ice-indenter interface a Model 31 High Range Miniature Load Cell was located between the 20 mm indenter and the underside of the compliant beam. The miniature load cell has a load capacity of 13 kN which is just above the maximum expected loads for these indentation tests. Maximum expected loads were determined to be between 9 and 10 kN, based on results from similar indentation tests with a 20-mm diameter indenter conducted by Barrette et al. (2002). This load cell has temperature stability to $-53\text{ }^{\circ}\text{C}$ making it suitable for cold room experiments.

The second load measurements were recorded by the MTS Series 661 Load Cell located between the MTS crosshead and the attachment point of the indentation system. This load cell is part of the MTS and its associated control system and therefore was not specifically chosen for these experiments. The load cell is rated for 250 kN and has temperature stability to $-46\text{ }^{\circ}\text{C}$. The capacity of this load cell

is roughly 25 times greater than the expected maximum loads and the location is not ideal for analyzing ice-structure interaction forces. For these reasons, the MTS load cell measurements in Phase 1A are used primarily to ensure consistency of the miniature load cell. The calibration records for the miniature load cell and three LVDTs are included in Appendix C. Figure 3.13 shows the locations of the two load cells.

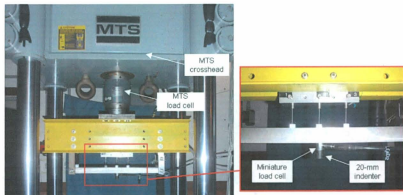


Figure 3.13: Photographs of location of miniature and MTS load cells.

Two HP Compaq DC 7100 computers installed with GEDAP 7.0 software were used for the data acquisition of the three LVDTs and both load cells. Data was acquired with an IOTech Daqboard 2000 data acquisition system with 16 bit resolution at sampling rates of 12,500 and 20,000 Hz in Phase 1A.

Pressure distribution at the ice-indenter interface is measured using the Tekscan I-Scan pressure measurement system. This system consists of a very thin, flexible tactile pressure sensor which has a matrix of individual sensing elements, referred to as “sensels”, which record static and dynamic interface pressure distributions

over the area covered by the sensor. Model 5051 sensors were used for these indentation tests which have a pressure rating of 172 MPa and a resolution of 62 sensels/cm². Pressure data is transmitted and stored in an external PC through a Tekscan USB handle at a rate of 100 Hz. Data recorded with the sensor can be played back as a movie file allowing for analysis of the relative variations in pressure distribution within a high pressure zone throughout an indentation test. To improve the accuracy of the Tekscan measurements the data from each test was post-calibrated based on the load cell data for that test. A description of the calibration procedure is included in Appendix C. The photograph in Figure 3.14 shows the placement of the tactile pressure sensor between the indenter and the top surface of the ice sample prior to an indentation test.

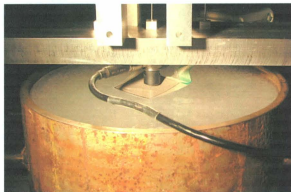


Figure 3.14: Photograph showing the positioning of a Tekscan tactile pressure sensor.

Both high-speed and regular video were recorded during each test. The high-speed black-and-white video had a close range view of the indenter and ice surface to capture visually failure processes and extrusion of pulverized ice during

indentation. The regular video had a view of the entire indentation system. High-speed video was recorded on a Photron ABXRX camera with a frame rate of 3000 frames per second and stored on a Panasonic Toughbook 30 installed with Photron FASTCAM 3 software. Regular video was recorded and stored using a Sony Digital 8 color camcorder.

3.2.3 Test Structure for Phase 1B

Indentation Systems

The second series of tests, Phase 1B, was aimed at identifying the conditions which trigger dynamic ice failure for a single high pressure zone during indentation of a confined ice specimen in the absence of structural feedback. The absence of structural feedback is the primary distinction between Phase 1A and Phase 1B. To eliminate structural response during dynamic loading tests were conducted using rigid indentation systems.

Tests were conducted with 20 mm and 40 mm diameter indenters. For the 20 mm indenter tests the indenter was mounted to two solid steel blocks plus the steel adapter plate which mounted directly to the MTS load cell. The photograph in Figure 3.15 shows the mounting arrangement for the 20 mm indenter. The additional steel blocks were required to provide enough vertical clearance between the indenter tip and the MTS crosshead to ensure the top edge of the confining rings did not come into contact with the crosshead during indentation.

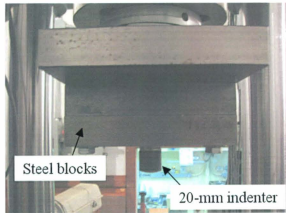


Figure 3.15: Photograph of 20 mm rigid indentation system.

For the 40 mm indenter tests the indenter was designed to mount directly to the MTS load cell without an adapter plate. Figure 3.16 presents the design drawing for the 40 mm indenter and a photograph of the indenter mounted to the MTS.



Figure 3.16: 40 mm indenter design drawing (Left); Photograph of 40 mm rigid indentation system (Right).

Three system characteristic tests were conducted: a Stress-Strain test (as described in Section 3.2.2) for each of the two rigid systems, and a third test to measure the

transient response of the MTS after a sudden drop in load. For this test a thin wire was secured to the MTS crosshead and the hydraulic ram and the wire was subjected to a linearly increasing load until the wire snapped. An LVDT internal to the MTS (located at the base of the hydraulic ram and records the extension of the ram) would record any transient response of the MTS displacement. There was no transient response observed and this is due to the control system of the MTS. The data plots for each system characterization test are included in Appendix B.

When the MTS is in "Displacement-Control" mode, as it is during an indentation test, it is operating on a closed-loop system. It is given a manually adjusted command control signal (static or dynamic) and the MTS LVDT measures the position of the hydraulic ram. If there is a difference between the command signal and the signal from the LVDT, a signal to the control valve causes the difference to be corrected. From the wire test it was determined that when the MTS is operating in "Displacement-Control" mode it effectively isolates any transient structural response between the control points (i.e. between the top of the crosshead and the bottom platen) and thus the indentation systems simulate perfectly rigid structures.

Polycrystalline freshwater ice specimens with randomly oriented crystals, 2.00 to 3.35 mm in diameter, were grown and confined in 150 mm diameter steel confining rings and secured to a stainless-steel platen attached to the hydraulic ram of the MTS. Ice samples were clamped to the platen in three different

locations to ensure the samples did not move during testing. Vertical displacement (indentation rate) of the specimen is controlled by regulating the rate of extension of the hydraulic ram.

Instrumentation and Data Acquisition

A reduced set of instrumentation was required for Phase 1B as there was no need to measure structural response. Therefore the miniature load cell and the LVDT array were not used.

Loads were measured using the MTS Series 661 Load Cell, rated for 250 kN. The MTS load cell is located between the indenter and the MTS cross head and can be seen in Figure 3.11. Indentation displacement was recorded using the MTS internal LVDT. Similar to Phase 1A two HP Compaq DC 7100 computers installed with GEDAP 7.0 software were used for data acquisition and storage. Data was acquired with an IOTech Daqboard 20000 with a 16 bit resolution at a sampling rate of 10,000 Hz.

The Tekscan I-Scan system was also used in Phase 1B to measure the pressure distribution at the ice-indenter interface. Model 5051 sensors were used which have a pressure rating of 172 MPa and a resolution of 62 sensels/cm². The pressure data was transmitted and stored in an external PC through the Tekscan USB handle at a rate of 100 Hz.

High-speed and regular video were recorded for each test. Black-and-white high-speed video was recorded on a Photron ABXRX camera at a frame rate of 3000

frames per second and stored on a Panasonic Toughbook 30 installed with Photron FASTCAM 3 software. The regular video was recorded using a Sony Digital 8 color camcorder.

3.3 Ice Specimen Preparation

Polycrystalline, freshwater ice specimens for both experimental phases were produced from 136 kg blocks of commercially purchased, bubble-free, sculptor's ice. All ice production work was conducted at -11 °C in the Small Cold Room at NRC-IOT. An ice saw was used to cut the blocks into manageable pieces and these were stored in the Small Cold Room. With the use of a bandsaw the bubble-free ice was cut into "fingers" roughly 30 cm in length with a cross-section of 3 cm x 2 cm. These "fingers" were then fed into an industrial ice crusher and the crushed ice was sieved to produce seed ice in the size range of 2.00 to 3.35 mm or 3.35 to 4.75 mm. The seed ice was then stored in insulated coolers until it was ready for use. Photographs of the bubble-free ice, bandsaw, industrial ice crusher, and the sieve are shown in Figure 3.17.



Figure 3.17: Photographs of Small Cold Room equipment: (a) bubble-free sculptor's ice, (b) bandsaw, (c) industrial ice crusher, and (d) sieve.

Steel, cylindrical, confining rings were used to mold the ice specimens (see Figure 3.7). A thin, plastic membrane was secured around the bottom of the rings using high vacuum silicone grease and all-weather vinyl electrical tape, which maintains conformability to $-18\text{ }^{\circ}\text{C}$, to ensure a water-tight seal. Seed ice was then placed into the rings to a depth of 5 cm and the rings were flooded with distilled water at a temperature between 0 and $2\text{ }^{\circ}\text{C}$. Care was taken to flood the molds below the waterline to minimize the amount of air entrained in the specimens. The mixture was stirred to allow the seed to form a uniform ice cover

at the surface. The specimens were placed on polystyrene foam sheets and left to freeze for at least two days. The polystyrene foam insulated the bottom of the specimens promoting preferential ice growth from the top and sides of the specimen inward. This directional freezing caused the bottom surface, which was against the plastic membrane, to bulge, while the top surface remained level with only slight irregularities. The bulged surface was leveled flush with the bottom surface of the ring using a warm steel plate. One day prior to testing the ice specimens were placed in insulated coolers, brought to the Large Cold Room, and left over night at the target test temperature.

3.4 Testing Procedure

All indentation tests for Phase 1A and Phase 1B were conducted using the Materials Testing System (MTS) which is housed in the Large Cold Room (LCR) facilities at the National Research Council – Institute for Ocean Technology (NRC-IOT). Prior to testing, prepared specimens were stored in the LCR at the target test temperature over night, for a minimum of 16 hours.

Tests were conducted at temperatures ranging from -5°C to -15°C , with indentation speeds ranging from 2 mm/s to 10 mm/s and maximum penetration depths of 2.5 mm and 10 mm. The specimen being tested was mounted on a stainless-steel platen attached to the hydraulic ram of the MTS and positioned such that the indenter would make contact in the center of the top surface of the

ice. To ensure the specimen did not shift horizontally during testing it was secured to the platen at three different locations using clamping systems.

Tests were controlled using the MTS control system and data collected with the data acquisition system. The MTS control system, data acquisition system, associated computers, and video monitors were located just outside the LCR. As described in Section 3.2 the indentation system is attached to the MTS crosshead through the MTS load cell and remains stationary during the tests. A Tekscan tactile pressure sensor is placed on the top surface of the ice directly below the indenter. The hydraulic ram, used to control the vertical displacement and indentation rate of the specimen, is raised until the indenter just touches to surface of the ice, which corresponds to the first sign of a load reading from the Tekscan film. The specimen is then backed-off slightly to give enough distance between the indenter and the ice surface to allow for the displacement rate to reach its required speed prior to first contact.

At the beginning of each test the load and displacement recordings are synchronized with the high-speed video by a one-shot synchronizing electronic pulse sent to the high-speed video camera.

Following each indentation test the hydraulic ram is lowered and the specimen is removed from the MTS. The indented area of the specimen is extracted from the confining ring and a thin-section is taken through the indented area to allow for observation of the microstructural characteristics in the damaged layer. The

process of specimen extraction and thin-sectioning is described in Section 3.5 below.

3.5 Thin-sectioning Procedure

To study the microstructure of the damaged layer a thin-sectioning technique, developed by Sinha (1977), was employed which made use of a microtome. This technique was developed to optically examine the grain and sub-grain structure of sea ice.

Following each test the first step in the thin-sectioning process was to extract the portion of the ice containing the indented area. A milling machine with a half inch bit, located in the Large Cold Room, was used to plunge the depth of the ice specimen and cut out a rectangular prism. This portion of ice was then lifted out of the confining ring, sealed in a plastic zipper bag in an insulated cooler, and brought to the Small Cold Room for storage. Figure 3.18 shows a photograph of the milling machine in use.



Figure 3.18: Photograph of an indented area being extracted using the milling machine in the Large Cold Room.

Once in the Small Cold Room a thick section of ice is cut vertically through the indented area using the bandsaw. One side of the thick section is sanded level with a mesh sanding sheet on top of a steel plate that had been machined flat. The thick section is then mounted on a clear glass slide with the sanded surface against the glass. Drops of water are used to freeze-weld the ice to the glass. The microtome has an attached pump that creates a suction to secure the glass slide to the “shuttle” of the microtome. The “shuttle” is manually moved back and forth passing the exposed surface of the ice across a precision sharpened steel knife. The thickness cut from the ice with each pass can range from 1 to 30 μm . The

photograph in Figure 3.19 shows the microtome located in the Small Cold Room at NRC-IOT.

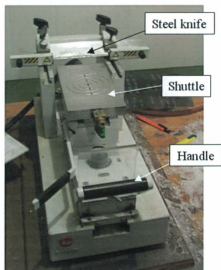


Figure 3.19: Photograph of the microtome located in the Small Cold Room.

The microtoming process can be broken down into several stages. First, 30 μm thick cuts are removed from the exposed surface until the ice section is cut down to the desired region of the indented area. After this, fifteen passes of the knife are taken with 5 μm cuts, and then fifteen passes with 1 to 2 μm cuts. After each pass a fine bristled paint brush is used to wipe snow off the knife. At this point the exposed surface of the ice section is a near "mirror finish", as described by Sinha (1977). A razorblade is used to cut the freeze-welding locations to remove the section from the glass slide. The section is flipped and mounted on a new, clean glass slide with the prepared surface now against the glass. The section is

permanently freeze-welded to the glass slide by using a continuous bead of water along all sides of the section except the side with the indentation. Starting with 30 μm cuts the newly exposed surface is reduced until the section is roughly 1 mm thick. Cuts are reduced to 5 μm for several passes and then 1 to 2 μm . The final thin-section is between 0.2 and 0.5 mm.

The final thin-section is labeled with the appropriate test name and is brought to the lighting booth for photographs with a Nikon D100 digital-SLR camera. Three photographs are taken for each thin-section: once with cross-polarized light transmitted through the section, once with regular light reflected from the side of the section, and a combination of these two lighting techniques. Cross polarized light allows for observation of the crystal structure of the ice and can be used to identify regions of recrystallization, which appear unmodified when viewed with regular lighting. Side-lighting exposes grain boundaries and in particular makes areas of dense microfracture appear white. After photographing the thin-sections are preserved in plastic zipper bags and stored in insulated coolers in the Small Cold Room.

3.6 Summary

A total of 44 indentation tests were completed throughout Phase 1A and Phase 1B in an effort to improve our understanding of compressive ice failure mechanics during ice-structure interaction. Being able to simulate a high pressure zone at small-scale and knowing that the microstructural characteristics of a high pressure

zone are similar across a wide range of scales allowed for a cost-effective approach to studying compressive ice failure in the laboratory.

Ice specimens used in both phases were confined in cylindrical, steel confining rings in order to prevent splitting of the specimens. Structural compliance was introduced through the design of compliant indentation systems and allowed for the study of the effects of structural feedback in compressive ice failure. The internal structure of the ice and the characteristics of the damaged layer were assessed through the process of thin-sectioning. Collected data included: load traces, structural deflection, interfacial pressure distribution, and regular and high-speed video.

Chapter 4: Experimental Results

4.1 Overview

Due to the large number of indentation tests performed throughout Phases 1A and 1B only a sample of the results from each of the two phases are presented in this chapter. An exhaustive collection of test results are presented in Appendix A.

A single, stationary high pressure zone was successfully modeled using a spherical, steel indenter to indent polycrystalline ice specimens. One of the objectives of this research was to investigate how loading rate affects frequency and amplitude of cyclic loading patterns produced during compressive failure of ice. A typical result for each of the three indentation speeds tested in Phases 1A and 1B is presented in this chapter. For Phase 1A the time traces for indenter load and structural deflection are provided. For Phase 1B structural compliance was not a factor and only the indenter load is presented. A second objective was to gain insight into the role that the formation, evolution, and failure of a high

pressure zone has on the observed cyclic loading patterns. During periods of cyclic loading images taken from the tactile pressure recordings are used to demonstrate the failure mechanisms associated with specific load drops. Photographs of thin-sections taken through the damaged regions of the ice specimens are provided showing the highly modified crystal structure of the ice in the vicinity of the indentation zone. Also presented is a typical warm ice result obtained in Phase 1A and a typical result obtained with the larger 40 mm diameter indenter in Phase 1B.

The naming convention used for both phases identifies details of the parameters used for each individual test. Figure 4.1 provides an example of the structure of the naming convention.

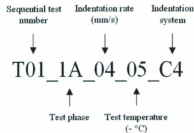


Figure 4.1: Test naming convention example

4.2 Results from Phase 1A

The first series of tests, Phase 1A, consisted of 31 tests aimed at identifying the optimal conditions which trigger dynamic ice failure for a single high pressure zone during indentation of a confined ice specimen. Factors varied were

temperature, indentation rate, and structural compliance of the indentation system and collected data included force records, structural deflection, interfacial pressure distribution, and high speed video. Thin-sections were taken through the damaged regions to assess the microstructural characteristics in the indentation zone. A sample of the data from Phase 1A is presented below.

4.2.1 Test Matrix – Phase 1A

The matrix for the first series, Phase 1A, initially consisted of twenty four tests; half at $-5\text{ }^{\circ}\text{C}$ and half at $-15\text{ }^{\circ}\text{C}$, and at loading rates of 4, 7, and 10 mm/s. In the original twenty four tests four levels of structural compliance were tested using the four indentation systems described in Section 3.2.2. Loading rate values were chosen based on analysis of Barrette et al. (2002) in which he achieved high amplitude, high frequency, ice-induced vibrations with indentation tests similar to the present research. All tests had a maximum indentation depth of 2.5 mm.

Seven additional tests were added to Phase 1A, and based on examination of the results from the first twenty four tests it was decided to change the testing temperature to $-10\text{ }^{\circ}\text{C}$ to match more closely conditions used by Barrette et al. (2002) to attain dynamic ice crushing behaviour. Having realized that Compliant System 4, which was originally intended to be rigid, had an amount of compliance, three rigid tests were conducted. A rigid system was achieved by removing the indentation system and mounting the indenter, inline with the miniature load cell, to an adapter plate attached to the MTS load cell. All seven additional tests were conducted at 4 mm/s, and included repeat tests. This was

done to better establish the conditions necessary for the generation of cyclic crushing during indentation.

Tactile pressure sensors have proven useful for observing interfacial pressure distributions and for determining failure mechanisms. A trade-off associated with using tactile pressure sensors is that the sensors cover the ice surface surrounding the indentation zone and block the line of sight of the high-speed video. For this reason tactile pressure data was not collected for all tests. The test matrix in

Table 4.1 presents the list of indentation tests completed for Phase 1A.

Table 4.1: Test Matrix for Phase 1A.

Test	Indentation System	Disp. Rate (mm/s)	Temp. (°C)	Sampling freq. (Hz)	Tactile pressure data
T01_1A_04_05_C4	C.S. 4	4	-5	12500	Yes
T02_1A_07_05_C4	C.S. 4	7	-5	12500	Yes
T03_1A_10_05_C4	C.S. 4	10	-5	12500	Yes
T04_1A_04_05_C1	C.S. 1	4	-5	12500	Yes
T05_1A_07_05_C1	C.S. 1	7	-5	12500	Yes
T06_1A_10_05_C1	C.S. 1	10	-5	12500	No
T07_1A_04_05_C2	C.S. 2	4	-5	12500	No
T08_1A_07_05_C2	C.S. 2	7	-5	12500	Yes
T09_1A_10_05_C2	C.S. 2	10	-5	12500	Yes
T10_1A_04_05_C3	C.S. 3	4	-5	12500	Yes
T11_1A_07_05_C3	C.S. 3	7	-5	12500	Yes
T12_1A_10_05_C3	C.S. 3	10	-5	12500	Yes
T13_1A_04_15_C4	C.S. 4	4	-15	12500	Yes
T14_1A_07_15_C4	C.S. 4	7	-15	12500	No
T15_1A_10_15_C4	C.S. 4	10	-15	12500	Yes
T16_1A_04_15_C1	C.S. 1	4	-15	12500	Yes
T17_1A_07_15_C1	C.S. 1	7	-15	12500	Yes
T18_1A_10_15_C1	C.S. 1	10	-15	12500	Yes
T19_1A_04_15_C2	C.S. 2	4	-15	12500	Yes
T20_1A_07_15_C2	C.S. 2	7	-15	12500	No
T21_1A_10_15_C2	C.S. 2	10	-15	12500	Yes
T22_1A_04_15_C3	C.S. 3	4	-15	12500	Yes
T23_1A_07_15_C3	C.S. 3	7	-15	12500	Yes
T24_1A_10_15_C3	C.S. 3	10	-15	12500	Yes
T25_1A_04_10_R	Rigid	4	-10	20000	Yes
T26_1A_04_10_R	Rigid	4	-10	20000	No
T27_1A_04_10_R	Rigid	4	-10	20000	Yes
T28_1A_04_10_C4	C.S. 4	4	-10	20000	No
T29_1A_04_10_C4	C.S. 4	4	-10	20000	Yes
T30_1A_04_10_C3	C.S. 3	4	-10	20000	No
T31_1A_04_10_C3	C.S. 3	4	-10	20000	No

It should be noted that tests: T06_1A_10_05_C1, T07_1A_04_05_C2, and T19_1A_04_15_C2 were interrupted when the MTS tripped on tensile saturation of the MTS load cell. This was a result of spring-back of the indentation system causing a tensile load on the MTS load cell. This was corrected by increasing the maximum allowable tensile load in the MTS load cell from 1 kN to 5 kN.

4.2.2 Slow Speed Test (4 mm/s)

The time series data from the miniature load cell and the middle LVDT for indentation test T16_1A_04_15_C3 is shown in Figure 4.2. This test was conducted with Compliant System 3 at an indentation rate of 4 mm/s and a test temperature of -15°C . Both the force record from the miniature load cell and the mid-length structural deflection record from the LVDT show a very regular cyclic loading pattern developed at approximately 0.28 seconds into the test. The load cycling frequency is close to 20 Hz, although it decreases with time as contact area increases with indentation depth. The average load drop for each cycle is approximately 2.5 kN and the maximum load achieved is 6.1 kN.

Three consecutive load drops in the force-time series are identified in Figure 4.2 with arrows (a) and (b), (c) and (d), and (e) and (f). Images from the pressure distribution data corresponding to before and after each load drop are presented in Figure 4.3. Going from images (a) to (b) and (c) to (d) in Figure 4.3 it can be seen that there is a decrease in the intensity of the high pressure zone without an appreciable shift in position or loss of contact area and thus the failure mechanism associated with these two load drops is high pressure zone failure. The failure

mechanism associated with the third load drop is spalling fracture. Going from image (e) to (f) in Figure 4.3 it can be seen that the high pressure zone vanishes and there is a significant loss of contact area.

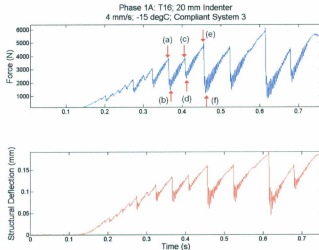


Figure 4.2: Miniature load cell and LVDT data for test T16_1A_04_15_C3 showing total force on the indenter (Top) and structural deflection (Bottom).

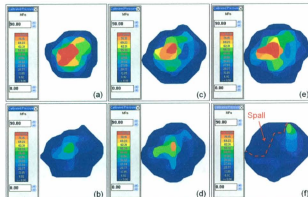


Figure 4.3: Pressure distribution images corresponding to the load drops identified in force-time trace in Figure 4.2.

Photographs of the thin-section taken through the damaged zone from test T16_1A_04_15_C3 are shown in Figure 4.4. The top image is taken using the side-lighting technique and the bottom photograph is taken through cross-polarized transmitted light. Both photos show evidence of a damaged layer with the top photo revealing the layer that is heavily dominated by zones of microfracture, which appear white and opaque under side lighting. A region just left of the center of the damaged layer appears translucent in the top photo but when viewed through cross-polarized light can be seen to have a fine-grained, recrystallized microstructure.

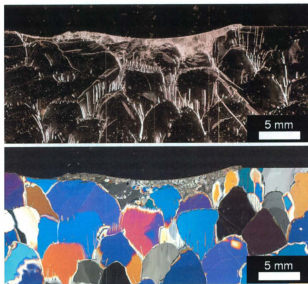


Figure 4.4: Thin-section of damaged zone from test T16_1A_04_15_C3 photographed with side lighting (Top) and through cross-polarized light (Bottom).

4.2.3 Medium Speed Test (7 mm/s)

The time series data from the miniature load cell and the middle LVDT for indentation test T17_1A_07_15_C3 is shown in Figure 4.5. This test was conducted with Compliant System 3 at an indentation rate of 7 mm/s and a test temperature of -15°C . Both the force data from the miniature load cell and the structural deflection data from the LVDT show a cyclic loading pattern developed at approximately 0.2 seconds into the test. The load cycling frequency from 0.2 to 0.3 seconds is near 55 Hz, and decreases to approximately 30 Hz from 0.3 to 0.45 seconds. The average load drop for each cycle in the second half of the test (0.3 to 0.45 seconds) is approximately 3 kN and the maximum load achieved is 6.3 kN. Three load drops in the force-time series are identified in Figure 4.5 with arrows (a) and (b), (c) and (d), and (e) and (f). Images from the pressure distribution data corresponding to before and after each load drop are presented in Figure 4.6. The failure mechanism associated with the first two load drops considered is high pressure zone failure. Going from images (a) to (b) and (c) to (d) in Figure 4.6 it can be seen that there is a decrease in the intensity of the high pressure zone without an appreciable shift in position or loss of contact area. The failure mechanism associated with the third load drop appears to be a combination of high pressure zone failure and spalling fracture. Going from image (e) to (f) in Figure 4.6 it can be seen that the high pressure zone loses intensity and does not shift position but there is also a significant loss of contact area.

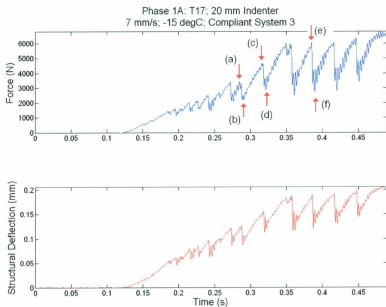


Figure 4.5: Miniature load cell and LVDT data for test T17_1A_07_15_C3 showing total force on the indenter (Top) and structural deflection (Bottom).

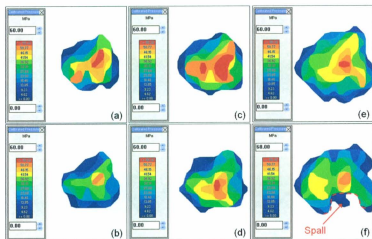


Figure 4.6: Pressure distribution images corresponding to the load drops identified in the force-time trace in Figure 4.5.

Photographs of the thin-section taken through the damaged zone from test T17_1A_07_15_C3 are shown in Figure 4.7. The top image, taken using the side-lighting technique, shows the layer to be heavily dominated by zones of microfracture. The bottom photograph, taken through cross-polarized transmitted light, shows a small recrystallized zone within the layer to the left of the center. Both photographs show evidence of the damaged layer.

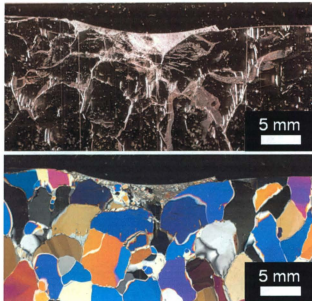


Figure 4.7: Thin-section of damaged zone from test T17_1A_07_15_C3 photographed with side lighting (Top) and through cross-polarized light (Bottom).

4.2.4 Fast Speed Test (10 mm/s)

The time series data from the miniature load cell and the center LVDT for indentation test T18_1A_10_15_C3 is shown in Figure 4.8. This test was

conducted with Compliant System 3 at the fastest indentation rate for Phase 1A, 10 mm/s, and at a test temperature of -15°C . Both the force record and the structural deflection record show a cyclic loading pattern developed at approximately 0.21 seconds into the test and it grew in amplitude and decreased in frequency as the test proceeded. The load cycling began near 118 Hz, and decreased to approximately 60 Hz at 0.3 seconds into the test. The average load drop for each cycle in the second half of the test (0.3 to 0.45 seconds) was approximately 1.8 kN and the maximum load achieved was 6.8 kN.

Tactile pressure data is collected at a rate of 100 Hz and as a result it is not always possible to obtain pressure distribution images at the exact moment of the peak and trough of a load drop. However, six images have been collected over three load cycles in the force-time series and are identified in Figure 4.8 with arrows (a), (b), (c), (d), (e) and (f). The failure mechanism associated with the load cycling appears to be high pressure zone failure. The images are presented in Figure 4.9 and it can be seen that throughout the load cycling the intensity of the high pressure zones fluctuate but their position does not shift and there is no significant decreases in contact area.

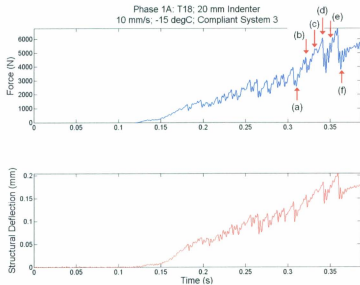


Figure 4.8: Miniature load cell and LVDT data for test T18_1A_10_15_C3 showing total force on the indenter (Top) and structural deflection (Bottom).

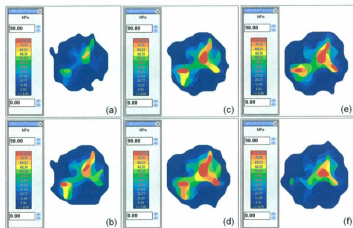


Figure 4.9: Pressure distribution images corresponding to the load drops identified in the force-time trace in Figure 4.8.

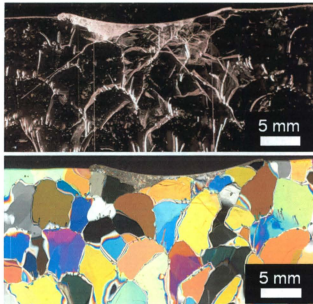


Figure 4.10: Thin-section of damaged zone from test T18_1A_10_15_C3 photographed with side lighting (Top) and through cross-polarized light (Bottom).

Photographs of the thin-section taken through the damaged zone from test T18_1A_10_15_C3 are shown in Figure 4.10. The top image, taken using the side-lighting technique, shows the layer to be almost entirely dominated by zones of microfracture, appearing white and opaque. The bottom photograph, taken through cross-polarized transmitted light, shows little evidence of recrystallization in the layer.

4.2.5 Warm Ice Results (-5°C)

The effect of temperature was also tested in Phase 1A. The first 12 tests were conducted at -5°C , the second half tested at -15°C , and the seven additional tests

at -10°C . The three tests presented above were conducted at -15°C with Compliant System 3 and cyclic loading patterns were evident at 4, 7, and 10 mm/s indentation rates. For tests with warm ice (i.e. -5°C) there was no load cycling evident at any of the indentation rates tested and the ice appeared to fail in the ductile mode. Figures 4.11 to 4.13 show the time series data from the miniature load cell and middle LVDT for indentation tests T04_1A_04_05_C3, T05_1A_07_05_C3, and T06_1A_10_05_C3, respectively.

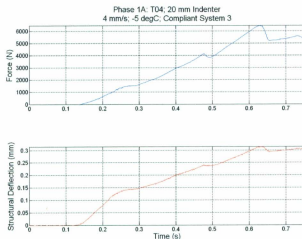


Figure 4.11: Miniature load cell and LVDT data for test T04_1A_04_05_C3 showing total force on the indenter (Top) and structural deflection (Bottom).

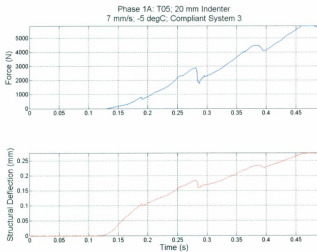


Figure 4.12: Miniature load cell and LVDT data for test T05_1A_07_05_C3 showing total force on the indenter (Top) and structural deflection (Bottom).

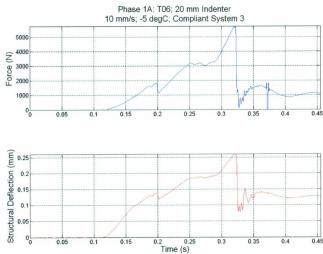


Figure 4.13: Miniature load cell and LVDT data for test T06_1A_10_05_C3 showing total force on the indenter (Top) and structural deflection (Bottom).

Thin-sections for tests T04_1A_04_05_C3 and T05_1A_07_05_C3 are presented in Figures 4.14 and 4.15, respectively. The damaged layer from the thin-section for test T06_1A_10_05_C3 broke apart early in the thin-sectioning process before photographs could be taken and therefore it is not presented below. The damaged layers for both tests shown are heavily dominated by zones of recrystallization, with some microfracturing at either edge of the damaged layer in Figure 4.15.

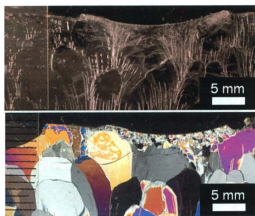


Figure 4.14: Thin-section of damaged zone from test T04_1A_04_05_C3 photographed with side lighting (Top) and through cross-polarized light (Bottom).

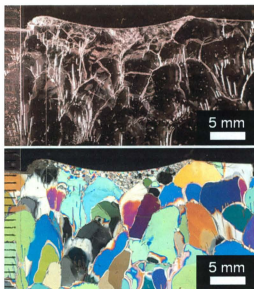


Figure 4.15: Thin-section of damaged zone from test T05_1A_07_05_C3 photographed with side lighting (Top) and through cross-polarized light (Bottom).

4.3 Results from Phase 1B

Building on the results of Phase 1A it was decided to conduct a series of rigid indentation tests. Eliminating structural feedback simplifies the interaction process allowing for identification of the optimal conditions to produce crushed ice and ice-induced vibration. The following list identifies the changes made from Phase 1A to Phase 1B:

- Temperature fixed at -10°C .
- Structural feedback eliminated through use of rigid indentation systems.
- A larger indenter, 40 mm in diameter, was introduced to investigate the effect of indenter size.

- A smaller seed size (2.00 to 3.35 mm in diameter) was used for the production of polycrystalline ice to better match the ratio of ice crystal to indenter size used in medium-scale field tests.
- The diameter of the confining rings was reduced to 150 mm to provide a greater level of confinement.
- The maximum indentation depth was increased to 10 mm to allow more time for the development of cyclic loading and damage processes.

4.3.1 Test Matrix – Phase 1B

The factors analyzed in Phase 1B included indenter size, 20 mm and 40 mm in diameter, and indentation rates, 2, 4, and 6 mm/s, with temperature fixed at -10°C.

The original test matrix consisted of 12 tests using a smaller 150 mm diameter confining ring, and one extra test was conducted taking advantage of a 300 mm diameter ice sample that was left over from Phase 1A. Table 4.2 presents a list of the indentation tests completed for Phase 1B. The same naming convention used for Phase 1A (see Figure 4.1) has been used for Phase 1B and the rigid indentation systems are identified by 'R20' for the 20 mm diameter rigid indenter, and 'R40' for the 40 mm diameter rigid indenter.

Table 4.2: Test matrix for Phase 1B.

Test	Indentation System	Disp. Rate (mm/s)	Temp. (°C)	Sampling freq. (Hz)	Tactile pressure data
T48_1B_02_10_R20	Rigid 20	2	-10	10000	Yes
T49_1B_04_10_R20	Rigid 20	4	-10	10000	No
T50_1B_06_10_R20	Rigid 20	6	-10	10000	No
T51_1B_02_10_R20	Rigid 20	2	-10	10000	Yes
T52_1B_04_10_R20	Rigid 20	4	-10	10000	Yes
T53_1B_06_10_R20	Rigid 20	6	-10	10000	No
T54_1B_02_10_R40	Rigid 40	2	-10	10000	Yes
T55_1B_04_10_R40	Rigid 40	4	-10	10000	No
T56_1B_06_10_R40	Rigid 40	6	-10	10000	Yes
T57_1B_02_10_R40	Rigid 40	2	-10	10000	No
T58_1B_04_10_R40	Rigid 40	4	-10	10000	Yes
T59_1B_06_10_R40	Rigid 40	6	-10	10000	No
T60_1B_04_10_R40	Rigid 40	4	-10	10000	Yes

4.3.2 Slow Speed Test (2 mm/s)

The time series data from the MTS load cell for indentation test T48_1B_02_10_R20 is shown in Figure 4.16. This test was conducted with a 20 mm diameter rigid indentation system at the slowest indentation rate for Phase 1B, 2 mm/s. The force data from the MTS load cell shows little evidence of cyclic loading except for one load drop near the beginning of the test, at approximately 0.25 seconds. The maximum load achieved in the test was 11.8 kN. An enlarged view of the region boxed in red in Figure 4.16 is provided in Figure 4.17. Arrows (a) and (b) point to the peak and trough, respectively, of the 0.5 kN load drop, and the corresponding pressure distribution images are presented in Figure 4.18. This single load drop is a result of high pressure zone failure, characterized by a decrease in the intensity of the high pressure zone without an appreciable shift in position, as seen in Figure 4.18 (a) and (b).

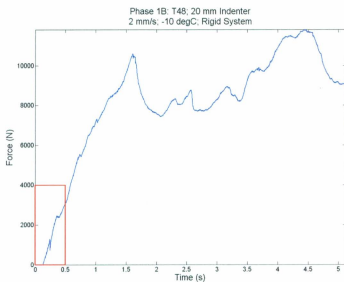


Figure 4.16: MTS load cell data for test T48_1B_02_10_R20 showing total force on the indenter.

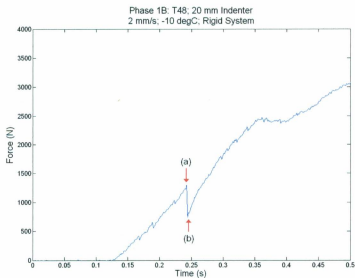


Figure 4.17: Enlarged view of the region boxed in red in Figure 4.16.

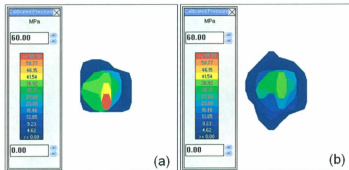


Figure 4.18: Pressure distribution images corresponding to the load drop identified in the force-time trace in Figure 4.17.

The thin-section for test T48_1B_02_10_R20 is presented in Figures 4.19. The top photograph highlights zones of microfracture near the edges of the layer while the bottom photograph reveals the layer to be heavily dominated by recrystallization.

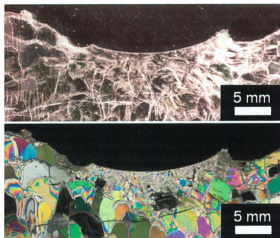


Figure 4.19: Thin-section of damaged zone from test T48_1B_02_10_R20 photographed with side lighting (Top) and through cross-polarized light (Bottom).

4.3.3 Medium Speed Test (4 mm/s)

The time series data from the MTS load cell for indentation test T51_1B_04_10_R20 is shown in Figure 4.20. This test was also conducted with the 20 mm diameter rigid indenter system but with an indentation rate of 4 mm/s. The force data from the MTS load cell shows little evidence of cyclic loading except for a few cycles near beginning of the test, from approximately 0.18 to 0.23 seconds. The maximum load achieved in the test was 14.6 kN. An enlarged view of the region boxed in red in Figure 4.20 is provided in Figure 4.21. Arrows (a) and (b), and (c) and (d) point to the peaks and troughs of two consecutive load cycles and the corresponding pressure distribution images are presented in Figure 4.22. The amplitude of the load drop from (a) to (b) is 0.4 kN and from (c) to (d) is 0.7 kN. Based on the pressure distribution images in Figure 4.22 it is apparent that these load drops are a result of high pressure zone failure, characterized by a decrease in the intensity of the high pressure zone without an appreciable shift in position. The thin-section for test T51_1B_04_10_R20 is presented in Figure 4.23. The top photograph highlights zones of microfracture near the edges of the layer while the bottom photograph shows the layer is heavily dominated by recrystallization.

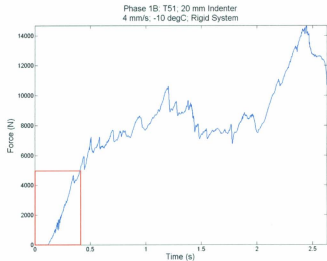


Figure 4.20: MTS load cell data for test T51_1B_04_10_R20 showing total force on the indenter.

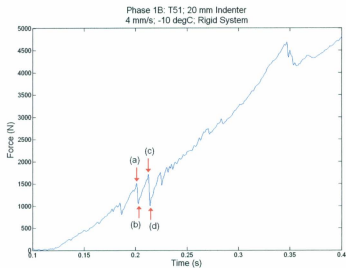


Figure 4.21: Enlarged view of the region boxed in red in Figure 4.20.

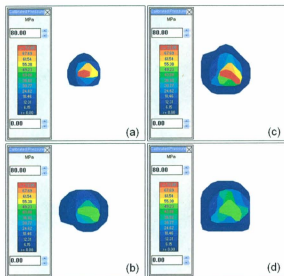


Figure 4.22: Pressure distribution images corresponding to the load drop identified in the force-time trace in Figure 4.21.

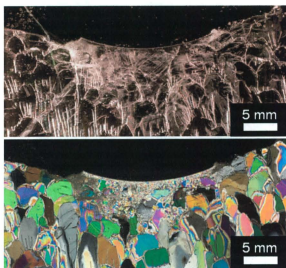


Figure 4.23: Thin-section of damaged zone from test T51_1B_04_10_R20 photographed with side lighting (Top) and through cross-polarized light (Bottom).

4.3.4 Fast Speed Test (6 mm/s)

The time series data from the MTS load cell for indentation test T52_1B_06_10_R20 is shown in Figure 4.24. This test was also conducted with the 20 mm diameter rigid indenter system but with the fastest indentation rate for Phase 1B, 6 mm/s. The force data from the MTS load cell shows little evidence of cyclic loading except for a few periods in the first 0.3 seconds of the test. The maximum load achieved in the test was 12.3 kN. An enlarged view of the region boxed in red in Figure 4.24 is provided in Figure 4.25. Two locations within the first period of cyclic loading, which had an amplitude of approximately 0.1 kN, are identified with arrows (a) and (b) and four locations in the second period of cyclic loading, which had amplitudes of approximately 0.3 kN, are identified with arrows (c) through (f). The arrows correspond to pressure distribution images in Figure 4.26. The pressure distribution images show that throughout both periods of cyclic loading there is no significant loss of contact area or appreciable shift in the position of the high pressure zones. As such, the failure mechanisms associated with the load drops are high pressure zone failures. The thin-section for test T52_1B_06_10_R20 is presented in Figure 4.27. The top photograph highlights zones of microfracture near the edges of the layer while the bottom photograph reveals the layer to be heavily dominated by recrystallization.

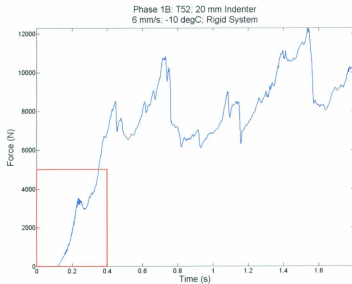


Figure 4.24: MTS load cell data for test T52_1B_06_10_R20 showing total force on the indenter.

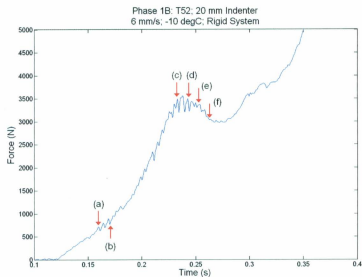


Figure 4.25: Enlarged view of the region boxed in red in Figure 4.20.

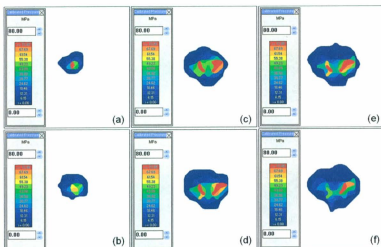


Figure 4.26: Pressure distribution images corresponding to the load drop identified in the force-time trace in Figure 4.21.

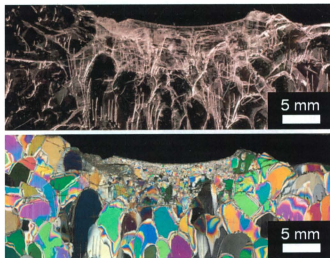


Figure 4.27: Thin-section of damaged zone from test T52_1B_06_10_R20 photographed with side lighting (Top) and through cross-polarized light (Bottom).

4.3.5 Results for Increased Indenter Size

The three sets of test results presented above are for a rigid, 20 mm diameter spherical indenter covering the three indentation rates tested in Phase 1B. The following is provided to show a sample of the results obtained while indenting with the larger, 40 mm diameter indenter.

The time series data from the MTS load cell for indentation test T54_1B_02_10_R40 is shown in Figure 4.28. This test was conducted with the larger 40 mm diameter rigid indenter system, at an indentation speed of 2 mm/s and a temperature of -10°C . The force data from the MTS load cell shows little evidence of cyclic loading except for a period between 0.2 and 0.5 seconds. The maximum load achieved in the test was 39.8 kN, which is significantly greater than the loads achieved with the 20 mm diameter indenter but was expected as the indenter is twice as large. An enlarged view of the region boxed in red in Figure 4.28 is provided in Figure 4.29. The peaks and troughs of three load drops are identified with arrows (a) through (f) and the corresponding pressure distribution images are presented in Figure 4.30. From the pressure distribution images it can be seen that the three load drops considered are a result of high pressure zone failures, characterized by moderate decreases in the intensity of the high pressure zones without any appreciable loss of contact area. The average amplitude of the load drops is approximately 0.4 kN with a frequency of approximately 50 Hz. The thin-section for test T54_1B_02_10_R40 is presented in Figures 4.31. From the bottom photograph it can be seen that the layer is significantly dominated by a

fine-grained recrystallized microstructure across its entire width, while the top photograph highlights a zone of microfracture near the left edge of the layer.

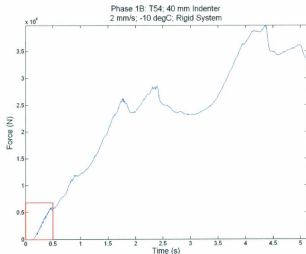


Figure 4.28: MTS load cell data for test T54_1B_02_10_R40 showing total force on the indenter.

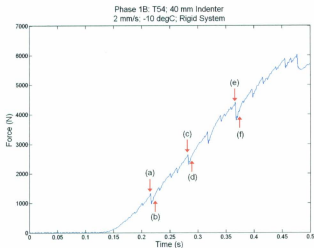


Figure 4.29: Enlarged view of the region boxed in red in Figure 4.28.

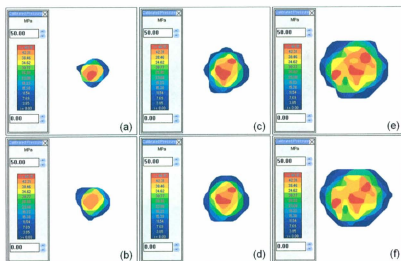


Figure 4.30: Pressure distribution images corresponding to the load drop identified in the force-time trace in Figure 4.29.

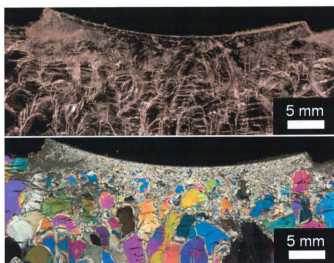


Figure 4.31: Thin-section of damaged zone from test T54_1B_04_10_R40 photographed with side lighting (Top) and through cross-polarized light (Bottom).

4.4 Summary

A total of 44 small-scale indentation tests were completed in Phases 1A and 1B and a sampling of the results were presented in this chapter. From the collected data it was observed that cyclic loading patterns can be achieved through the compressive failure of polycrystalline ice specimens. These periods of cyclic loading appear most often and most pronounced through indentation in the presence of structural feedback. During tests on warm ice there was little evidence of cyclic loading the ice experienced ductile failure.

Through analysis of tactile pressure data it was determined that a single, stationary high pressure zone was successfully simulated through indentation with a spherical, steel indenter. The tactile pressure data also allowed load drops to be linked to failure mechanisms such as high pressure zone failure and spalling fracture. Thin-sections of the damaged regions allowed for assessment of the microstructural modifications in the vicinity of the indentation zone. Most thin-sections had some amount of microfracture and recrystallization in the damaged layer although the warm ice results show the damaged layer to be mostly dominated by recrystallization.

Chapter 5: Analysis

5.1 Overview

Small-scale laboratory work has been used to aid in our understanding of the mechanics associated with observed ice failure processes during ice-structure interaction. Through the successful simulation of a single, stationary high pressure zone, and with the ability to record the total load, structural deflection, and interfacial pressure distribution, it is possible to gain insight into the role of: load limiting failure mechanisms, temperature, structural feedback, and loading rate during the compressive failure of ice.

Results from the analysis of the data collected during the two phases of small-scale compressive ice failure experiments are presented in this chapter. Tactile pressure distribution data and high-speed video recordings were synchronized with the load trace data to link observed failure mechanisms in the ice (i.e. crushing and spalling) with specific events in the load trace. A range of testing temperatures, levels of structural compliance, and loading rates were tested and

analyzed to study their effect on ice failure processes during ice-structure interaction.

5.2 Observations of Ice Failure Process

Each test has been reviewed individually to determine the behaviour of the ice in the vicinity of the high-pressure zone. Particular attention was placed on the failure mechanisms which acted to limit the total load during periods of cyclic loading. Synchronizing tactile pressure distribution data and high-speed video recordings with load trace data for each test allowed load drops and periods of cyclic loading to be associated with observed failure processes in the ice related to high pressure zones, such as crushing and spalling.

5.2.1 Crushing

In ice mechanics literature crushing refers to the pulverization and extrusion of softened ice from the periphery of high-pressure zones (Jordaan et al., 2008) and is associated with the failure of these high pressure zones. The crushing failure of ice acts as a load limiting failure mechanism during ice-structure interaction and through analysis of the experimental data it has been observed to produce regular, cyclic loading patterns. This observation supports the theory that it is the cycling of pressure softening and hardening in the damaged layer that produces the cyclic behaviour associated with crushing (Jordaan et al., 2008).

The cyclic loading patterns produced as a result of crushing failure of the ice had a wide range of amplitudes and frequencies. The frequency of load cycling was

often found to decrease throughout the duration of a test and this is due to the contact area increasing with increasing penetration of the spherical indenter tip. Other factors, such as structural compliance and loading rate, control the amplitude and frequency and will be discussed later in this chapter.

When analyzing tactile pressure distribution data a crushing event is characterized by a decrease in the intensity of a high pressure zone without an appreciable shift in position or loss of contact area, as described in Chapter 3, Section 3.1.1.

Through visual observation of the ice surface, (i.e. high-speed video footage) a crushing event is characterized by the extrusion of fine-grained pulverized material from around the indenter. During periods of cyclic loading high-speed video footage will show the continuous extrusion of material which appears to flow from under the indenter. A period of cyclic loading is shown in Figure 5.1 with three consecutive cycles identified. Each load drop, (a) to (b), (c) to (d), and (e) to (f), can be associated with crushing events, or failure of the high pressure zone. Tactile pressure distribution images for each set of points are presented in Figure 5.2 showing the characteristic high pressure zone failure.

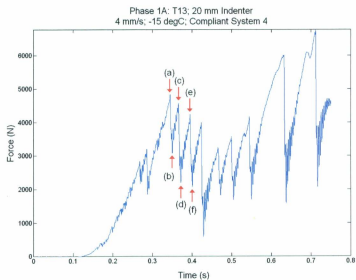


Figure 5.1: Miniature load cell data identifying cyclic crushing failure.

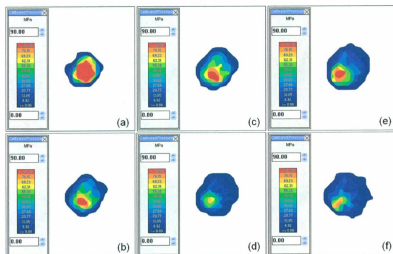


Figure 5.2: Pressure distribution images before and after crushing events.

5.2.2 Spalling

A second load limiting failure mechanism associated with the compressive failure of ice related to high pressure zones is spalling fracture. Unlike crushing failure, which occurs in a consistent and regular nature, spalls have been observed to occur intermittently and are likely promoted by the presence of flaws in the ice. Each individual load drop in each test was analyzed to determine if spalling was the associated failure mechanism. Spalling failures are characterized by a significant loss of contact area at the ice-indenter interface and throughout these experiments have been observed to interrupt the cyclic loading patterns produced from crushing failure. This interruption is likely due to the significant loss of contact area at the ice-indenter interface and the associated time it takes to regain the level of contact necessary to form a high pressure zone. Figure 5.3 presents the same load record shown in Figure 5.1 but identifies a spalling event that interrupts the cyclic loading trend discussed above. Two pressure distribution images from before and after the spall, Figure 5.4 (a) and (b), show the loss of contact area associated with the event. A still image from the high-speed video footage, Figure 5.4 (c), identifies two large fragments of ice projected from the surface as a result of the spalling event.

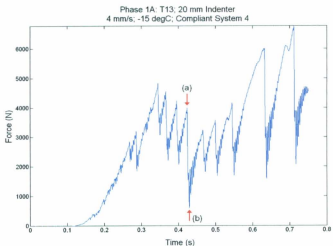


Figure 5.3: Miniature load cell data identifying a spalling event.

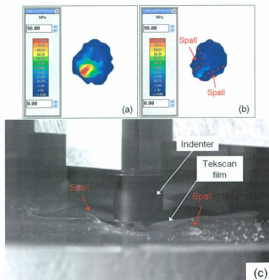


Figure 5.4: Pressure distribution before (a) and after (b) a spalling event, and a still taken from the high-speed video recording of the event.

5.3 Effect of Temperature

Temperature had a significant effect on the failure processes and resulting load patterns produced during these experiments. For all tests conducted at -5°C there was no evidence of crushing or load cycling and the ice appeared to fail in a ductile mode. It should be noted that in this context ductile failure is more akin to a damaged enhanced creep response. It should be noted that spalling events still occurred in tests at -5°C , but were rare. Figure 5.5 presents two force plots, one at -5°C and the other at -15°C , for Compliant System 4 at an indentation rate of 7 mm/s. It can be seen that the cold ice test produced regular cyclic loading patterns while the warm ice test experienced ductile failure. The crushing failure in the cold test appears to limit the maximum achievable load, while the ductile failure in the warm test is characterized by a steady, increasing load.

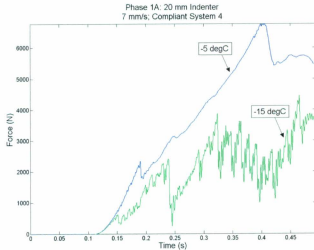


Figure 5.5: Miniature load cell data for two identical tests at different temperatures.

Temperature was also observed to have an effect on the microstructural modification of the damaged layer. In Phase 1A, when thin-sections taken from tests with the same indentation rate and same indentation system but different test temperatures were compared it was found that the warmer ice (-5°C) results were more heavily dominated by recrystallization. The cold ice results (-15°C) were significantly dominated by zones of microfracture. A similar observation was found by Barrette et al. (2002). Li et al. (2004) similarly observed damaged layers mainly comprised of recrystallization for very slow indentation rates, even though the temperature was as low as -10°C . This leads one to believe that the microstructural modifications in the damaged layer will be dominated by recrystallization if the ice experiences ductile failure. Figure 5.6 (a) and (b) show the thin-section photographs, taken through cross-polarized light and side-light, respectively, for Compliant System 4 indenting at a rate of 4 mm/s and at a temperature of -5°C . The damaged layer is recrystallized across its entire width with only small areas of microfracture at the edges. When compared to the thin-section photographs in Figure 5.6 (c) and (d), for the same indentation system at the same indentation rate, but at a temperature of -15°C , it can be seen that the damaged layer is more heavily dominated by microfracture, and only a small zone in the center is recrystallized.

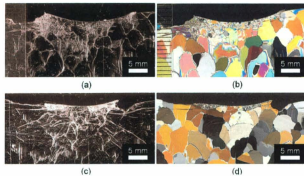


Figure 5.6: Thin-section photographs highlighting the effect of temperature on microstructural modification in the damaged layer.

5.4 Effect of Structural Compliance

Throughout the course of this experimental program six different indentation systems were used: four compliant systems (Phase 1A), and two rigid systems (Phase 1B). Three main observations have been linked to structural feedback, or the lack thereof. First, due to the elastic deflection of the compliant systems the actual indentation rate experienced by the ice, referred to as the relative indentation rate, is lower than the nominal rate imposed by the MTS actuator during periods of load increase. When the ice fails the structure springs forward greatly increasing the relative rate. Second, the amplitudes produced during periods of cyclic loading for tests with compliant systems have significantly larger amplitudes than tests with rigid systems. Lastly, it has been identified through these experiments that the frequency of load cycling has a strong dependence on the compliance of the system.

5.4.1 Relative Indentation Rate

The indentation structures used in Phase 1A deflected under load due to their compliance. When the advancing ice specimen (controlled by the MTS actuator) makes first contact with the structure the structure deflects elastically resulting in a decreased relative loading rate. The structure continues to deflect until the strength of the ice is exceeded by the structural resistance and the ice fails. Upon failure of the ice and subsequent loss of load capacity the structure will spring back resulting in an increased relative loading rate. It is known that the strength of ice has a strong dependence on the rate of loading (Peyton, 1968). The decreased loading rate during the loading stage creates an increase in ice strength and subsequently allowing the total force to grow. Upon failure of the ice and subsequent spring-back of the structure the ice experiences increased loading rates leading to a decrease in strength of the ice. For periods of cyclic loading the relative loading rate was observed to cycle between decreased rates, during the loading stage, and increased rates, during the spring-back stage. Figure 5.7 is a displacement plot for test T23_1A_07_15_C1 showing the nominal loading rate imposed by the MTS, the structural deflection at the mid-length of the compliant beam measured by the middle LVDT, and the resulting relative indentation rate (taken as the nominal rate minus the structural deflection). It can be seen that during the loading stages the relative rate is reduced to approximately 2 mm/s from the nominal rate of 7 mm/s. During a spring-back stage the relative loading rate increases to 195 mm/s, almost 200 times the rate during the loading stage.

The average relative loading rates during loading stages for all indentation systems from Phase 1A are presented in Table 5.1, and plotted against the nominal rates in Figure 5.8. As would be expected, the relative rates decrease with increasing compliance, because the greater the compliance the further the structure will deflect under a given load. The relative rates also decrease with decreasing temperature, meaning that a given structure will deflect further at -15°C than at -5°C .

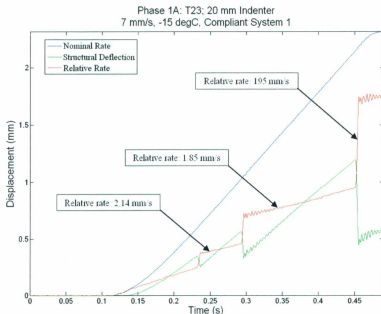


Figure 5.7: Plot of the relative indentation rate for test T23_1A_07_15_C1.

Table 5.1: Relative indentation rates due to structural compliance

Nominal Rate	Compliant System 1 Relative Rate		Compliant System 2 Relative Rate		Compliant System 3 Relative Rate		Compliant System 4 Relative Rate	
	-5°C	-15°C	-5°C	-15°C	-5°C	-15°C	-5°C	-15°C
4	1.5	1.2	2.7	2.1	3.7	3.1	3.8	3.4
7	2.7	2.0	5.8	3.1	6.1	5.2	6.8	7.2
10	3.1	3.3	8.1	6.0	9.4	7.4	9.5	9.5

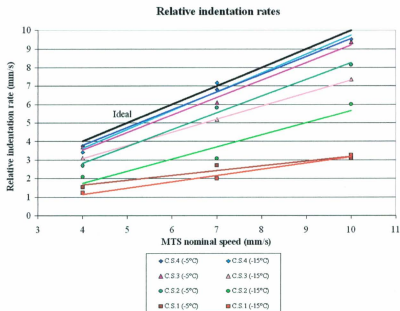


Figure 5.8: Relative indentation rates versus nominal indentation rates for Phase 1A indentation systems.

5.4.2 Amplitude and Frequency of Cyclic Loading

For test conditions that produced cyclic loading patterns the amplitude was affected by the presence of structural feedback. Ten tests that produced regular cyclic loading patterns are presented in Table 5.2. Five different structural systems are considered: Compliant Systems 2, 3, and 4, and the 20 mm and 40 mm diameter Rigid Systems. All tests considered were conducted at 4 mm/s. It

can be seen that in the presence of structural feedback (i.e. indentation systems that are not perfectly rigid) the average amplitudes during periods of cyclic loading range from 2410 N to 2657 N, while for tests conducted with rigid systems the amplitudes range from 148 N to 800 N. This dramatic difference in amplitudes is likely due to the structural deflection of the compliant systems creating decreased relative loading rates which subsequently increase the strength of the ice allowing for the development of greater total loads prior to failure. Increased relative loading rates produced upon failure of the ice and associated spring-back cause a decrease in the ice strength and therefore an increased drop in load. The amplitudes for T50 and T51 are larger than those for T25, T26 and T27. A possible explanation may be that the increased confinement from the smaller rings affects the fracture behaviour, though this would not likely affect damage processes.

Table 5.2: Average amplitude for periods of cyclic loading for five different indentation systems.

Test	Indentation Rate (mm/s)	Stiffness (MN/m)	Indenter (mm)	Confining Ring Diameter (mm)	Average Amplitude (N)
T13	4	150	20	300	2657
T16	4	15	20	300	2580
T19	4	10	20	300	2410
T25	4	Rigid	20	300	184
T26	4	Rigid	20	300	148
T27	4	Rigid	20	300	199
T50	4	Rigid	20	150	260
T51	4	Rigid	20	150	680
T56	4	Rigid	20	150	800
T60	4	Rigid	20	300	800

The frequency of cyclic loading was identified to have a linear relationship with the stiffness of the structure. Figure 5.9 presents a plot of frequency versus

structural stiffness for the three indentation rates tested in Phase 1A. The stiffnesses correspond to Compliant Systems 1, 2, and 3. Compliant System 4 was an outlier in this particular analysis and was not included. This is likely due to the inelastic behaviour of Compliant System 4. It can be seen that at 4, 7, and 10 mm/s the frequency of cyclic loading has a linear, positive trend with increasing structural stiffness.

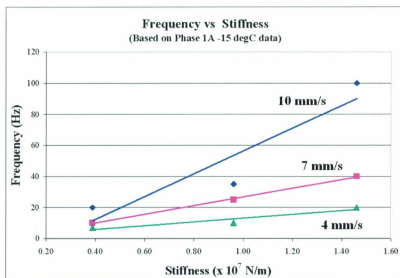


Figure 5.9: Plot of frequency versus stiffness for Phase 1A data.

5.5 Link between Speed and Frequency

For both the compliant system tests in Phase 1A and the rigid system tests in Phase 1B there is a linear relationship identified between the frequency during periods of cyclic loading and the nominal indentation rate. Figure 5.10 presents the linear trends for Compliant Systems 1, 2, and 3. Similar to Figure 5.9 above,

data for Compliant System 4 is not plotted due to the inelastic behaviour of the system.

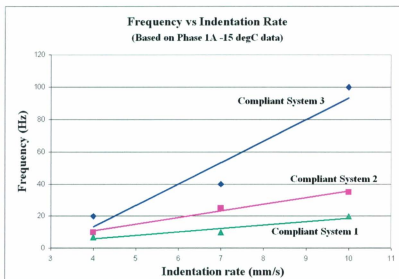


Figure 5.10: Plot of frequency versus indentation rate for Phase 1A data.

In the absence of structural feedback a linear relationship was still identified between the cycling frequency and the rate of indentation. Figure 5.11 presents a plot of the linear trends for Phase 1B data. It can be seen that increasing the rate from just 2 to 6 mm/s causes an increase in frequency of approximately 150 Hz.

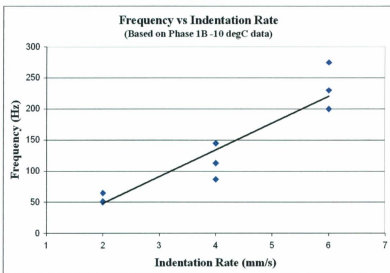


Figure 5.11: Plot of frequency versus indentation rate for Phase 1B data.

5.6 Preliminary Spectral Analysis

A preliminary spectral analysis was performed on the load-time trace for test T14_1A_07_15_C4 to determine if a Fast Fourier Transform (FFT) can be used to determine the frequency of load cycling during crushing. FFT is commonly used to find the frequency components of a signal that is buried in noise. There are several factors contributing to the difficulty of isolating the cyclic loading frequency for these experiments. Firstly, noise inherent to the instrumentation, due to the sensitivity of the instrument, will cause false spikes in the spectral plots. Secondly, transient vibrations in the indentation system can be quite significant, especially for a more compliant system, and can mask the actual load cycling frequency produced by crushing. Lastly, due to the spherical geometry of

the indenter the contact area increases with penetration, which in turn causes the load cycling frequency to gradually decrease as a test proceeds.

To eliminate some of the noise in the load signal the data was first filtered to eliminate any frequencies above 500 Hz. This value was chosen because damage processes in ice, as observed from previous small-scale indentation tests, have been observed to occur at frequencies below 500 Hz. Using MATLAB a FFT was implemented on the filtered data. Figure 5.12 presents the spectral plot for test T14_1A_07_15_C3. A manual count of the frequency for this test gives an approximate value of 70 Hz. As can be seen from Figure 5.12 there is a noticeable spike at 73 Hz. This is a promising result but without prior knowledge of the cycling frequency it would be difficult to say with confidence that that 73 Hz spike on the spectral plot is in fact the load cycling frequency.

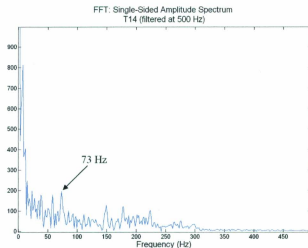


Figure 5.12: FFT spectral plot for test T14_1A_07_15_C3.

5.7 Summary

Small-scale laboratory indentation tests were conducted to aid in our understanding of the mechanics associated with ice failure processes related to high pressure zones. It was found that regular periods of cyclic loading were a result of crushing failure of the ice, and that this crushing failure is directly related to the failure of high pressure zones, as was observed through pressure distribution data and high-speed video footage. A second load limiting failure mechanism observed was spalling. Spalling occurred intermittently and most often acted to disrupt cyclic loading patterns.

Tests on warm ice (-5°C) produced no cyclic loading patterns and the ice experienced ductile failure. Cyclic loading patterns developed at -10°C and -15°C . Temperature also had an effect on the microstructural modification in the damaged layer. In warmer ice tests the damaged layer was almost entirely composed of a fine-grained, recrystallized microstructure. For the colder tests, zones of microfracture were apparent in the layer, and on occasion the entire layer would be microfractured.

When structural compliance was introduced into the system the deflection of the structure under load would create a decreased relative loading rate. This decreased loading rate lead to an increase in ice strength and resulted in larger amplitude load cycling, when compared to rigid indentation tests. The frequency of load cycling was also found to have a linear dependence on the structural stiffness on the indentation systems. For both compliant and rigid system indentation tests

there was a linear relationship identified between load cycling frequency and rate of indentation. Further data points are necessary to confirm this linear relationship for the compliant indentation systems.

Chapter 6: Discussions and Conclusions

6.1 Main Conclusions

The objective of this research program was to improve our understanding of compressive ice failure mechanics during ice-structure interaction. Emphasis was placed on investigating the processes responsible for the formation and evolution of high pressure zones, the processes that serve to limit ice loads, the influence of temperature on load-limiting ice failure mechanisms, the role of structural feedback, and the effect of indentation rate on the ice-structure interaction process. Based on the analysis of the data collected from the forty-four ice indentation tests four main conclusions have been drawn.

6.1.1 Crushing and Cyclic Loading

For testing conditions which produced regular cyclic loading patterns the associated ice failure mechanism was crushing and this was determined through analysis of the pressure distribution data. During periods of crushing regular drops

in load were linked to failure of the high pressure zone, resulting in a decrease in the contact pressure and an extrusion of pulverized ice from the periphery of the contact area. A second load-limiting failure mechanism observed was spalling fracture. This could not be linked to regular, cyclic loading patterns, but rather it was observed to occur intermittently and often interrupted cyclic loading patterns produced from crushing failure.

6.1.2 Effect of Temperature

The temperature of ice during compressive loading has a drastic effect on the process by which it fails. When warmer ice, near -5°C , is loaded in compression ductile failure dominates resulting in a steady increase in load without any cyclic pattern development. For colder ice, the failure mechanisms become dominated by crushing and spalling and crushing will often lead to the development of regular cyclic loading patterns.

The microstructure of the ice in the damaged layer has a dependence on the temperature of the ice at the time of indentation. For warmer ice the damaged layer is heavily dominated by a fine-grained, recrystallized microstructure, where as for colder tests only the central portion of the layer is recrystallized while the outer edges are highly microfractured. As the ice temperature at the time of indentation is decreased microfracture becomes the dominant microstructural modification within the layer.

6.1.3 Effect of Structural Compliance

The compliance of the indentation structure has two main effects. First, due to its deflection under load, it decreases the relative indentation rate experienced by the ice and subsequently increases the ice strength which allows the total load to grow. Upon failure of the ice the elastic energy stored in the structure through deflection is released through spring-back of the structure. This cycling between decreased and increased relative indentation rates aids in the development of cyclic loading patterns.

The second effect is that the frequency of cyclic loading has a linear dependence on the compliance, or stiffness, of the structure. Stiffer structures will produce cyclic loading patterns with higher frequencies. The amplitude of load drops is also dependent on the presence of structural feedback. For rigid indentation tests it was observed that the load drops were much less than those observed for compliant indentation tests. These smaller load drops are likely related to the lack of structural deflection experienced by the rigid structure causing a decrease in the feedback of energy from the structure into the ice.

6.1.4 Linear Relationship between Speed and Frequency

A linear relationship is observable between the speed at which the structure indents the ice and the frequency of the resulting cyclic loading patterns. The faster the indentation speed the greater the frequency. This relationship was observed for both rigid and compliant systems however the frequencies achieved with the rigid systems were much larger than those achieved with the compliant

systems. Also the increase in frequency for a unit increase in indentation speed is much larger for a rigid system than a compliant system.

6.2 Recommendations for Future Work

Throughout the course of this experimental program several recommendations for future work emerged. The most obvious, and most ambitious, recommendation is to study compressive ice failure at full-scale. The rationale for small-scale testing was that high pressure zones can be successfully modeled at small scale and the characteristics of these high pressure zones and the structure of the damaged layer remains similar at different scales. This justifies relatively inexpensive laboratory testing to studying compressive ice failure, but ultimately a collection of full-scale data would be invaluable to the research team.

Within the scope of small-scale laboratory testing a number of recommendations can be made. First, increasing the size of the indenter would provide data which could be used to assess scale effects in relation to compressive ice failure and provide insight for the prediction of full-scale interactions. Second, when an ice floe crushes against a vertical structure it is known that many high pressure zones form and transmit load to the structure. The failure of one high pressure zone can trigger the failure of other high pressure zones and may lead to synchronized crushing failure. Simulating multiple high pressure zones on the same compliant structure through use of multiple indenters would allow for the investigation of synchronized crushing and other multiple high pressure zone processes. Third,

exploring temperature effects more fully would be of great value. It was seen that for warmer temperatures and moderate loading rates (up to 10 mm/s) ice failed in a ductile mode. Investigating if increased indentation rates on warm ice would produce brittle failure would be a positive direction for small-scale research. As well, analyzing full-scale data, from projects such as Structures in Ice (STRICE), to study temperature effects at large-scale would be of great benefit.

The following recommendations for future work have already been implemented in Phase 1C of the research program "Compressive Ice Failure Mechanics" which is beyond the scope of this thesis. First, it was recommended that simpler indentation systems be designed to allow for more accurate prediction and modeling of structural response. These have been designed and tested and have successfully eliminated any non-elastic behaviour in the structure. Second, a stiffer structure was recommended in order to further investigate the linear dependence of cyclic loading on structural stiffness. The newly designed structure with increased stiffness produced promising results achieving frequencies greater than those observed in Phase 1A and 1B.

In conclusion, the results of this experimental program appear promising and are currently being used to determine the optimal conditions for studying compressive ice failure mechanics in the laboratory. These results will be used to guide the development of the remainder of this industry sponsored research program, and ultimately provide insights to improve the design of offshore structures for ice environments.

Bibliography

Akagawa, S., Nakazawa, N., Sakai, M., Matsushita, H., Terashima, T., Takeuchi, T., and Saeki, H. 2000. Ice failure mode predominantly producing peak-ice-load observed in continuous ice load records. Proceedings of the 10th International Offshore and Polar Engineering Conference. 2000. p. 613.

Barrette, P., Pond, J., and Jordaan, I.J., 2002. Ice damage and layer formation: in small scale indentation experiments. *Ice in the Environment, Proceedings of the 16th international Symposium on Ice, IAHR, Dunedin, New Zealand, 2002, Vol. 3:246-253*

Blenkarn, K.A., 1970. Measurement and analysis of ice forces on Cook Inlet Structures. Proc. 2nd OTC Conf., Houston, TX, OTC 1261, Vol. 2, pp. 365-378.

Duval P., Ashby, M.F., and Anderman, I., 1983. Rate-controlling processes in the creep of polycrystalline ice. *J Phys. Chem.* 87: pp. 4066-4074.

Frederking, R.M.W., Jordaan, I.J., and McCallum, J.S., 1990. Field tests of ice indentation at medium scale: Hobson's Choice ice island 1989. Proceedings of 10th International Symposium on Ice, IAHR, Espoo, Finland, Vol. 2, pp. 931-944.

Frederking, R.M.W., 2004. Ice pressure variations during indentation. Proceedings of the 17th IAHR International Symposium on Ice. 2004. Vol. 2. pp. 307.

- Gagnon, R.E. 1994. Generation of Melt During Crushing Experiments on Freshwater Ice. *Cold Regions Science and Technology*, Vol. 22, No. 4, pp. 385-398.
- Jeffries, M., Kärnä, T. and Løset, S. 2008. Field data on the magnification of ice loads on vertical structures. *Proceedings of the 19th IAHR International Symposium on Ice*, Vancouver, BC, Vol. 2, pp. 1115–1134.
- Jordaan, I. and McKenna, R., 1988. Constitutive relations for creep of ice. *Proceedings of 9th IAHR International Symposium on Ice*, Vol. 3, Sapporo, Japan, pp. 47–58.
- Jordaan, I.J. and Xiao, J., 1992. Interplay between damage and fracture in ice-structure interaction. *Proceedings of the 11th International Symposium on Ice, IAHR, Banff, Alberta*, 1992, Vol. 3, pp. 1448 – 1467.
- Jordaan, I.J. and Singh, S.K. 1994. Compressive ice failure: critical zones of high pressure. *Proc. 12th Int. IAHR Ice Symp.*, Vol. 1, Trondheim, Norway, pp. 505-514.
- Jordaan, I., Matskevitch, D., and Meglis, I., 1997. Disintegration of ice under fast compressive loading. *Proceedings of the Symposium on Inelasticity and Damage in Solid subject to Microstructural Change*, St. John's, Newfoundland, pp. 211–231.
- Jordaan, I.J., 2001. Mechanics of ice-structure interaction. *Engineering Fracture Mechanics*; 68, pp. 1923-1960
- Jordaan, I.J., Li., C, Barrette, P., Duval, P. and Meyssonier, J. 2005. Mechanisms of ice softening under high pressure and shear. *Proc., 18th Int. POAC*. Vol. 1, pp. 249-260.
- Jordaan, I.J., Wells, J., Xiao, J., Derradji-Aouat, A., 2008. Ice crushing and cyclic loading in compression. *Proceedings 19th IAHR Symposium on Ice*, Vancouver, British Columbia, Canada.
- Jordaan, I.J. and Taylor, R.S. 2011. Viscoelasticity, damage and ice behaviour in compression. *Proc., 21st Int. POAC*, Montreal, Canada, pp.78 – 87.

- Jordaan, I.J., Taylor, R.S., and Derradji-Aouat, A. 2012. (Draft) Scaling of flexural and compressive ice failure. Proc. 31st OMAE Conf. Rio de Janeiro.
- Kachanov, L., 1958. On the creep rupture time. *Izv. An SSSR, Otd. Tekhn. Nauk*, pp. 26–31.
- Kärnä, T. and Turunen, R., 1990. A straightforward technique for analyzing structural response to dynamic ice action. Proc. 9th OMAE Conf. Houston. Vol. 4, pp. 135 - 142.
- Kärnä, T., 1994. Steady-state vibrations of offshore structures. *Hydrotechnical Construction* 28(8), pp. 446-454.
- Kärnä, T., Guo, F., Løset, S. and Määttänen, M. 2008. Small-scale data on magnification of ice loads on vertical structures. Proceedings of the 19th IAHR International Symposium on Ice, Vancouver, BC.
- Li, C., 2002. Finite element analysis of ice-structure interaction with a viscoelastic model coupled with damage mechanics. M.Eng Thesis, Memorial University, St. John's, NL, Canada.
- Maattanen, M., 1977. Stability of self-excited ice-induced structural vibrations Proc., 4th Int. POAC, St. John's, Canada, pp. 684–694.
- Määttänen, M., 1978. On conditions for the rise of self-excited ice-induced autonomous oscillations in slender marine pile structures. *Winter Nav. Board, Finland, Res. Rep.*, 25.
- Mackey, T., Wells, J., Jordaan, I.J., Derradji-Aouat, A., 2007. Experiments on the fracture of polycrystalline ice. Proceedings of POAC 2007. Dalian, China.
- Masterson, D.M., Frederking, R.M.W., Jordaan I.J., Spencer, P.A., 1993. Description of multiyear ice indentation tests at Hobson's Choice ice island – 1990. Proceedings of 12th International Conference on Offshore and Arctic Engineering. Vol. 4. Glasgow. pp. 145-55.

- Peyton, H.R. 1968. Sea ice forces. Ice pressures against structures. Technical Memorandum, 92. National Research Council of Canada, Ottawa, Canada, pp. 117-123.
- Riska, K., Rantala, H. and Joensuu, A. 1990. Full scale observations of ship-ice contact. Laboratory of Naval Architecture and Marine Engineering, Helsinki University of Technology, Report M-97.
- Rice, J.R., 1968. Mathematical analysis in the mechanics of fracture. Liebowitz, H. (Ed.), Fracture, Vol. 2. Academic Press, New York, pp. 191-311.
- Sanderson, T.J.O., 1988. Ice mechanics: risks to offshore structures. Graham & Trotman, London.
- Schapery, R.A., 1981. On viscoelastic deformation and failure behaviour of composite materials with distributed flaws. Advances in Aerospace Structures and Materials, The American Society of Mechanical Engineers, pp.5-20.
- Schulson, E.M., 1999. The structure and mechanical behavior of ice. JOM, Vol. 51, No. 2. pp. 21-27.
- Ting, S.K. and Sunder, S.S., 1985. Constitutive modeling of sea ice with applications to indentation problems. CSEOE Research Report No. 3, MIT, Cambridge, Massachusetts.
- Singh, S., 1993. Mechanical behaviour of viscoelastic material with changing microstructure. Ph.D Thesis, Memorial University, St. John's, NL, Canada.
- Sinha, N.K., 1977. Technique for studying the structure of sea ice. Journal of Glaciology 18. pp. 315-323.
- Sinha, N.K., 1982. Delayed elastic strain criterion for first cracks in ice. Proc. of the symposium on deformation and failure of granular materials, Rotterdam: Balkema. pp. 323-330.

Sinha, N.K. and Cai, B., 1992. Analysis of Ice from Medium-Scale Indentation Tests. NRC Laboratory Memorandum IME-CRE-LM-002, 63p.

Sodhi, D.S., and Nakazawa, N. 1990. Frequency of intermittent ice crushing during indentation tests. Proceedings of 10th IAHR International Symposium on Ice, Espoo, Finland, Vol. 3, pp. 277-289.

Sodhi, D.S., Takeuchi, T., Nakazawa, N., Akagawa, S., Saeki, H., 1998. Medium-scale indentation tests on sea ice at various speeds. Cold Regions Science and Technology. 28. pp. 161-182.

Takeuchi, T., Masaki, T., Akagawa, S., Kawamura, M., Nakazawa, N., Terashima T., Honda, H., Saeki, H., and Hirayama, K. 1997. Medium-scale indentation tests (MSFIT) - ice failure characteristics in Ice/Structure interactions. Proceedings of 7th International Offshore and Polar Engineering Conference. Vol. 2. p. 376.

Taylor, R.S., Frederking, R.F. and Jordaan, I.J. 2008. The nature of high pressure zones in compressive ice failure. Proceedings of the 19th IAHR International Symposium on Ice, Vancouver, BC.

Taylor, R.S., 2010. Analysis of Scale Effect in Compressive Ice Failure and Implications for Design. Ph.D Thesis, Memorial University, St. John's, NL, Canada.

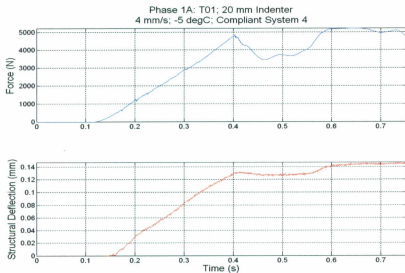
Wells, J., Jordaan, I., Derradji-Aouat, A. and Taylor, R. 2010. Small-scale laboratory experiments on the indentation failure of polycrystalline ice in compression: Main results and pressure distribution. Cold Regions Science and Technology, Vol. 65, No. 3, pp. 314-325.

Xiao, J., and Jordaan, I.J., 1996. Application of damage mechanics to ice failure in compression. Cold Regions Science and Technology. Vol. 24, pp. 305-322.

Xiao, J., 1997. Damage and fracture of brittle viscoelastic solids with application to ice load models. Ph. D Thesis, Memorial University, St. John's, NL, Canada.

**APPENDIX A – Test Results:
Total Load, Structural Deflection,
and Thin-section Photographs**

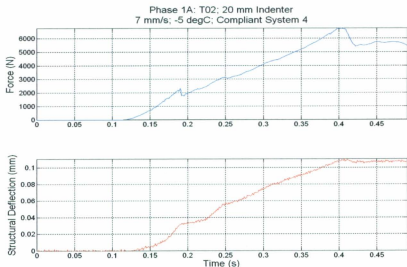
Phase 1A



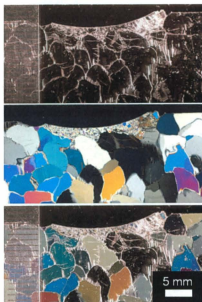
T01_1A_04_05_C4: Interaction load trace (Top); Structural deflection (Bottom).



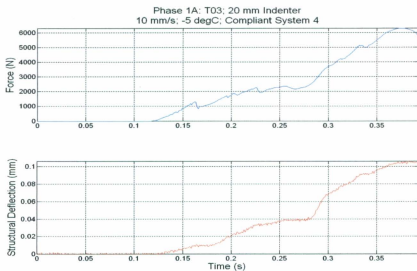
T01_1A_04_05_C4: Thin-section photographs: Sidelight (Top), X-polarized (Middle), and Combination (Bottom)



T02_1A_07_05_C4: Interaction load trace (Top); Structural deflection (Bottom).



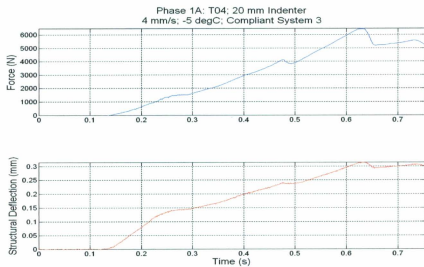
T02_1A_07_05_C4: Thin-section photographs: Sidelight (Top), X-polarized (Middle), and Combination (Bottom)



T03_1A_10_05_C4: Interaction load trace (Top); Structural deflection (Bottom).



T03_1A_10_05_C4: Thin-section photographs: Sidelight (Top), X-polarized (Middle), and Combination (Bottom)

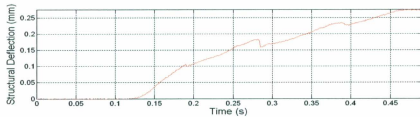
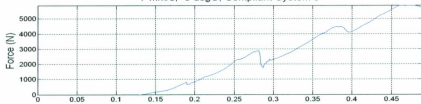


T04_1A_04_05_C3: Interaction load trace (Top); Structural deflection (Bottom).

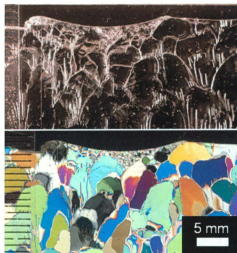


T04_1A_04_05_C3: Thin-section photographs: Sidelight (Top), X-polarized (Middle), and Combination (Bottom)

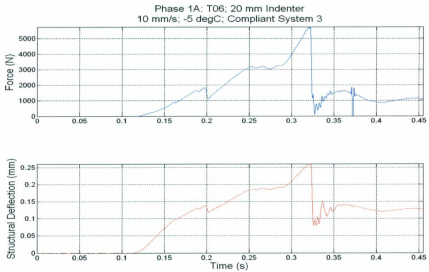
Phase 1A: T05; 20 mm Indenter
7 mm/s; -5 degC; Compliant System 3



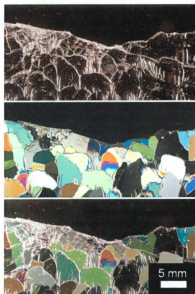
T05_1A_07_05_C3: Interaction load trace (Top); Structural deflection (Bottom).



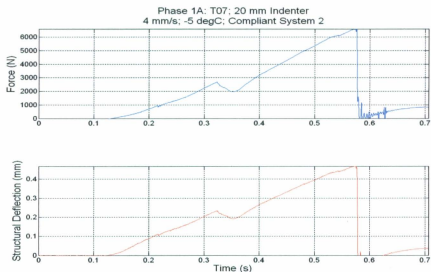
T05_1A_07_05_C3: Thin-section photographs: Silight (Top), and X-polarized (Bottom)



T06_1A_10_05_C3: Interaction load trace (Top); Structural deflection (Bottom).



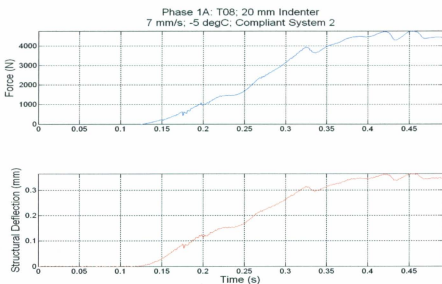
T06_1A_10_05_C3: Thin-section photographs: Silight (Top), X-polarized (Middle), and Combination (Bottom)



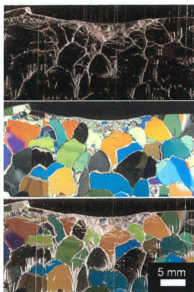
T07_1A_04_05_C2: Interaction load trace (Top); Structural deflection (Bottom).



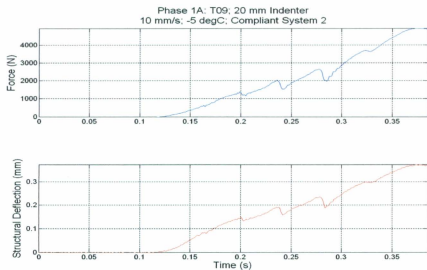
T07_1A_04_05_C2: Thin-section photographs: Sidelight (Top), X-polarized (Middle), and Combination (Bottom)



T08_1A_07_05_C2: Interaction load trace (Top); Structural deflection (Bottom).



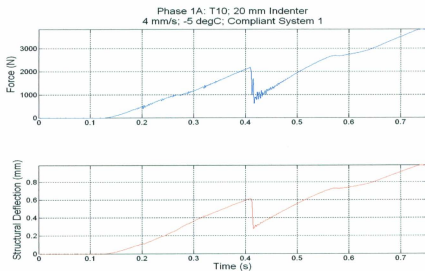
T08_1A_07_05_C2: Thin-section photographs: Sidelight (Top), X-polarized (Middle), and Combination (Bottom)



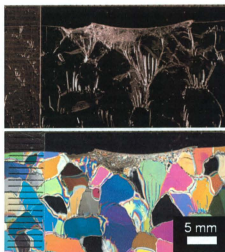
T09_1A_10_05_C2: Interaction load trace (Top); Structural deflection (Bottom).



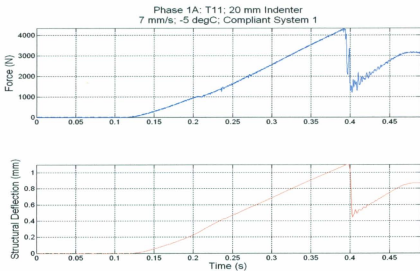
T09_1A_10_05_C2: Thin-section photographs: Sidelight (Top), X-polarized (Middle), and Combination (Bottom)



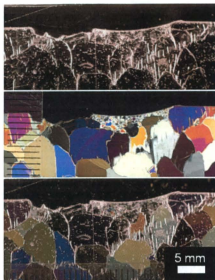
T10_1A_04_05_C1: Interaction load trace (Top); Structural deflection (Bottom).



T10_1A_04_05_C1: Thin-section photographs: Silight (Top),
and X-polarized (Bottom).

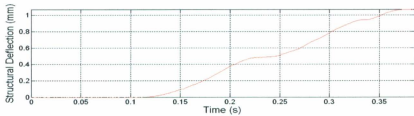
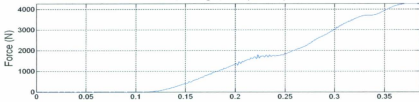


T11_1A_07_05_C1: Interaction load trace (Top); Structural deflection (Bottom).



T11_1A_07_05_C1: Thin-section photographs: Sidelight (Top), X-polarized (Middle), and Combination (Bottom)

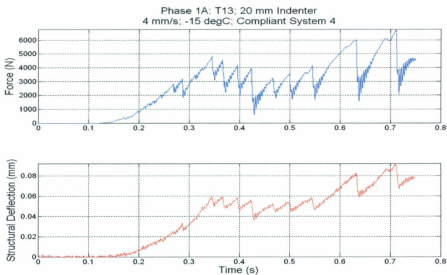
Phase 1A: T12: 20 mm Indenter
10 mm/s; -5 degC; Compliant System 1



T12_1A_10_05_C1: Interaction load trace (Top); Structural deflection (Bottom).



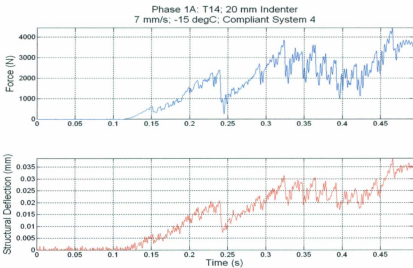
T12_1A_10_05_C1: Thin-section photographs: Sidelight (Top), X-polarized (Middle), and Combination (Bottom)



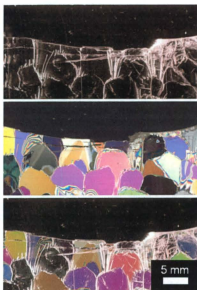
T13_1A_04_15_C4: Interaction load trace (Top); Structural deflection (Bottom).



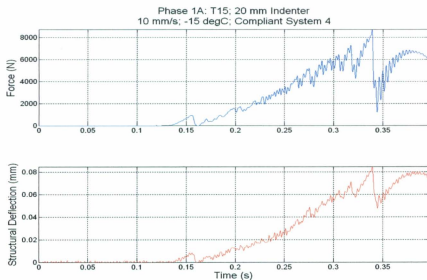
T13_1A_04_15_C4: Thin-section photographs: Silight (Top), X-polarized (Middle), and Combination (Bottom)



T14_1A_07_15_C4: Interaction load trace (Top); Structural deflection (Bottom).



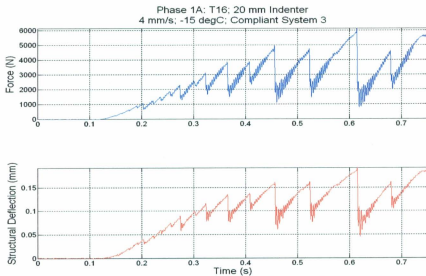
T14_1A_07_15_C4: Thin-section photographs: Silight (Top), X-polarized (Middle), and Combination (Bottom)



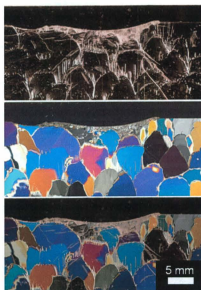
T15_1A_10_15_C4: Interaction load trace (Top); Structural deflection (Bottom).



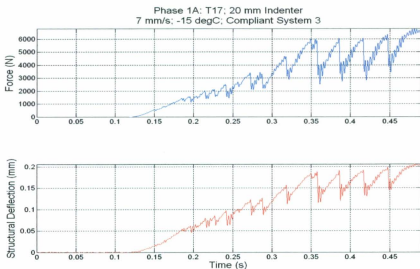
T15_1A_10_15_C4: Thin-section photographs: Silight (Top), X-polarized (Middle), and Combination (Bottom)



T16_1A_04_15_C3: Interaction load trace (Top); Structural deflection (Bottom).



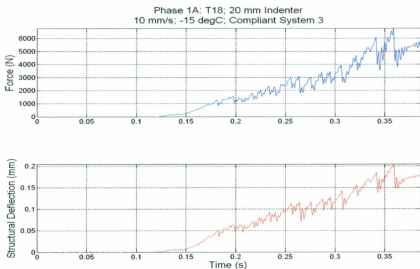
T16_1A_04_15_C3: Thin-section photographs: Silight (Top), X-polarized (Middle), and Combination (Bottom)



T17_1A_07_15_C3: Interaction load trace (Top); Structural deflection (Bottom).



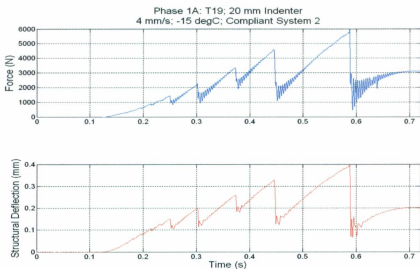
T17_1A_07_15_C3: Thin-section photographs: Sidelight (Top), X-polarized (Middle), and Combination (Bottom)



T18_1A_10_15_C3: Interaction load trace (Top); Structural deflection (Bottom).



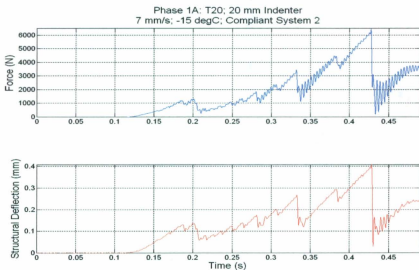
T18_1A_10_15_C3: Thin-section photographs: Sidelight (Top), X-polarized (Middle), and Combination (Bottom)



T19_1A_04_15_C2: Interaction load trace (Top); Structural deflection (Bottom).



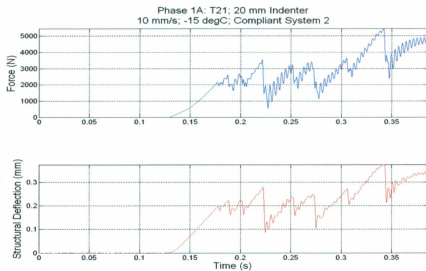
T19_1A_04_15_C2: Thin-section photographs: Sidelight (Top), X-polarized (Middle), and Combination (Bottom)



T20_1A_07_15_C2: Interaction load trace (Top); Structural deflection (Bottom).



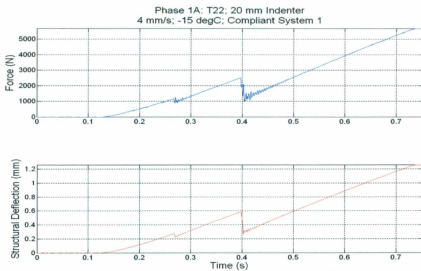
T20_1A_07_15_C2: Thin-section photographs: Silight (Top), X-polarized (Middle), and Combination (Bottom)



T21_1A_10_15_C2: Interaction load trace (Top); Structural deflection (Bottom).



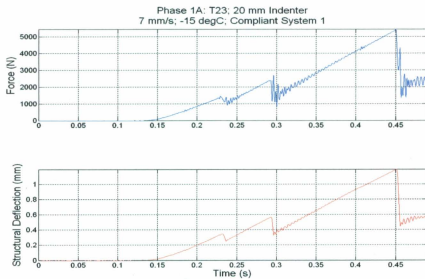
T21_1A_10_15_C2: Thin-section photographs: Silight (Top), X-polarized (Middle), and Combination (Bottom)



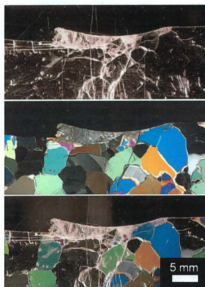
T22_1A_04_15_C1: Interaction load trace (Top); Structural deflection (Bottom).



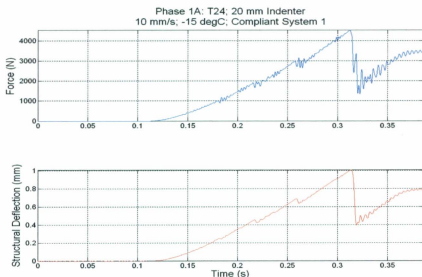
T22_1A_04_15_C1: Thin-section photographs: Sidelight (Top), X-polarized (Middle), and Combination (Bottom)



T23_1A_07_15_C1: Interaction load trace (Top); Structural deflection (Bottom).



T23_1A_07_15_C1: Thin-section photographs: Silight (Top), X-polarized (Middle), and Combination (Bottom)

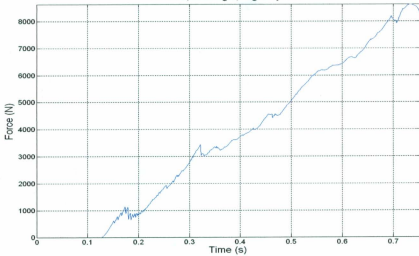


T24_1A_10_15_C1: Interaction load trace (Top); Structural deflection (Bottom).



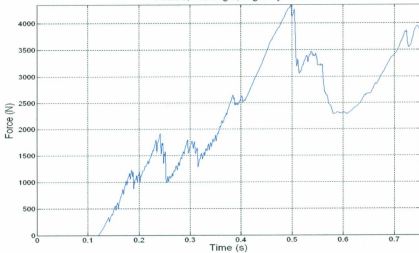
T24_1A_10_15_C1: Thin-section photographs: Silight (Top), X-polarized (Middle), and Combination (Bottom)

Phase 1A: T25; 20 mm Indenter
4 mm/s; -10 degC; Rigid System



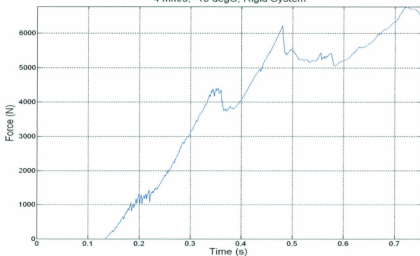
T25_1A_04_10_R: Interaction load trace.

Phase 1A: T26; 20 mm Indenter
4 mm/s; -10 degC; Rigid System



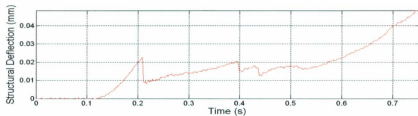
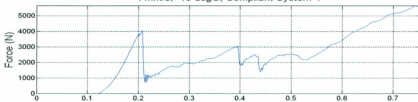
T26_1A_04_10_R: Interaction load trace.

Phase 1A: T27; 20 mm Indenter
4 mm/s; -10 degC; Rigid System



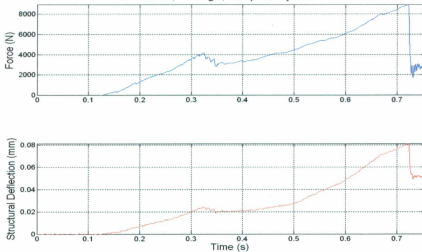
T27_1A_04_10_R: Interaction load trace.

Phase 1A: T28; 20 mm Indenter
4 mm/s; -10 degC; Compliant System 4



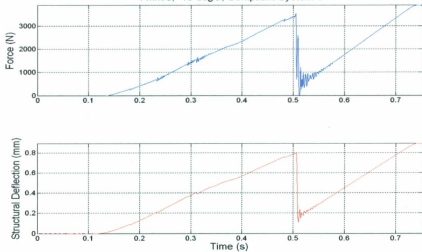
T28_1A_04_10_C4: Interaction load trace (Top); Structural deflection (Bottom).

Phase 1A: T29; 20 mm Indenter
4 mm/s; -10 degC; Compliant System 4



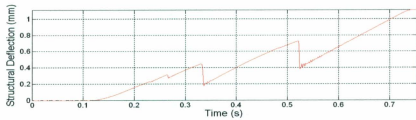
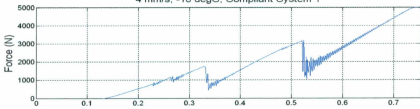
T29_1A_04_10_C4: Interaction load trace (Top); Structural deflection (Bottom).

Phase 1A: T30; 20 mm Indenter
4 mm/s; -10 degC; Compliant System 1



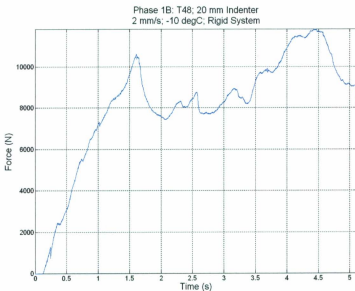
T30_1A_04_10_C1: Interaction load trace (Top); Structural deflection (Bottom).

Phase 1A: T31; 20 mm Indenter
4 mm/s; -10 degC; Compliant System 1

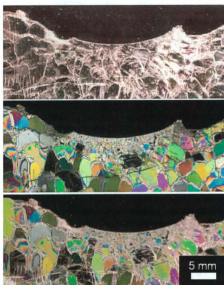


T31_1A_04_10_C1: Interaction load trace (Top); Structural deflection (Bottom).

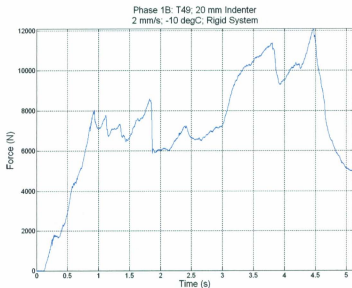
Phase 1B



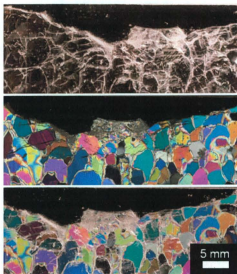
T48_1B_02_10_R20: Interaction load trace.



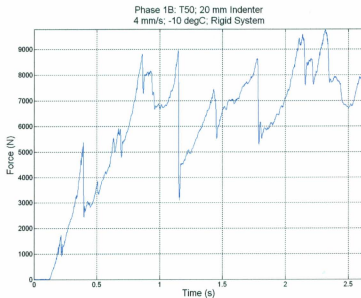
T48_1B_02_10_R20: Thin-section photographs: Sidelight (Top), X-polarized (Middle), and Combination (Bottom)



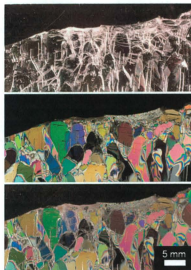
T49_1B_02_10_R20: Interaction load trace.



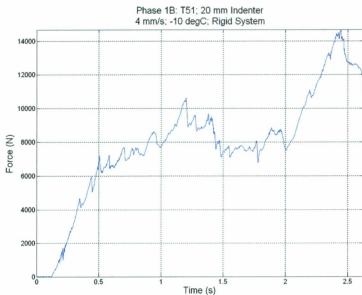
T49_1B_02_10_R20: Thin-section photographs: Sidelight (Top), X-polarized (Middle), and Combination (Bottom)



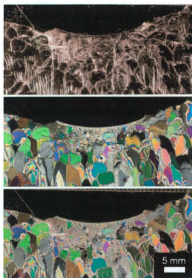
T50_IB_04_10_R20: Interaction load trace.



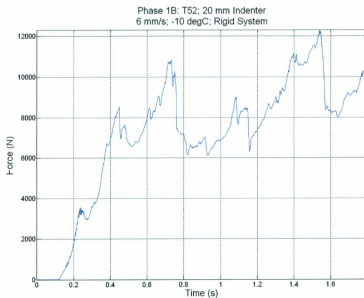
T50_IB_04_10_R20: Thin-section photographs: Sidelight (Top), X-polarized (Middle), and Combination (Bottom)



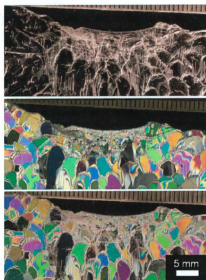
T51_1B_04_10_R20: Interaction load trace.



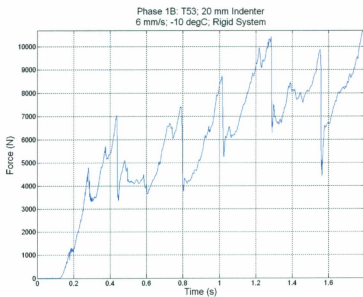
T51_1B_04_10_R20: Thin-section photographs: Silight (Top), X-polarized (Middle), and Combination (Bottom)



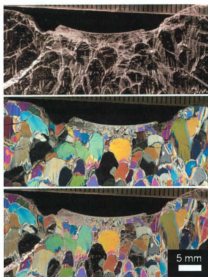
T52_1B_06_10_R20: Interaction load trace.



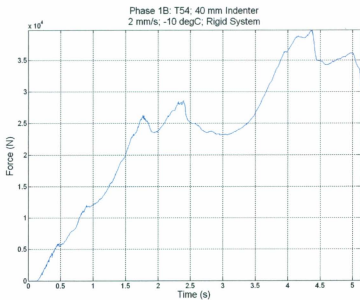
T52_1B_06_10_R20: Thin-section photographs: Sidelight (Top), X-polarized (Middle), and Combination (Bottom)



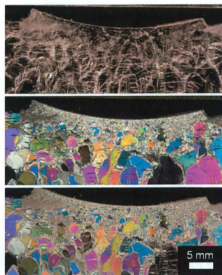
T53_1B_06_10_R20: Interaction load trace.



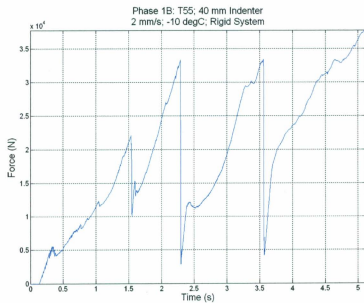
T53_1B_06_10_R20: Thin-section photographs: Silight (Top), X-polarized (Middle), and Combination (Bottom)



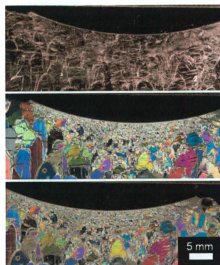
T54_1B_02_10_R40: Interaction load trace.



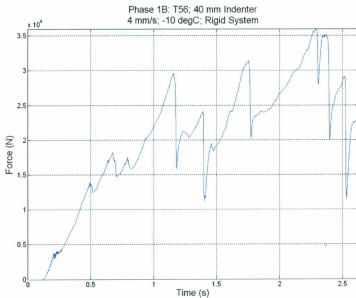
T54_1B_02_10_R40: Thin-section photographs: Sidelight (Top), X-polarized (Middle), and Combination (Bottom)



T55_1B_02_10_R40: Interaction load trace.



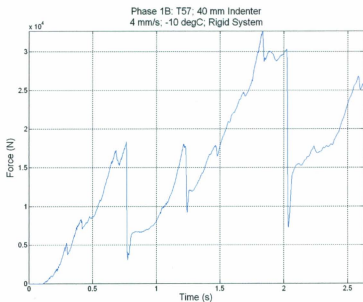
T55_1B_02_10_R40: Thin-section photographs: Sidelight (Top), X-polarized (Middle), and Combination (Bottom)



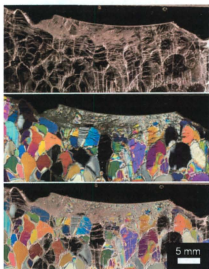
T56_1B_04_10_R40: Interaction load trace.



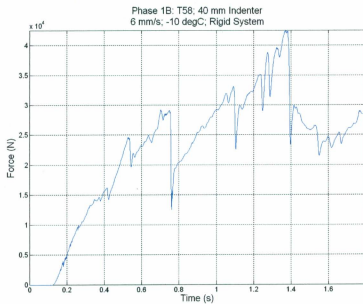
T56_1B_04_10_R40: Thin-section photographs: Sidelight (Top), X-polarized (Middle), and Combination (Bottom)



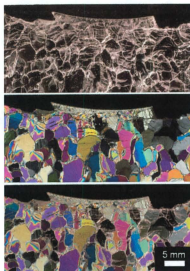
T57_1B_04_10_R40: Interaction load trace.



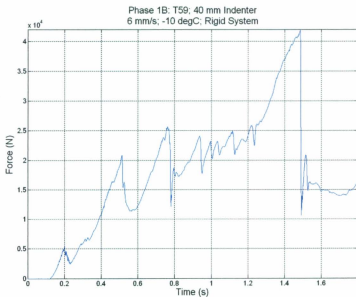
T57_1B_04_10_R40: Thin-section photographs: Sidelight (Top), X-polarized (Middle), and Combination (Bottom)



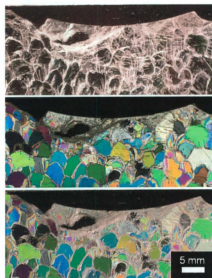
T58_1B_06_10_R40: Interaction load trace.



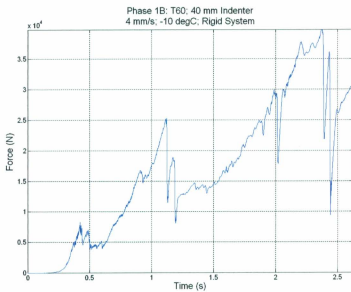
T58_1B_06_10_R40: Thin-section photographs: Sidelight (Top), X-polarized (Middle), and Combination (Bottom)



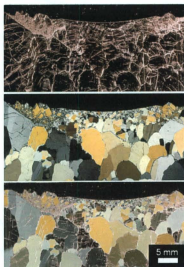
T59_1B_06_10_R40: Interaction load trace.



T59_1B_06_10_R40: Thin-section photographs: Sidelight (Top), X-polarized (Middle), and Combination (Bottom)

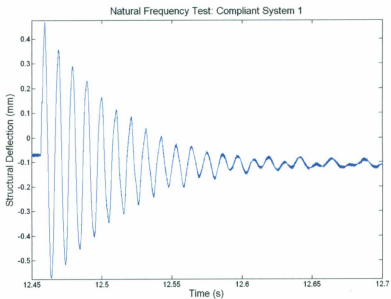
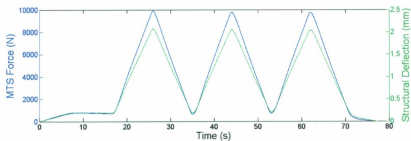
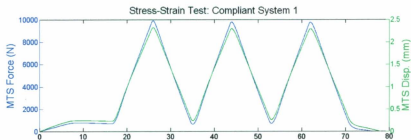


T60_1B_04_10_R40: Interaction load trace.

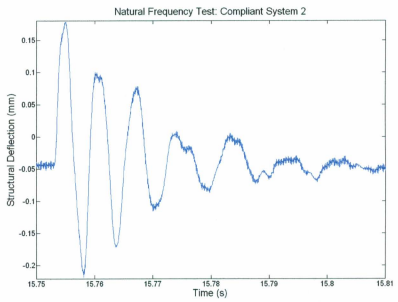
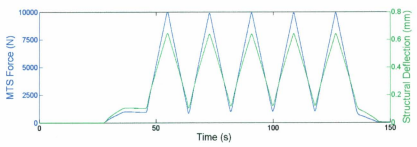
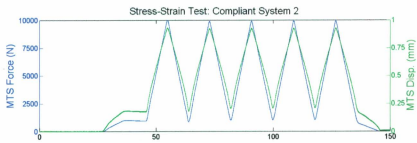


T60_1B_04_10_R40: Thin-section photographs: Silight (Top), X-polarized (Middle), and Combination (Bottom)

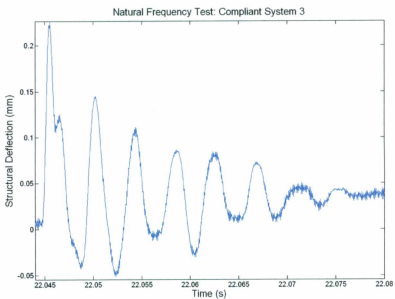
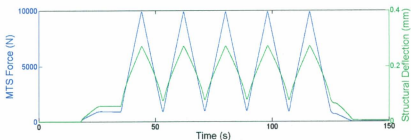
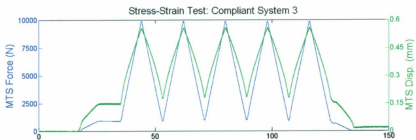
APPENDIX B – System Characterization Test Results



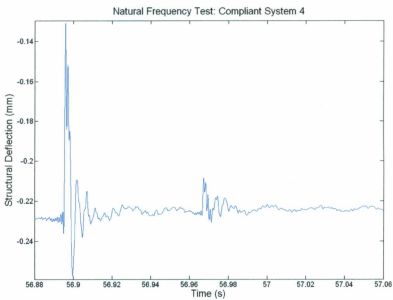
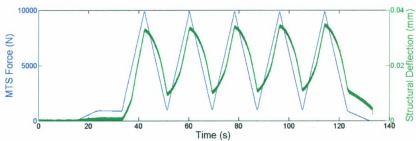
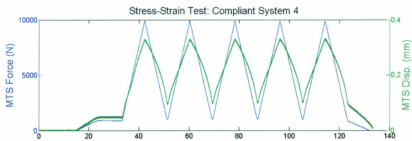
System characterization Tests for Compliant System 1



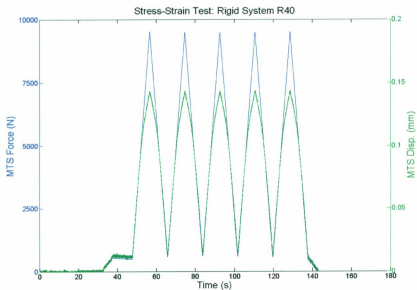
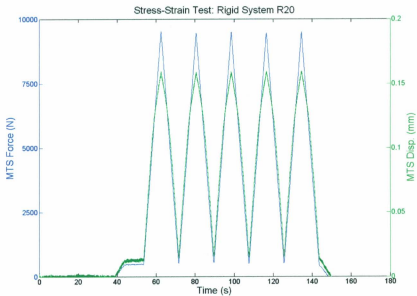
System characterization Tests for Compliant System 2



System characterization Tests for Compliant System 3



System characterization Tests for Compliant System 4



System characterization Tests for Rigid Systems R20 (Top) and R40 (Bottom)

APPENDIX C – Calibrations

Tekscan I-Scan Pressure Sensors

The Tekscan I-Scan system requires calibration prior to use consisting of three separate stages: conditioning, equilibration, and calibration.

Conditioning:

New sensors or sensors that have not been used for a length of time require conditioning. Conditioning the sensor minimizes the effects of drift and hysteresis. Each sensor was uniformly loaded 3 to 5 times to a pressure 20% greater than the anticipated pressures for the tests. This was achieved by placing the sensor between two pieces of neoprene and applying the required load with the MTS. The pieces of neoprene were larger than the sensor area to ensure uniform load over the sensor.

Equilibration:

Due to the design of the sensors each sensor is unique. For instance the distribution of the pressure-sensitive ink through the sensor is not precisely uniform and as a sensor is used certain sensels may become less responsive. This results in variations within the sensels of a sensor and variations between sensors. Equilibration compensates for these differences.

A Switchable-Equilibration was applied to the sensors. This process of equilibration consisted of placing the sensor between two pieces of neoprene and applying an even load across the sensor using the MTS. Each sensor was loaded

to 100 kN in increments of 10 kN. At each load level the I-Scan software assigns a unique scale-factor to each sensel making them all equal. This data is recorded and saved.

Calibration:

A Tekscan sensor is composed of an array of sensels with each sensel being a force sensitive variable resistor, with a level of impedance of .10 Meg ohms, under zero load, and 20 kilo ohms, under full load. When a load is applied to a sensel the corresponding level of impedance is assigned a digital value through means of an analog-to-digital converter. Calibration is required to correlate the digital output to engineering units (i.e. Newtons and Pascals).

The calibration procedure consisted of a series of linear, single-load calibrations. For a single load calibration a known force was applied, using the MTS, to an area of the sensor using a piece of neoprene smaller than the sensors total area. Each digital output value and corresponding load value is saved in a calibration file. Depending on the experimental loads, one of the series of calibration files is chosen and applied after the test using the associated I-Scan software. This is referred to as a post calibration. The series of calibration loads ranged from 10 kN to 100 kN, in increments of 10 kN.

Miniature Load Cell

Calibration of COLDDAS Channel 4

11:27 27 April 2011

Project: Ice Compressive Failure Mechanics

Facility: LARGE COLD ROOM

Sensor: BEAM LOAD

Model: SENSOTEC 3K LBWP

Serial Number: A1054R 569970

Programmable Gain: 1

Plug-In Gain: 500

Filter Frequency: 3000.0 Hz

Data Point No.	Input Signal (volts)	Physical Value (N)	Fitted Curve Value (N)	Error (N)	
1	-0.354	-500.0	-495.7	4.328	
2	-5.682	-8000.0	-7999.1	0.852	
3	-0.068	-100.0	-93.6	6.422	
4	-1.427	-2000.0	-2000.6	-0.564	
5	-2.850	-4000.0	-4011.5	-11.506	← Maximum Error
6	-4.268	-6000.0	-6008.5	-8.516	
7	-6.302	-9000.0	-8999.6	0.394	
8	-0.211	-300.0	-295.0	4.988	
9	-7.096	-10000.0	-9990.4	9.600	

Maximum Error = -0.116 % of Calibration Range.

Definition of Calibration Curve
Polynomial Degree = 1 (Linear Fit)

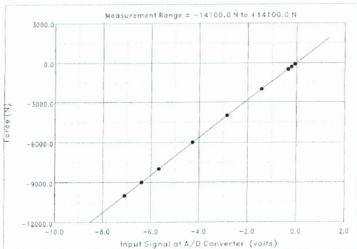
$$Y = C_0 + C_1 \cdot V$$

where $Y(t)$ = Force (N),

$V(t)$ = input signal at A/D converter (volts),

C_0 = 2.60958 N,

and C_1 = 1408.33 N/volt.



LVDTs

Calibration of COLDDAS Channel 5

11:14 29 April 2011

Project: Ice Compressive Failure Mechanics

Facility: LARGE COLD ROOM

Sensor: LVDT #1

Model: TRANS-TEK 0235-0000 D-11R

Serial Number: 5216

Programmable Gain: 1

Plug-In Gain: 1

Filter Frequency: 1000.0 Hz

Data Point No.	Input Signal (volts)	Physical Value (mm)	Fitted Curve Value (mm)	Error (mm)	
1	-5.669	3.094	3.014	0.009826	
2	-2.780	5.005	4.999	-0.006354	
3	0.130	7.015	6.998	-0.017266	
4	3.058	9.021	9.009	-0.011838	
5	5.976	11.004	11.014	0.009794	
6	7.442	12.009	12.021	0.020854	← Maximum Error
7	4.503	10.000	10.002	0.001648	
8	1.506	7.988	7.984	-0.013590	
9	-1.318	5.995	5.983	-0.012487	
10	-4.231	4.002	4.001	-0.000701	
11	-7.115	2.000	2.020	0.020122	

Maximum Error = 0.209 % of Calibration Range.

Definition of Calibration Curve
Polynomial Degree = 1 (Linear Fit)

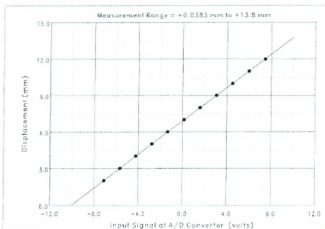
$$Y = C_0 + C_1 \cdot V$$

where $Y(t)$ = Displacement (mm),

$V(t)$ = input signal at A/D converter (volts),

C_0 = 6.90831 mm,

and C_1 = 0.687001 mm/volt.



Project: Ice Compressive Failure Mechanics

Facility: LARGE COLD ROOM

Sensor: LVDT 02

Model: TRANS-TEK 0235-0000 D-11R

Serial Number: 5214

Programmable Gain: 1

Plug-In Gain: 1

Filter Frequency: 1000.0 Hz

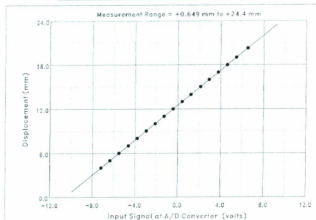
Data Point No.	Input Signal (volts)	Physical Value (mm)	Fitted Curve Value (mm)	Error (mm)	
1	-6.343	5.005	4.995	-0.010216	
2	-4.640	7.007	7.017	0.010412	
3	-2.955	9.010	9.020	0.010470	
4	-1.281	11.009	11.010	0.000825	
5	0.399	13.017	13.006	-0.010921	
6	2.110	15.048	15.039	-0.009211	
7	3.763	17.003	17.004	0.000683	
8	5.447	19.010	19.004	-0.005702	
9	6.509	20.253	20.267	0.014011	± Maximum Error
10	4.509	17.003	17.097	0.003803	
11	2.916	16.002	15.996	-0.005587	
12	1.216	13.986	13.977	-0.009292	
13	-0.448	12.003	12.000	-0.003248	
14	-2.125	9.999	10.007	0.008173	
15	-3.802	8.002	8.014	0.011839	
16	-5.493	6.001	6.004	0.002911	
17	-7.187	4.000	3.991	-0.008895	

Maximum Error = 0.0802 % of Calibration Range.

Definition of Calibration Curve

Polynomial Degree = 1 (Linear Fit)

$$Y = C_0 + C_1 \cdot X$$

where $Y(t)$ = Displacement (mm), $X(t)$ = input signal at A/D converter (volts), C_0 = 12.5318 mm,and C_1 = 1.18833 mm/volt.

Project: Ice Compressive Failure Mechanics

Facility: LARGE COLD ROOM

Sensor: LVDT #3

Model: TRANS-TEK 0235-0000 D-11R

Serial Number: 5215

Programmable Gain: 1

Plug-In Gain: 1

Filter Frequency: 1000.0 Hz

Data Point No.	Input Signal (volts)	Physical Value (mm)	Fitted Curve Value (mm)	Error (mm)	
1	-6.224	5.009	4.999	-0.010430	
2	-4.509	7.001	7.021	0.019593	
3	-2.786	9.024	9.052	0.028190	
4	-1.068	11.061	11.077	0.016229	
5	0.562	13.016	12.999	-0.017130	
6	2.272	15.057	15.015	-0.042183	
7	3.950	17.024	16.994	-0.030142	
8	5.701	19.035	19.058	0.023178	
9	6.597	20.048	20.115	0.066792	= Maximum Error
10	4.786	17.999	17.980	-0.019230	
11	3.077	16.006	15.964	-0.041806	
12	1.383	14.998	14.967	-0.030823	
13	-0.272	12.008	12.015	0.007341	
14	-1.951	10.004	10.036	0.031775	
15	-3.656	8.003	8.027	0.023664	
16	-5.367	6.005	6.009	0.004380	
17	-7.086	4.011	3.982	-0.029401	

Maximum Error = 0.416 % of Calibration Range.

Definition of Calibration Curve
Polynomial Degree = 1 (Linear Fit)

$$Y = C_0 + C_1 \cdot V$$

where $Y(t)$ = Displacement (mm),

$V(t)$ = input signal at A/D converter (volts),

C_0 = 12.3366 mm,

and C_1 = 1.17901 mm/volt.

Measurement Range = +0.546 mm to +24.1 mm

